ÇUKUROVA UNIVERSITY
INSTITUTE OF NATURAL AND APPLIED SCIENCES

M.Sc. THESIS

Fuad SARIĞIGÜZEL

FREE SURFACE AND PASSIVE CONTROL EFFECTS ON FLOW CHARACTERISTICS AROUND VARIOUS TORPEDO-LIKE GEOMETRIES

DEPARTMENT OF MECHANICAL ENGINEERING

ADANA-2019

ÇUKUROVA UNIVERSITY
INSTITUTE OF NATURAL AND APPLIED SCIENCES

FREE SURFACE AND PASSIVE CONTROL EFFECTS ON FLOW CHARACTERISTICS AROUND VARIOUS TORPEDO-LIKE GEOMETRIES

Fuad SARIĞIGÜZEL

MSc THESIS

DEPARTMENT OF MECHANICAL ENGINEERING

We certify that the thesis titled above was reviewed and approved for the award of the degree of the Master of Science by the board of jury on 30/12/2019.

…………………….	………………………..	………………………………...
Prof.Dr. Beşir ŞAHİN	Prof.Dr. Hüseyin AKILLI	Prof.Dr. Muammer ÖZGÖREN
SUPERVISOR	MEMBER	MEMBER

This MSc thesis is written at the Department of Mechanical Engineering, Institute of Natural and Applied Sciences of Çukurova University.
Registration Number:

Prof. Dr. Mustafa GÖK
Director
Institute of Natural and Applied Sciences

This thesis was financially supported by the Scientific and Technological Research Council of Turkey under contract no: 214M318. Additional financial support was also received from the Scientific Research Project Office of Çukurova University under contract no: FYL-2019-11552.

ABSTRACT

MSc. THESIS

FREE SURFACE AND PASSIVE CONTROL EFFECTS ON FLOW CHARACTERISTICS AROUND TORPEDO-LIKE GEOMETRY

Fuad SARIĞIGÜZEL

ÇUKUROVA UNIVERSITY
INSTITUTE OF NATURAL AND APPLIED SCIENCES
DEPARTMENT OF MECHANICAL ENGINEERING

Supervisor : Prof. Dr. Beşir ŞAHİN
Year: 2019, Pages: 105
Jury : Prof. Dr. Beşir ŞAHİN
: Prof. Dr. Hüseyin AKILLI
: Prof. Dr. Muammer ÖZGÖREN

The present study investigates the effect of free-surface on the flow structure around a model of an underwater vehicle called torpedo-like geometry by using experimental and numerical methods. The numerical study utilizes the pressure-based solver of ANSYS-Fluent software while the experimental study employs the dye flow visualization and particle image velocimetry (PIV) methods. The Large Eddy Simulation (LES) is performed to reveal the unsteadiness of the flow structure around the torpedo-like geometries. The interface-capturing volume of the fluid fraction (VOF) method is used to model the free-surface. The results show that the flow characteristics such as velocity field, streamline topology, vorticity, and kinetic energy becomes asymmetric as the torpedo-like geometry is located close to free-surface. Therefore, the resulted drag force, F_D for h/D = 0.75 was found to increase relative to uniform flow condition. It was also found that the free-surface effect becomes negligible for submergence depth ratios higher than 2.5 owing to the near-symmetrical form of the flow structures. Also, when the Reynolds number is increased from Re = $20x10^3$ to $40x10^3$, time-averaged vorticity formation length and drag coefficient, C_D decrease for all examined torpedo-like geometries. As a passive control method, modifications were applied by adding 3 and 4 wings to the stern section of the torpedo-like geometry to examine in detail the resulted flow structure and drag force. It is observed from numerical results that the stern with wings favorably organizes the wake region while increasing the drag coefficient, C_D.

Key Words: Free-Surface effect, Large Eddy Simulation (LES), PIV, Torpedo-like geometry, Volume-of-Fluid (VOF)

ÖZ

YÜKSEK LİSANS TEZİ

TORPEDO-BENZERİ GEOMETRİSİNDEKİ AKIŞ ÖZELLİKLERİNDE SERBEST YÜZEY VE PASİF KONTROL ETKİLERİ

Fuad SARIĞIGÜZEL

ÇUKUROVA ÜNİVERSİTESİ
FEN BİLİMLERİ ENSTİTÜSÜ
MAKİNE MÜHENDİSLİĞİ ANABİLİM DALI

Danışman : Prof. Dr. Beşir ŞAHİN
Yıl: 2019, Sayfa: 105
Jüri : Prof. Dr. Beşir ŞAHİN
: Prof. Dr. Hüseyin AKILLI
: Prof. Dr. Muammer ÖZGÖREN

Bu çalışmada, torpido-benzeri geometri olarak adlandırılan serbest yüzeyin etkisi altında modellerin etrafındaki akış yapısı sayısal ve deneysel yöntemlerle araştırılmıştır. Sayısal çalışmada ANSYS-Fluent yazılımının sıkıştırılamaz çözücüsü kullanılmıştır. Deneysel çalışmada ise boya görselleştirmesi ve parçacık görüntülemeli hız ölçme yöntemleri uygulanmıştır. Akış yapısının geometri etrafındaki daimi olmayan akış özelliklerini hesaplamak için Büyük Girdap Simülasyonu (LES) türbülans modeli ile çözümlemeler yapılmıştır. Serbest yüzeyde hava-su ara yüzeyindeki akış özelliklerinin belirlenmesi için sıvı/gas akış oranı hacmi modelleme (VOF) yöntemi kullanılmıştır. Elde edilen sonuçlar, torpido benzeri geometrinin serbest yüzeye yakın olması nedeniyle hız alanı, akım çizgileri, girdap ve kinetik enerji gibi akış karakteristiklerin simetrik olmadığı görülmüştür. Bu nedenle, sonuçta meydana gelen sürükleme kuvvetinin (F_D), daldırma oranı h/D = 0.75'e göre üniform akışa kıyasla arttığı bulunmuştur. Daldırma oranı h/D = 2.5 için akış yapısının simetrik bir formda oluştuğu, serbest yüzey etkisinin ihmal edilebilir düzeye indiği ve buna bağlı olarak üniform akış durumuna benzer akış özellikleri olduğu görüldü. Ayrıca, Reynolds sayısı $20x10^3$'den $40x10^3$'e yükseldiğinde ve sürükleme kuvvetinin (F_D), daldırma oranı (h/D) arttıkça azaldığı, girdap uzunluğunun kısalarak modelin kuyruk kısmına yaklaştığı ve art izi bölgesi küçülmüştür. Pasif akış kontrol uygulaması ile aynı burun geometrisine sahip modelin kuyruğuna 3 ve 4 kanat eklenmesinin akış yapısı ve sürükleme kuvveti üzerindeki etkisi incelenmiştir. Nümerik sonuçlara göre kanatların art izi bölgesindeki akışı olumlu yönde etkilediği ancak sürükleme kuvveti katsayısının kısmen yükseldiği tespit edilmiştir.

Anahtar Kelimeler: Akış Hacmi (VOF), Büyük Girdap Simülasyonu (LES), PIV, Serbest yüzey etkisi, Torpido-benzeri geometri

EXPANDED ABSTRACT

Many engineers and scientists have been interested in studying the flow structure around underwater vehicles due to the importance of their wide range of applications. Underwater vehicles, for example, may be utilized for underwater exploration, inspections, maintenance, construction, rescue activities, or military defense. Those and many other applications require the vehicle to operate efficiently and stably under the water surface. Such requirements cannot be achieved unless a detailed study is performed to analyze the flow structure around the vehicle and its hydrodynamic coefficients.

Underwater vehicles are forced to consume more energy to overcome the pressure difference between its front and rear surface during its motion under the water surface. This pressure difference forms an unsteady drag resistance due to flow separation around its body. At the same time, the vibrations induced by the flow structures on the vehicle can move the vehicle out of its orbit, leading to undesirable routes. This in return negatively affects maneuverability of the torpedo-like vehicles during the motion. Decreasing the drag resistance and/or controlling the lift force is very important, especially for vehicles that are desired to move towards a specific target. Besides flow characteristics such as flow separation from the objects, vortex shedding mechanism and turbulence effects should be controlled. For controlling or decreasing such flow-induced forces over moving vehicles in flow, optimization of various geometries and passive flow control applications are commonly used.

Flow control techniques are divided into two groups which are active flow control in which energy consumed and passive flow control in which flow structure is manipulated with geometric parameters or by the energy of the fluid in motion. Complexities and negative factors in a flow around an underwater vehicle are tried to be minimized by means of an interaction constituted by manipulating high momentum flow towards the low momentum vortex flow region with a passive

flow control method. Many passive flow control methods are available in the literature, which generally intended to narrow wake and prevent flow separation such as modification on the objects, hydrofoils, o-rings, vortex generators, tail, and winglets. These passive control techniques are used not only for hydrodynamic performance but also for noise and vibration control.

The work considered in this study aims to investigate numerically and experimentally the hydrodynamics characteristics of unsteady flow structure around a torpedo-like underwater vehicle placed at various locations near water free-surface. Furthermore, the passive flow control method is applied to the torpedo-like vehicle by placing hydrofoil-shape wings at the rear part of the vehicle as an attempt to minimize the adverse effects of the flow characteristics around the vehicle. A torpedo-like underwater vehicle is considered as a type of Autonomous underwater vehicle (AUVs) which has a propeller attached to its stern. Since the flow characteristics due to the hull or stern form are to be investigated to decrease the drag coefficient and related energy consumption. However, the propeller for the examined models was neglected in this study. The geometry of torpedo-like underwater vehicles may be divided into three geometric parts; nose section (elliptic, spherical, cambered nose), mid-section (in the cylindrical form) and the stern section (in elliptic, conical and sharp corner shape). To constitute such torpedo-like geometries, different diameters, lengths, aspect ratio, spherical radius, cone angle, surface structure, angle of attack, hydrofoil location, tail wing, geometries, and dimensions can be changed. These changes substantially affect flow structure around the geometry. Flow occurred around the geometry should be examined in detail in respect of hydrodynamic flow characteristics according to the location of the torpedo-like geometry exposing to uniform flow and free water surface.

The study is performed at Reynolds numbers of $20x10^3$ and $40x10^3$ (based on the characteristic length, *L*, of the geometry), and for submergence depth ratios, *h/D* which are varied from 0.50 to 3.5. Firstly, numerical investigations were performed by utilizing the ANSYS-FLUENT software which provides the required solutions for setting up the Large Eddy Simulation (LES), and for modeling the free surface of the water. LES is performed in this study to reveal the unsteadiness of the flow structure around the geometry for the considered submergence depth ratios (*h/D*), while the interface-capturing volume-of-fluid (VOF) method is used to model the free-surface. The mesh generated to carry out the simulation comprises of polyhedral cells and resolves the viscous sublayer ($y^+ < 1$). The mesh is refined in the vicinity of the torpedo-like geometry in order to reduce discretization errors. Later, the dye visualization experiments and velocity field measurements using the PIV method were done at Re = $20x10^3$ and $40x10^3$ for submergence depth ratios, *h/D* of 0.75, 1.00, 1.50, 2.00, and 3.00 while keeping the angle of attack zero.

The examined torpedo-like geometry having a cambered nose is similar to the missile shroud separation structure and its nose creates a boundary layer separation from the nose and reattachment to the surface again and then decreasing the negative effect on the flow characteristics such as an increase in drag phenomena.

The obtained results show that the free surface affects the flow structure when compared to uniform flow conditions. The flow characteristics such as velocity field, streamline topology, vorticity, and kinetic energy becomes asymmetric as the torpedo-like geometry is located close to free-surface. Therefore, as the submergence depth decreases the resulted drag force, F_D is increased relative to the uniform flow condition. For the highest submergence depth of *h/D*=3.5, flow structures occur nearly in symmetrical form and are similar to the uniform flow condition, indicating the negligible effect of the free surface. Also, when the Reynolds number is increased from Re = $20x10^3$ to $40x10^3$, time-averaged vorticity formation length and drag coefficient (C_D) decrease for all examined torpedo-like model geometries.

GENİŞLETİLMİŞ ÖZET

Birçok mühendis ve bilim insanı, geniş uygulama alanlarının önemi nedeniyle su altı araçlarının etrafındaki akış yapısını incelemekle ilgilenmiştir. Örneğin sualtı araçları, sualtı keşifleri, denetimler, bakım, inşaat, kurtarma faaliyetleri veya askeri savunma için kullanılabilir. Bu ve diğer birçok uygulama, aracın verimli ve su yüzeyinde sabit bir şekilde çalışmasını gerektirir. Bu şartlar, aracın etrafındaki akış yapısını ve hidrodinamik katsayılarını analiz etmek için ayrıntılı bir çalışma yapılmadıkça gerçekleştirilemez.

Su altı araçları, su yüzeyi altındaki hareketi sırasında ön ve arka yüzeyi arasındaki basınç farkının üstesinden gelmek için daha fazla enerji tüketmeye zorlanır. Bu basınç farkı, gövdesi etrafındaki akış ayrılmasından dolayı dengesiz bir sürtünme direnci oluşturur. Aynı zamanda, araçtaki akış yapılarının neden olduğu titreşimler, istenmeyen akış yönlenmelerine ve oluşumuna neden olmaktadır. Bu da, torpido benzeri araçların hareket sırasında manevra kabiliyetini olumsuz yönde etkilemektedir. Sürtünme direncini azaltmak ve kaldırma kuvvetini kontrol etmek, özellikle belirli bir hedeften geçmek isteyen araçlar için çok önemlidir. Cisim yüzeylerinden akış ayrılması gibi akış özelliklerinin yanı sıra girdap kopma mekanizması ve türbülans etkileri kontrol edilmelidir. Bir akışta hareket halindeki taşıtlar üzerinde bu tür akış kaynaklı kuvvetlerin kontrolü ya da azaltılması için çeşitli geometrilerin ve pasif akış kontrol uygulamalarının optimizasyonu yaygın olarak kullanılmaktadır.

Akış kontrol teknikleri, enerji tüketilen aktif akış kontrolü ve akış yapısının geometrik parametrelerle veya hareket halindeki akışkanının enerjisiyle manipüle edildiği pasif akış kontrolünün olduğu iki gruba ayrılır. Bir su altı aracının etrafındaki bir akışta oluşan karmaşıklıklar ve negatif faktörler, pasif bir akış kontrol yöntemi ile düşük momentumu olan girdaplı akış bölgesine doğru yüksek momentum akışının manipüle edilmesiyle oluşturulan bir etkileşim vasıtasıyla en aza indirilmeye çalışılmaktadır. Literatürde genel olarak, cisim yüzeyinden akışın ayrılmasını önleme ve ayrılmış akış bölgesini azaltmak için akışa maruz kalan cismin veya modelin geometrisinde değişiklik yapma, kanatçıklar, o-ring, girdap jeneratörleri, kuyruk ve halka kanatları gibi akış ayrılmasını önleme amaçlı birçok pasif akış kontrol yöntemi mevcuttur. Bu pasif kontrol teknikleri sadece hidrodinamik performans için değil aynı zamanda gürültü ve titreşim kontrolü için de kullanılır.

Burada ele alınan çalışma, serbest su yüzeyine yakın çeşitli yerlere yerleştirilen torpido benzeri bir su altı aracının etrafındaki daimi olmayan akış yapısının hidrodinamik özelliklerini sayısal ve deneysel olarak incelemeyi amaçlamaktadır. Ayrıca, aracın arka kısmına hidrofil benzeri şekilli kanatçıklar aracın etrafındaki su serbest yüzeyinin olumsuz etkilerini en aza indirmeye çalışmak amacıyla torpido benzeri araca pasif akış kontrol yöntemi uygulanmaktadır. Torpido benzeri bir su altı aracı, arka kısmına takılı bir pervaneye sahip bir tür Özerk sualtı aracı (AUV) olarak kabul edilir. Gövde formuna bağlı akış karakteristiği, ne kadar itki kuvveti oluşturduğundan ziyade akış özellikleri araştırılması düşünüldüğünden bu çalışmada pervane etkisi ihmal edilmiştir. Torpido benzeri su altı aracının geometrisi üç geometrik bölüme ayrılabilir; ön kısım (küresel ve elips formunda), gövde (silindirik formda) ve arka kısım (elips, konik, yuvarlatılmış keskin kenarlı köşe). Torpido benzeri geometriler, farklı çaplar, uzunluklar, en boy oranı, küresel yarıçap, koni açısı, yüzey yapısı, yalpalama açısı, hücum açısı, kuyruk kanadı, geometriler ve boyutlar oluşturulabilir. Bu değişiklikler geometri etrafındaki akış yapısını büyük ölçüde etkiler. Geometri etrafında oluşan akış, üniform akışa ve serbest su yüzeyine maruz kalan akıştaki torpido benzeri geometrinin konumuna göre hidrodinamik akış özellikleri açısından detaylı olarak incelenmelidir.

Bu çalışmda, Re = $20x10^3$ ve $40x10^3$ Reynolds sayıları (geometrinin karakteristik uzunluğu L'ye bağlı olarak) ve daldırma derinlikleri oranı h/D = 0.5 ila 3.5 arasında değiştirlerek gerçekleştirildi. İlk olarak, Büyük Eddy simülasyonunun (LES) uygulanması ve suyun serbest yüzeyinin modellenmesi için gerekli araçları sağlayan ANSYS-FLUENT programı kullanılarak sayısal araştırmalar yapılmıştır. Bu çalışmada, LES, su altında kalan derinliklerin (*h/D*) geometri etrafındaki akış yapısının dengesizliğini ortaya çıkarmak için yapılırken, serbest yüzeyin modellenmesinde arabirim yakalama akışkan hacmi (VOF) yöntemi kullanılmıştır. Simülasyonu gerçekleştirmek için oluşturulan ağ çokyüzlü hücrelerden oluşur ve yapışkan alt tabakayı ($y^+ < 1$) düzeltir. Diferansiyel denklemi ayrıklaştırmadan kaynaklanan hatalarını azaltmak için torpido benzeri geometrinin cidar yakın bölgesinde daha küçük boyutta yoğun ağ yapısı oluşturulmuştur. Daha sonra, boya görselleştirme ve PIV yöntemiyle hız alanı ölçüm deneyleri ve sıfır derece sabit hücum açısında çeşitli daldırma derinliklerinde (*h/D* = 0.75, 1.0, 1.5, 2.0, 3.0) ve Re=$20x10^3$ ve $40x10^3$ Reynolds sayılarında yapılmıştır.

Bombeli uç olarak incelenen uç geometrisi füzelerin gövdelerinden ayrılan kapsüle benzerdir. Bu bombeli şekil burun kısmında akış ayrılması oluşturur, bombeli uça göre daha düşük çaptaki gövdeye ayrılmış akışın tekrar yüzeye yapışmasına katkı sağlar, sürüklenmedeki artış olayı gibi akış karakteristikleri üzerindeki negatif etkiyi de azaltır .

Elde edilen sonuçlar, serbest yüzeyin, üniform akış durumuna göre akış yapısını etkilediğini göstermektedir. Torpido benzeri geometrinin serbest yüzeye yakın olması nedeniyle hız alanı, akım çizgisi değişimi, girdap konturları ve kinetik enerji gibi akış karakteristikleri asimetrik hale getirmektedir. Bu nedenle, sonuçta meydana gelen sürükleme kuvveti (F_D), dalma derinliği azaldıkça üniform akışa kıyasla önemli derecede artmaktadır. İncelenen en yüksek daldırma derinliği (*h/D*=3.5) değeri için akış yapıları, yaklaşık simetrik bir formda meydana gelmektedir ve serbest yüzey etkisinin ihmal edilebilir seviyeye düşmesinden dolayı üniform akış durumuna benzer özellik göstermektedir. Ayrıca, Reynolds sayısı Re = $20x10^3$'den Re=$40x10^3$'e yükseltildiğinde, zamana göre ortalama girdap oluşumu uzunluğu ve sürüklenme kuvvet katsayısı (C_D), incelenen tüm torpido benzer geometriler için azalmaktadır.

ACKNOWLEDGMENTS

I would like to thank my supervisor Prof. Dr. Beşir ŞAHİN who continuously supported and guided my thesis work. Also, I would like to express my gratitude to Prof. Dr. Hüseyin AKILLI for his support and encouragement as the Head of the Mechanical Engineering Department.

I sincerely thank Prof. Dr. Muammer ÖZGÖREN as the project coordinator of TÜBİTAK contract No:214M318 titled "Investigation of Flow Structure around Various New Generation Torpedo Like Geometries and its Control" for providing me this thesis subject and his continuous support thought this study. Also, I would like to thank to project advisor Prof. Dr. Beşir ŞAHİN, Project Researchers Assoc. Prof. Dr. Levent Ali KAVURMACIOĞLU and Assist. Prof. Dr. Tahir DURHASAN for their assistance in every subject of this study.

I would like to thank Research Assistant Sergen TÜMSE and Project Assistant Alpaslan KILAVUZ for their invaluable assistance during my experiments.

I sincerely thank Laboratory technician Sefa MERAL, Department secretary and officer, Seyyare ÇAĞLAR and Feyzullah AKÇALI for their help during my studies.

My sincere thanks go to my dearest family for their great patience and support during my studies, and I express my deepest gratitude especially to my parents who have continuously encouraged me along the way.

Last, I am grateful to the Çukurova University Scientific Research Project Office for their financial support under contract no: FYL-2019-11552.

CONTENTS **PAGES**

LIST OF FIGURES **PAGES**

NOMENCLATURE

L	:	The total length of the torpedo-like geometry
h	:	Submergence depth
D	:	The diameter of the mid-section part
A_c	:	The projected area in the streamwise direction
x, y	:	Streamwise, and crosswise coordinate directions
u	:	Streamwise components of velocity (m/s)
v	:	Crosswise components of velocity (m/s)
ω	:	Vorticity
Re	:	Reynolds number
U_∞	:	Freestream velocity (m/s)
C_D	:	Drag coefficient
α	:	Angle of Attack
$\langle \ldots \rangle$	:	Time-averaged operator

Abbreviations

HOV	:	Human-Occupied Vehicle
ROV	:	Remotely Operated Vehicle
AUV	:	Autonomous Underwater Vehicle
CCD	:	Charge-Coupled Device
CFD	:	Computational Fluid Dynamics
PIV	:	Particle Image Velocimetry
LES	:	Large Eddy Simulation
WALE	:	Wall-Adapting Local-Eddy-Viscosity Model
VOF	:	Volume-of-Fluid
TKE	:	Turbulent Kinetic Energy
CFL	:	Courant–Friedrichs–Lewy

XXV

1. INTRODUCTION

Since ancient times human beings have always been trying to discover and understand the marvelous environment under the sea surface for scientific, industrial, and military purposes. However, it took no long time to realize that underwater environment is physically too severe for humans' body to survive, and is unapproachable without some sort of protection that in a way or another compensates the absence of oxygen, the high pressure, and the low temperature under the water surface. At the very beginning, men overcome the absence of oxygen by inventing snorkel and swim fins for hands and feet, which enables him to stay underwater longer. However, the snorkel became useless for diving deeper since the increasing water pressure with depth makes it impossible for the diver to draw air through the snorkel. Later, the man was able to dive at greater depths with the innovation of a diving chamber, which is a closed container at atmospheric pressure that could be lowered and raised with cables or weights. Today, the diving chamber is more generally known as Underwater Vehicle (UV) which does not only provides a protective environment, but also enables man, while being under the water surface, to perform various tasks and missions such as making a direct observation, collecting data, and photographs, etc.

1.1. Developments of Underwater Vehicles

The earliest underwater vehicle designed by a Dutch scientist, Cornelius Van Drebblel, around 1620 was able to dive to depths of around 4 m and remain submerged for a few hours. About century later other successful designs of underwater vehicles were emerged out such as the *Turtle,* which was built by David Bushnell in 1776, and the *Nautilus* by Robert Fulton in 1800. At the beginning of the nineteenth century, most European navies had noticed the importance of underwater vehicle and started building large vehicles which are hand-propelled and are made of strong materials that sustain the increasing water pressure at greater depths.

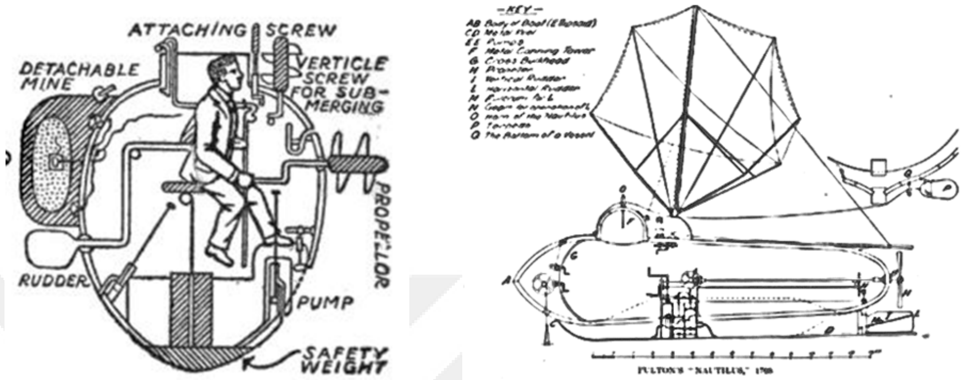

(a) (b)

Figure 1.1. Earliest examples of underwater vehicles; (a) David Bushnell's Turtle (Wikipedia, 2019), (b) Robert's Nautilus (Wikipedia, 2019)

In 1863, the French naval engineers launched the Plongeur that was the largest underwater vehicle at that time and was the first vehicle to be propelled by a compressed-air engine. Later in 1878, George Willam Garrett built a steam-powered underwater vehicle called Resurgam. By the end of the 1880s, the advent of the battery technology allows J. F. Waddington to go a step further in designing an underwater vehicle which was similar in size to the Resurgam vehicle but electrically powered. Meanwhile, George Willam Garrett and a Swedish engineer, Torsten Vilhelm Nordenfelt, worked together to build Nordenfelt I which was the first underwater vehicle that could fire a self-propelled torpedo. Later, Garrett and Nordenfelt commissioned by the Ottoman Navy to build two underwater vehicles which were 30.5 m long, steam-powered, capable of submerging to a depth of 30 m and could fire three torpedoes. In January 1888, both the vehicles were tested and although their movement was not at a desired accuracy under the sea, they successfully fired the torpedo, making the Ottoman navy to be the first in the world who launched torpedoes under the water. Up to the twentieth century, underwater vehicles were mainly being designed and built for military purposes whereas a few were being utilized for explorations of oceans and this was due to their inability to dive more than tens of meters under the water surface and to remain submerged for no more than a couple of hours (Marx, 1990).

Underwater vehicles saw enormous developments during the twentieth century, which has enabled the scientists for the first time to observe the marine fauna in their natural environment and has helped to recover lost equipment from ocean depths. In 1934, William Beebe and Otis Barton could descend to 923 m under the water surface in an underwater vehicle, called Bathysphere, which they had designed to study and photograph deep-sea life. The bathysphere was a 2.5-ton steel ball 1.37 m inside diameter and 38 mm thick, with three viewports (Marx, 1990). In spite of its success, however, Bathysphere was not able to dive on its own but through cables connected to the surface ship. The problem with the cables was that they prevent the Bathysphere to go more than a kilometer under the water surface. Auguste Piccard overcame this problem by designing an underwater vehicle, called Bathyscaphe, in 1954 which adjusts its depth by changing its weights. The Bathyscaphe has a flotation chamber containing gasoline and iron pellets. By releasing some of the gasoline, the bathyscaphe becomes heavier than water enabling it to dive, and by releasing some of the iron-shot ballast enables it to ascend back to surface. Another model of the bathyscaphe, called the Trieste II, came in 1960 to allow Jacques Piccard, the son of Auguste Piccard, with Don Walsh to descent to a depth of 10.9 km at the bottom of the Marians trench.

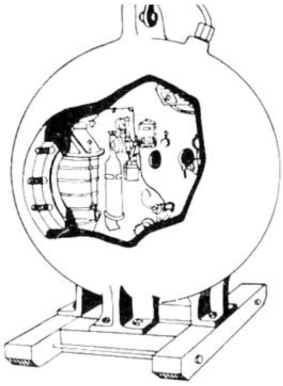

(a)

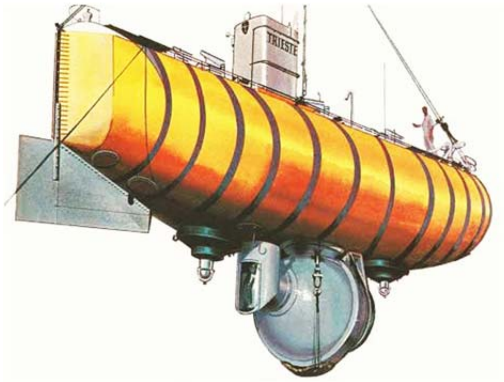

(b)

Figure 1.2. The famous two designs of underwater vehicles in twentieth-century; (a) *Bathysphere* designed by William Beebe (Anonymous, 2019c), and (b) *Bathyscaphe* designed by Auguste Piccard (Anonymous, 2019a)

Nowadays, underwater vehicles fall into three categories; Human-Occupied Vehicles (HOVs), Remotely Operated Vehicles (ROVs), and Autonomous Underwater vehicles (AUVs). HOVs allows human to present undersea surface for a limited period. They are built to withstand the high-pressure thousands of meters below the surface of the ocean and permit scientists to make detailed observations, collect specific samples, and place, retrieve, or conduct experiments in the deep ocean. Examples of HOVs are submarines, Bathyscaphe, Alvin, etc. On the other hand, ROVs are very popular un-crewed underwater vehicles that are controlled from the surface by a human being on the surface. All types of this vehicle are connected to the surface by a tether that provides power and control communication to the vehicle. The vehicles can remain below the surface for a day or more at a time and can hover like a helicopter over a seafloor target or survey a wide area (Shepherd, 2001). The last category of underwater vehicles, AUVs, are the most advanced vehicles that human beings have ever designed in the history. AUVs are uncrewed, untethered, computer-controlled underwater vehicles that can drift, drive, or glide through the ocean without real-time control by human operators. Some AUVs interact with operators periodically through satellite signals or underwater acoustic beacons, while others can make decisions on their own, changing their mission profile based on environmental data they receive through sensors.

Figure 1.3. Examples of AUV (Anonymous, 2019e) and ROV (Anonymous, 2019b)

There are two classes of AUVs. One of the classes is called *torpedo-like* vehicles, which have a propeller at its stern, and steerable control surfaces to control turns and vertical motion. However, torpedo-like vehicles require enough speed to maintain their motion and therefore, they are not controllable at very low speeds. The other class, called *Gliders*, are designed for applications where low speed, and/or long operating time underwater are required. Gliders do not produce thrust directly but rather, utilize the variable-buoyancy propulsion system, a system that uses buoyancy to generate vertical motion which is then translated into a trust using lifting surfaces such as wings (Bellingham, 2009).

Figure 1.4. Torpedo-like vehicle (Bellingham, 2009)

1.2. Hydrodynamic Aspects

Underwater Vehicles are forced to consume more energy to overcome an unsteady drag resistance which is created mainly due to the pressure difference between the front and rear surface of an object moving in a stream. Also, the unsteady drag resistance induces vibration in the flow structure which directly affects the motion accuracy of the object. Torpedo-like vehicles also encounter such an unsteady drag resistance which negatively affects its maneuverability during their motions. Therefore, it is essential to decrease the drag resistance of vehicles especially for those which are desired to move to a specific target. Besides, flow characteristics such as flow separation from the objects, vortex shedding mechanism, and turbulence effects should be minimized too.

In order to control the drag resistance and other factors, various flow control techniques are used. Flow control techniques are divided into two groups; i) Active flow control in which external energy is provided, and ii) Passive flow control in which flow structure is manipulated by attaching non-moving part to the geometry. Examples of such non-moving parts include hydrofoils, O-rings, vortex generators, tail and ring wings. Other passive flow control methods are available in the literature, which generally intended to decrease the drag resistance by narrowing the wake region and preventing flow separation. These passive flow control techniques are used not only for hydrodynamic performance but also for noise and vibration control.

1.3. Scope of the Thesis

The thesis intends to investigate the hydrodynamic characteristics of unsteady flow structures around different torpedo-like vehicles placed at various depths under the free-surface of water. Furthermore, passive flow control methods were considered for the stern section of the torpedo-like geometry as an attempt to minimize the adverse effects of the free-surface of water on the flow structure around the torpedo-like vehicles. In addition to studying the free surface of the water effect, the influence of the angle of attack can also be partly examined. The investigations were carried out experimentally by using dye flow visualization, and Particle Image Velocimetry (PIV) techniques as well as numerically by utilizing ANSYS FLUENT software, which provides the required tools for setting up a Large Eddy Simulation (LES). The software allows utilization of the Volume-of-Fluid model to simulate the water free-surface. These investigations were done at the Reynolds numbers ($U_\infty\ L/\nu$) of $20x10^3$ and $40x10^3$ based on the length of the model, and for the angle of attack of 0°, 4°, 8°, and 12°. The influence of the free-surface of water effect on the hydrodynamic characteristics was studied by utilizing the submergence depth ratio *h/D*, where *h* is the distance from the free-surface of water to the central plane of the model, and *D* is the diameter of the midsection of torpedo-like geometry. The submergence depth ratios considered here are *h/D* = 0.5, 0.75, 1.00, 1.50, 2.0, 3.0, and 3.5.

2. PREVIOUS STUDIES

There are many experimental and numerical studies in the literature related to this thesis concept. Some of them are given below.

Reichl et al. (2003) investigated the behavior of the wake Strouhal number for flow past a cylinder close to a free surface at both low and moderate Froude numbers. They made simulation at the low Froude number for various gap ratios and found significant changes in the Strouhal number as the gap ratio changes. Strouhal number becomes maximum when the gap ratio is 0.70. They changed the value of lift force acting on the cylinder and found that the separation of the ’jet’ from the free surface resulted in a decrease in the lift force acting upon the cylinder. In addition, they found that for the low Froude number, the results obtained were similar to those for flow past a cylinder close to an adjacent no-slip boundary.

Jagadeesh and Murali (2005) investigated the ability of k-epsilon turbulence models to predict hydrodynamic coefficients for two underwater vehicles having hull forms of AFTERBODY1, and AFTERBODY2 which had previously been developed and tested experimentally by Huang et al. (1978). All the turbulence models they used are RANS-based k-ε models, but they differ in their constants’ values and damping functions. The simulations were carried out at the Reynolds number of $6.8x10^6$ for AFTERBODY1 and of $6.6x10^6$ for AFTERBODY2. They found that the k-epsilon AKN turbulence model can predict the hydrodynamic coefficients of the vehicles more accurately than the other two models. Later in 2009 Jagadeesh and Murali measured the hydrodynamic coefficients of the AFTERBODY1 vehicle and verified the numerical solution of the same problem. In the study, they observed the change of the hydrodynamic characteristics of the vehicles by fixing the depth and varying the Reynolds number and angle of attack. As the results suggested, both the drag and lift forces decrease with increasing either the Reynolds number or the angle of attack.

Jagadeesh and Murali (2010) investigated the influence of free surface effects on the hydrodynamic coefficient of an axisymmetric underwater body using Reynolds averaged Navier-Stokes solver. The study focused mainly on the capabilities of turbulence models together with the volume of fluid (VOF) method for hydrodynamic investigation of an axisymmetric underwater body near the free surface. The numerical investigations were carried out to simulate measured hydrodynamic coefficients for several experimental parameters, including velocity variations from 0.4 m/s ($Re=2.12x10^5$) to 1.4 m/s ($Re=7.42x10^5$), depth of submergence from 0.75D to 4.0D, and angle of attack 0° to 15° on a vertical plane for a model scale of 1:2. They found that k-ε Realizable model together with the VOF method consistently provided superior performance in predicting the free surface wave effects on hydrodynamic coefficients for the axisymmetric underwater body model. They observed that as submergence depth ratio *h/D* decreases from 2.0 to 0.75, the C_D value increases by 24.6% for Fr=0.38, and that C_D remains almost constant for the relative submergence depth, *h/D*>2.0. Also, they observed that at higher angles of attack, the C_D value increases as the relative submergence depth (*h/D*) decreases from 2.0 to 0.75. However, the rate of increase is lower than that of smaller angles of attack.

Lin and Huang (2010) employed a Lagrangian frame numerical method to investigate two-dimensional free-surface flow induced by a submerged moving cylinder. As the Froude number increases the free surface distortion becomes considerably larger, and its effects on the wake formation and force coefficient are also larger. They observed that free surface distortion causes the wake to become much more asymmetric downstream, which lead to the variations of lift coefficient.

Pan et al. (2012) investigated the hydrodynamic coefficients of the submarine by numerical simulations. They simulated the oblique towing experiment and the planer Motion mechanism experiment performed on the SUBOFF submarine model using Reynolds Averaged Navier-Stokes (RANS) models. They also adopted the dynamic mesh method to simulate the maneuvering motions of pure heaving, pure swaying, pure pitching and pure yawing. They verified the computational results by comparing them with experimental data and recommended the dynamic mesh method to be used for estimating the hydrodynamic derivatives of a fully appended submarine.

Shao, et al. (2013) studied the force distributions on a surface-piercing yawed cylinder surface in a steady flow condition. They established a numerical model for a flow pass the surface-piercing yawed cylinder with yaw angles ranges from -45° to 45° and solved it using standard large-eddy simulation (LES) methodology. They found that the time-averaged total drag coefficient for all cases increases with the increase of yaw angle compared to that of the surface-piercing vertical cylinder, even over 2.5 for the ±45°-yawed cylinders. They reported the unbalanced hydrostatic pressures on the inclined section are mainly responsible for those increments and decrements.

Allston et al. (2014) investigated experimentally the wake region created by hydrofoil of autonomous underwater vehicles. They examined a parameter space of four flow speeds and five angles of attack. They obtained the results from laboratory experiments using particle image velocimetry of a full-scale prototype in a large flume tank and compared the results with 2-D numerical simulations.

Mansoorzadeh and Javanmard (2014) investigated the effect of free surface on drag and lift coefficients of an Autonomous Underwater vehicle., two-phase flow Reynolds Averaged Navier-Stokes equations were solved using computational fluid dynamics. They compared the numerical results with those obtained from both numerical single-phase flow simulations and the experiments conducted in the towing tank using the 1:1 scale model of AUV. They conducted the study at various submergence depth ratios ranging from 0.87 to 5.22 of the AUV diameter and at the speeds of 1.5 m/s and 2.5 m/s corresponding to Reynolds numbers of 1.9 and 3.17 million, respectively. They showed that the variation of drag and lift coefficients of the AUV with the submergence depth to be very sensitive to the AUV speed.

Goktepeli et al. (2016) obtained drag coefficients for torpedo-like geometries experimentally using an open wind tunnel for Reynolds numbers between Re=6.6x10^4 and Re=33.1x10^4. They changed the nose structures between elliptical, spherical and swaged and tails between wingless, 3 winged and 4 winged structures along with the length/diameter ratio of the model. As a result, they found that the drag coefficient decreases with increasing the Reynolds number for all cases and concluded that the swaged nose was the most efficient nose among the studied nose geometries. In addition, they concluded that addition increasing the length/diameter ratio decreased the drag coefficient.

Kaynarcalioglu (2016) investigated the flow characteristics around a cylindrical geometry with elliptical and semi-elliptical noses using PIV and CFD. His experimental investigation was carried out for Reynolds numbers, Re = 3.2x10^4 and 6.4x10^4 at various angles of attack and numerical study was carried out for $0.1 \leq Ma \leq 4.0$ using the LES turbulence model. He observed that while an oblique shock wave occurs on the nose of the elliptical geometry, two oblique shock waves occur due to the sharpness of the taper on the nose and the semi-elliptical geometry. In this way, the surface friction was kept to a minimum by reducing the drag coefficient by increasing the density in these areas with the impact of a shock wave.

Yagmur (2016) carried out numerical and experimental studies on the flow structure of torpedo-like geometries under free-stream flow conditions. He changed the angle of attack of the model between α = 0°, 4°, 8°, 12° and Reynolds numbers between Re=2x10^4 and 4x10^4. After comparing the results of Large Eddy Simulation (LES), k-ε RNG and k-ω SST turbulence models with the PIV results and concluded that the LES turbulence model gave more satisfactory results. He performed subsequent numerical studies with the LES model and obtained drag coefficients for their reference model placed at α = 0°, without wings as C_D = 0.2278 and C_D = 0.1665 for Re=20x10^3 and 40x10^3 respectively.

Dubbioso et al. (2017) discussed the maneuverability of a submarine in the case of Re = 6.36×10^6 using CFD solver based on unsteady RANS equations. Numerical analyses were performed for Froude number Fr = 0.21 at a depth close to the free water surface. They observed that the wing attached to the tail part of the model has a destabilizing effect in the transient phase.

Salari and Rava (2017) studied numerically the hydrodynamics of an autonomous underwater vehicle by employing the k-e and k-e turbulence models. They performed the study at various Froude numbers and for submergence depth ratios of 0.75 D, 1 D, 1.5 D, 2D, and 4 D. They stated that the free surface of water affects the drag coefficient of the vehicle and that this effect depends on its submergence depth and speed. Also, they observed that the drag near the free surface is larger than the drag at greater depths ($h/D > 3$) and that the flow structure becomes asymmetric as the vehicle moves toward the free surface of the water.

In the study of Doğan et al. (2018), the interaction of the flow structure between the free surface and the wake area of the sphere in an open water channel was presented for different submergence depth ratios in the range of 2.5×10^3 and 10×10^3 of the Reynolds number described by sphere diameter. The Particle Imaging Velocity (PIV) measurements and dye visualization techniques were applied to show flow patterns such as instantaneous and time-averaged velocity field, streamline topology, vorticity, and velocity contours. The sphere is fixed in the range of $0.25 < h/D < 3.0$ downwards from the free surface to a plurality of spherical diameters downwards from the partially submerged position to the free surface. Submergence depth is defined as the ratio of the distance of the sphere lower arm to the free surface of the sphere diameter. Depending on the locations where the sphere is located, the properties of the post-wake region exhibited three different flow events. These; submergence depth ratios for a range of $0.25 < h/D < 1.0$ for a restricted wake area between the uniform flow zone and the free surface, asymmetrical flow due to the free surface effect for the submergence depth for the range of $1.25 < h/D < 2.0$ models and submergence depth are classified as symmetrical flow structures for the range of $2.5 < h/D < 3.0$.

Wu et al. (2019), investigated the effect of the Froude number and immersion rate on free surface wave structures with the Kelvin-Havelock-Peters distant field approach. They examined the effect of the waves formed on the nose and back of the ship on the Fr number theoretically. They have found that the rate of change of the propagation wave depends on the velocity change.

Javanmard et al. (2019) performed numerical simulations to investigate the drag coefficients of an AUV under the effect of struts and free surface. They carried out the simulations for various submergence depth ratios and for Reynolds numbers of 1.9×10^6 and 3.16×10^6. Their results showed that the drag coefficient value of the AUV is reduced with the existence of struts and that the amount of reduction depends on the submergence depth, and Reynolds number.

Tian et al. (2019) studied numerically the effect of free surface waves on the hydrodynamic performance of an autonomous underwater vehicle. They carried out the simulations by utilizing the k-ω SST turbulence model along with the VOF multiphase model which are provided by the ANSYS-FLUENT software. They found that the wave height affects significantly the lift force of the vehicle and that the drag coefficient increases as the submergence depth is decreased.

The examined studies in the literature have different geometries from the present study. This study has been focused on the dye visualization, CFD analysis, partially PIV measurements and all together to yield the distinguished supporting results with each other for four different torpedo-like geometries.

3. MATERIAL AND METHOD

The flow structure around torpedo-like geometries was visualized through the dye flow visualization experiments which performed at the Reynolds numbers (Re = $U_\infty L/\nu$) of $20x10^3$ and $40x10^3$, and for submergence depth ratios (h/D) of 0.75, 1.00, 1.50, 2.0 and 3.0. Then, Particle Image Velocimetry (PIV) method was utilized to measure the instantaneous velocity field of the model and to determine the average velocity field. The PIV experiments were also performed for the same submergence depth ratios and Reynolds numbers considered in the dye flow visualization experiments. On the other hand, the cases for the variation of angles of attack (α = 0°, 4°, 8°, and 12°), and the submergence depth ratios (h/D = 0.5, 0.75, 1.00, 1.50, 2.0, 3.0 and 3.5) were investigated numerically by utilizing Large Eddy Simulation (LES), and Volume-of-fluid (VOF) models provided by ANSYS FLUENT 17.2. The following sections describe the studied models of the torpedo-like vehicle as well as the problem setup for the experimental and numerical work.

3.1. Models of Torpedo-Like Geometries

The hull of torpedo-like underwater vehicles is based on an axisymmetric body which comprises three sections; the Nose, Mid-section, and Stern. In general, the mid-section has a cylindrical form, whereas the nose and stern have a profile of ellipse, sphere, or parabola. The torpedo-like geometry considered here has a length (L) of 200 mm and consists of an elliptical (cambered) nose having a minor diameter (D_f) of 45 mm, cylindrical mid-section with a diameter (D_c) of 40mm, and stern of length (L_a) 80 mm (Figure 3.1). Profiles of the nose and mid-section of the torpedo-like geometry, are defined by the following equations:

$$y_f = \frac{D_f}{2} \cdot \sqrt{1 - \left(\frac{x-40}{40}\right)^2} \qquad 0 < x \le L_f \qquad (3.1)$$

$$y_c = \pm 20 \qquad L_f < x \le L_a \qquad (3.2)$$

where, L_f is the length of the nose ($L_f = 0.229D_f + 40$), L_c is the length of the mid-section ($L_c = L - L_a - L_f$), and the y coordinates are all in millimeters.

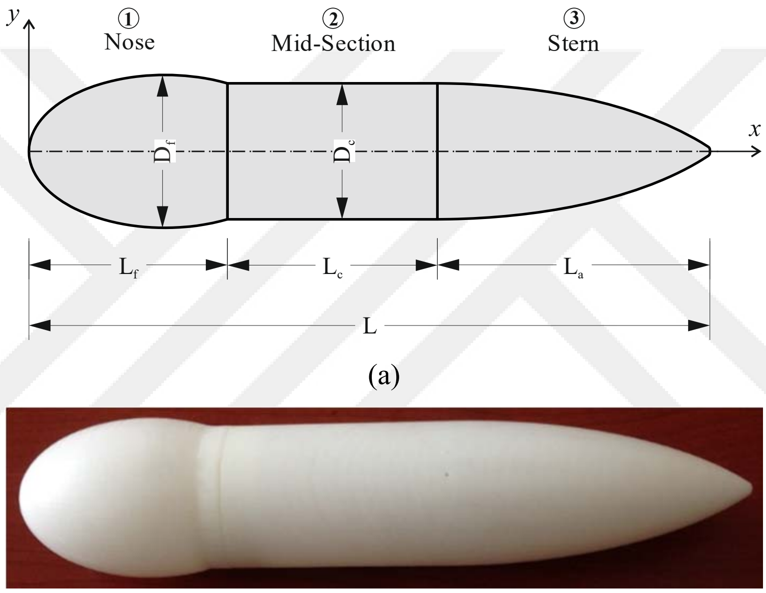

(a)

(b)

Figure 3.1. (a) The geometrical definition of Torpedo-like geometry, and (b) the photograph of the manufactured model

For the stern section two different profiles were considered; The Stern-I which is defined by an ellipse having a major diameter (D_1) of 188 mm and minor diameter (D_2) of 80 mm, and Stern-II which is defined by an ellipse with diameters D_1= 160 mm and D_2 = 40 mm. The two profiles of stern sections are given by the following equation:

$$y_a = \frac{D_2}{2} \cdot \sqrt{1 - \left(\frac{2}{D_1} \cdot (x + L - L_a)\right)^2} \qquad L_c < x \leq L \qquad (3.3)$$

Furthermore, the effect of adding three, and four wings to the torpedo-like geometry having Stern-I were examined. Each of the wings has the design as shown in Figure 3.3, and its dimensions are as follows: $a = 18\,mm$, $b = 0.8825\,a$, $c = 9\,mm$, α =45°, $d = 8\,mm$, $t = 1.2\,mm$. Figure 3.4 shows the isometric view of torpedo-like geometries that have considered in this work.

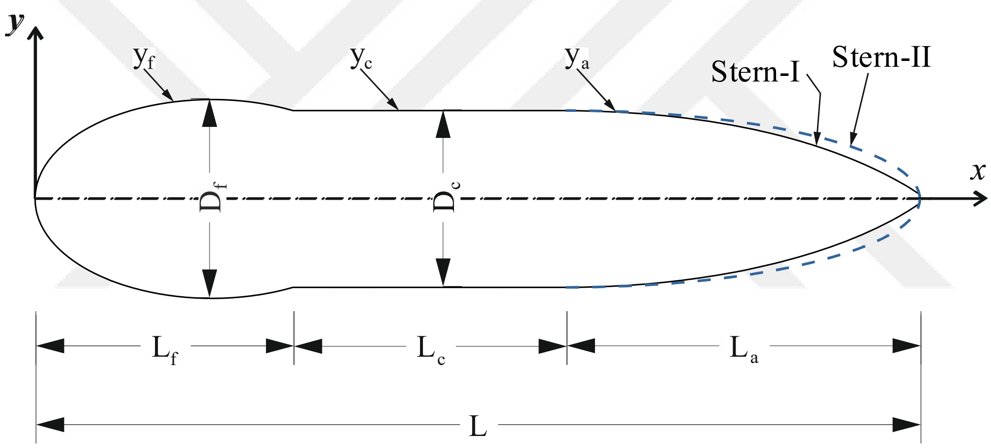

Figure 3.2. The two stern profiles (Stern-I and Stern-II) of the torpedo-like geometry

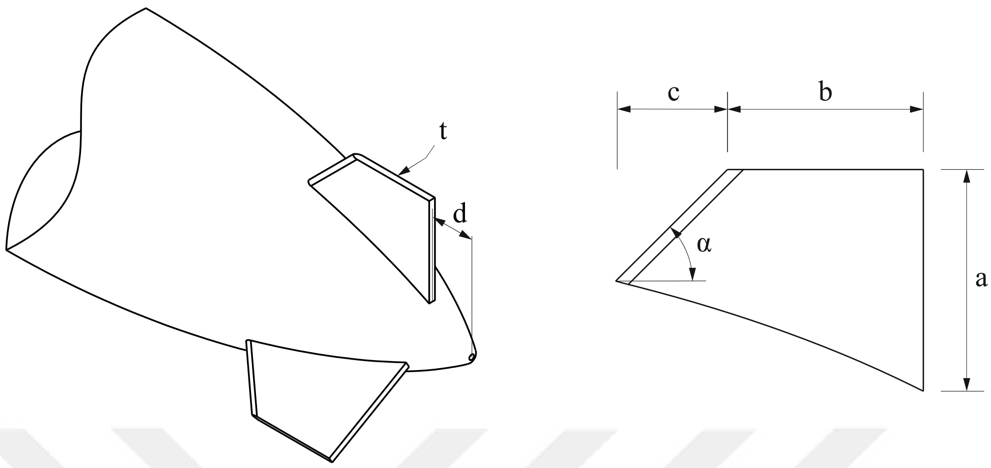

Figure 3.3. The Wing dimensions attached to the Stern-I

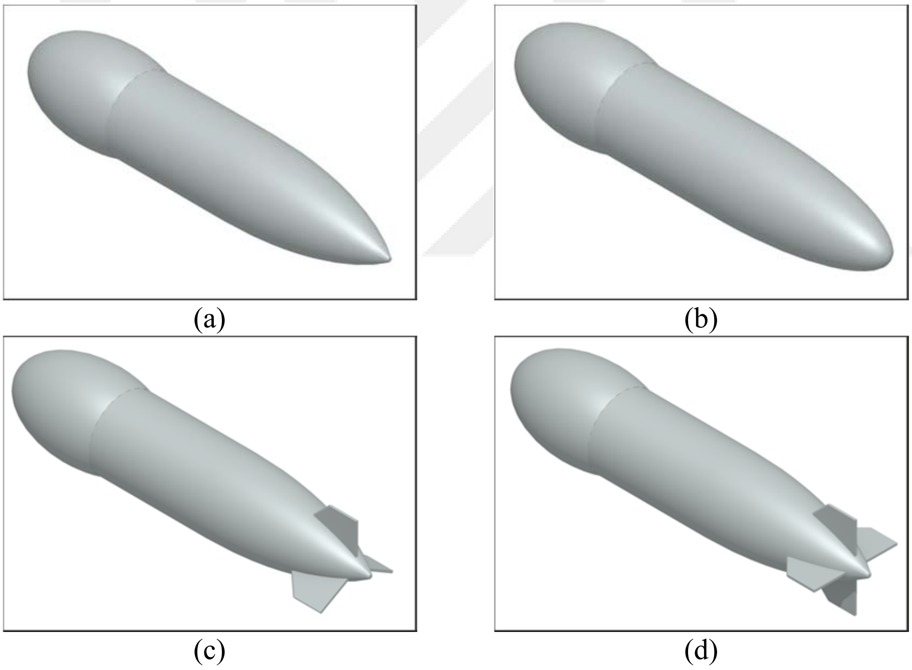

Figure 3.4. Isometric views of torpedo-like geometries which have cambered nose section and stern section of type; (a) Stern-I, (b) Stern-II, (c) 3-winged Stern-I, (d) 4- winged Stern-I

3.2. Experimental Setup

The experiments of dye flow visualization and Particle image velocimetry were carried out in a large-scale water channel located in the Fluid Mechanics Laboratory at Çukurova University. The water channel test section is constructed of transparent Plexiglas with a thickness of 15 mm with upstream and downstream fiberglass reservoirs, and the channel has the following dimension: a length of 8000 mm, a width of 1000mm, and a height of 750 mm. The water channel system has 2 tanks; one of them is situated at the inlet and the other one at the outlet of the channel as shown in Figure 3.5. Two sets of honeycombs were placed in the water channel before the test region where contraction of 2:1 is present to regulate the upstream flow. The design of the channel with a double honeycomb ensures low turbulence intensity. Circulation of water was provided with a water pump having a frequency control unit and power of 15 kW.

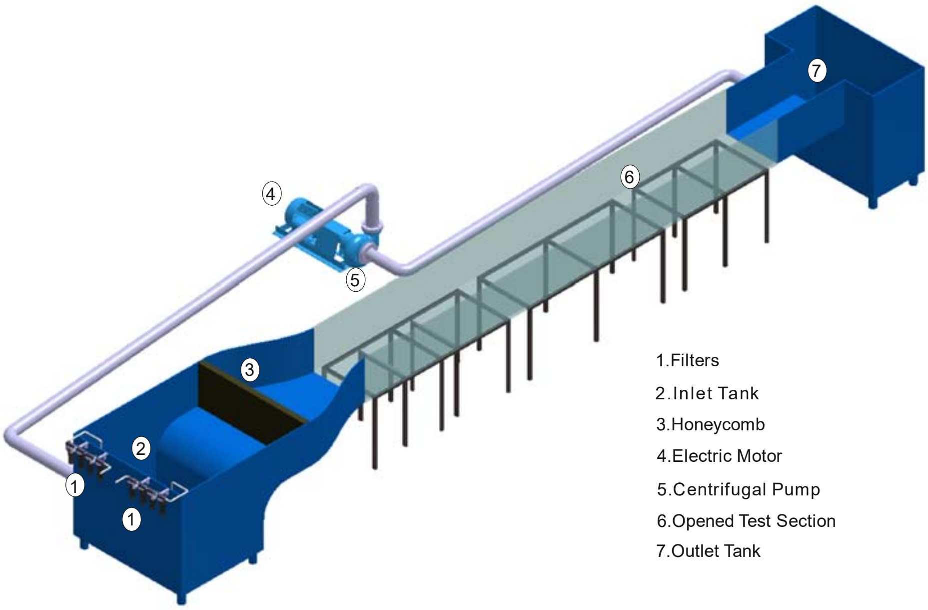

Figure 3.5. Schematic representation of the water channel

Froude number (Fr) is an important dimensionless number that needs to be considered whenever the wave propagation and the free surface interaction is to be examined. The Froude number relates the inertia force to the gravitational force and is defined as $Fr = u_\infty/\sqrt{g\,d}$, where u_∞ is the free-stream velocity, g is the gravitational acceleration, and d is the distance from the free-surface to the bottom of the channel. Depending on the value of Fr, the open-channel flow may be subcritical (Fr << 1), critical (Fr = 1), or supercritical (Fr >> 1). The Froude number of the water channel used to perform the experiments were calculated for water column height of 0.49m as follows: Fr = 0.046 for Re=$20x10^3$ and Fr = 0.091 for Re = $40x10^3$. Since the calculated values are significantly lower than the critical value of Fr=1, the free-surface deformation, and wave propagation is negligible.

3.2.1. Dye Flow Visualization Experiment

The dye visualization technique is defined as the method which gives preliminary or qualitative information about flow structures. In the present study, dye experiments were performed by using a fluorescent dye that changes color and shines under the laser sheet. The fluorescent dye is arranged by mixing powder of Rhodamine 6G with water. Dye was injected in the test region by taking advantage of fluorescent dye reservoir height. Furthermore, a continuous type of laser (Spectra-Physics) unit was used to illuminate the dye. The laser sheet was set parallel to the flow direction and through the longitudinal vertical plane of torpedo-like geometry. Flow structure was observed by ejecting Rhodamine 6G dye which was illuminated by a laser sheet in the test region. Images of the hydrodynamics of flow structures were recorded with a SONY HD-SR1 video camera and Sony Play Memories Software was used to capture the picture of instantaneous flow data. During the dye flow visualization experiments, the Reynolds number was taken as Re = $20x10^3$ and Re = $40x10^3$ with corresponding free-stream velocities of 0.1 and 0.2 m/s. The distance between free-surface and the longitudinal horizontal plane of the torpedo-like geometry referred to as submergence depth ratio was normalized with the diameter of mid-section part of torpedo-like geometry. The submergence depth ratios, h/D, considered for dye experiments are 0.75, 1.00, 1.50, 2.00, and 3.00. Figure 3.6 shows the experimental set-up of dye flow visualization experiments.

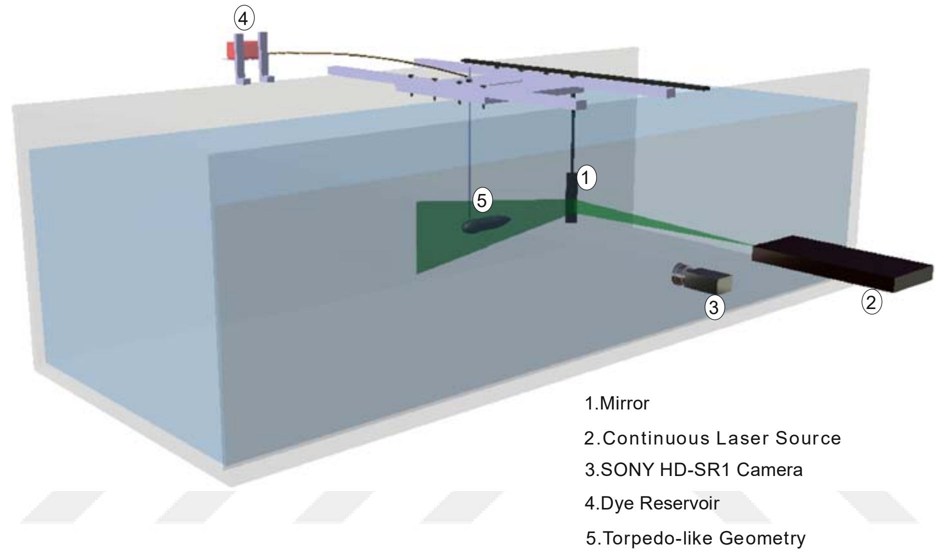

Figure 3.6. Setup used in dye visualization experiment

3.2.2. Particle Image Velocimetry Experiment

The Particle Image Velocimetry technique is one of the most reliable methods for flow velocity measurement in modern fluid mechanics. It is an optical method of velocity measurement which provides information about flow structures by measuring instantaneous velocity vectors over a certain flow field at the same time. Also, the procedure of capturing two images by the PIV technique at a specified time interval is shown in Figure 3.7. Bright and coated silver particles which have 10-micron diameter are mixed with water for instantaneous flow data measurements. Although the density of particles (1100 kg/m^3) is slightly higher than water density, they move at the same velocity with water to demonstrate particular movements of water flows. In the case of instantaneous velocity measurements since the distance between 2 pictures of the same particles in the flow field is known, the instantaneous velocity vector is calculated by the equation $V = \Delta x / \Delta t$.

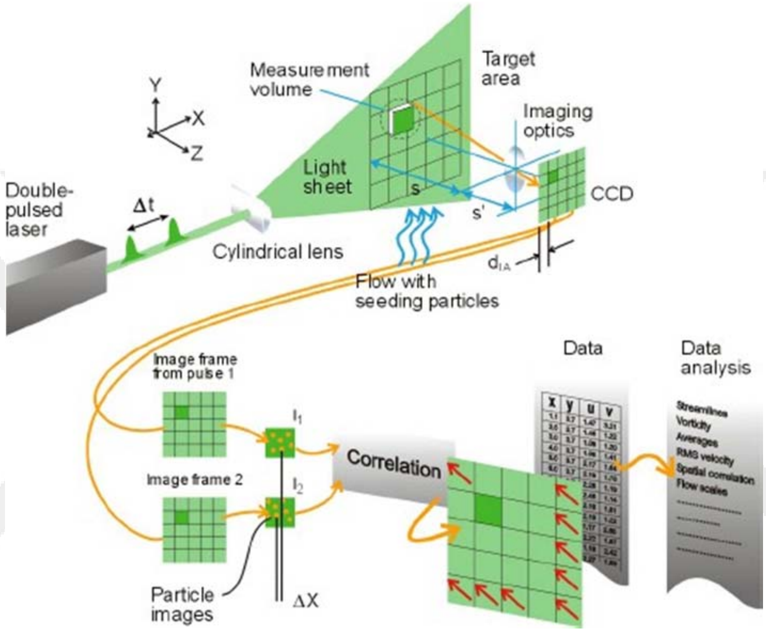

Figure 3.7. The working principle of PIV (Anonymous, 2019d)

Laser sheet which is created by a double-pulse laser source, Nd: YAG Laser (Neodymium-Doped Yttrium Aluminum Garnet) has a thickness of 1-2 mm with a width via optical devices. A double pulse laser source and camera must work simultaneously without a time shift. Therefore, synchronizer controlled by a computer unit exists on the PIV system. The laser source must provide laser light to illuminate seeding particles in the test region. Charged Couple Device (CCD) camera is used to capture images of the observed flow field illuminated by laser light. When CCD camera is set to work at a double frame mode, it determines the instantaneous velocity field through correlating two images, frame 1 and frame 2. Once the instantaneous velocity field is measured, the time-averaged velocity vectors, patterns of streamlines, vorticity concentrations, and turbulence statistics are calculated which provide a physical characteristic of the flow structures.

The field of view (observed field by the camera) is divided into small areas, where each area is called an “interrogation area”. Each interrogation area should have enough numbers of particles for accurate measurements. Therefore, the distribution of seeding particles is an important factor to account for in order to have the instantaneous velocity field accurately measured. Otherwise, a nonhomogeneous distribution of seeding particles may cause higher errors in readings.

The experiments for determining velocity field using PIV method were performed at Reynolds number of $20x10^3$ which corresponds to the free-stream velocity of 0.1 m/s. The submergence depth ratios, h/D, considered for PIV experiments are 0.75, 1.00, 1.50, 2.00, and 3.00. The side and top views of the experimental setup are shown schematically in Figure 3.8. The images were acquired by an 8-bit CCD camera having a resolution of $1200x1800$ pixels, and then were processed with interrogation areas of 32x32 pixels, and an overlap of 50%. Each processed image had a 2D grid size of 1.54 x 1.54mm² (0.038D x 0.038D), and total velocity vectors of 7326 (99x74). After removing the bad vectors using CLEANVEC PIV vector validation software, developed by Steven M. Soloff and Carl D. Meinhart (1999), the sampled-averaged velocity field was calculated using in-house program NWENSAV2 (Lin J. , 1996).

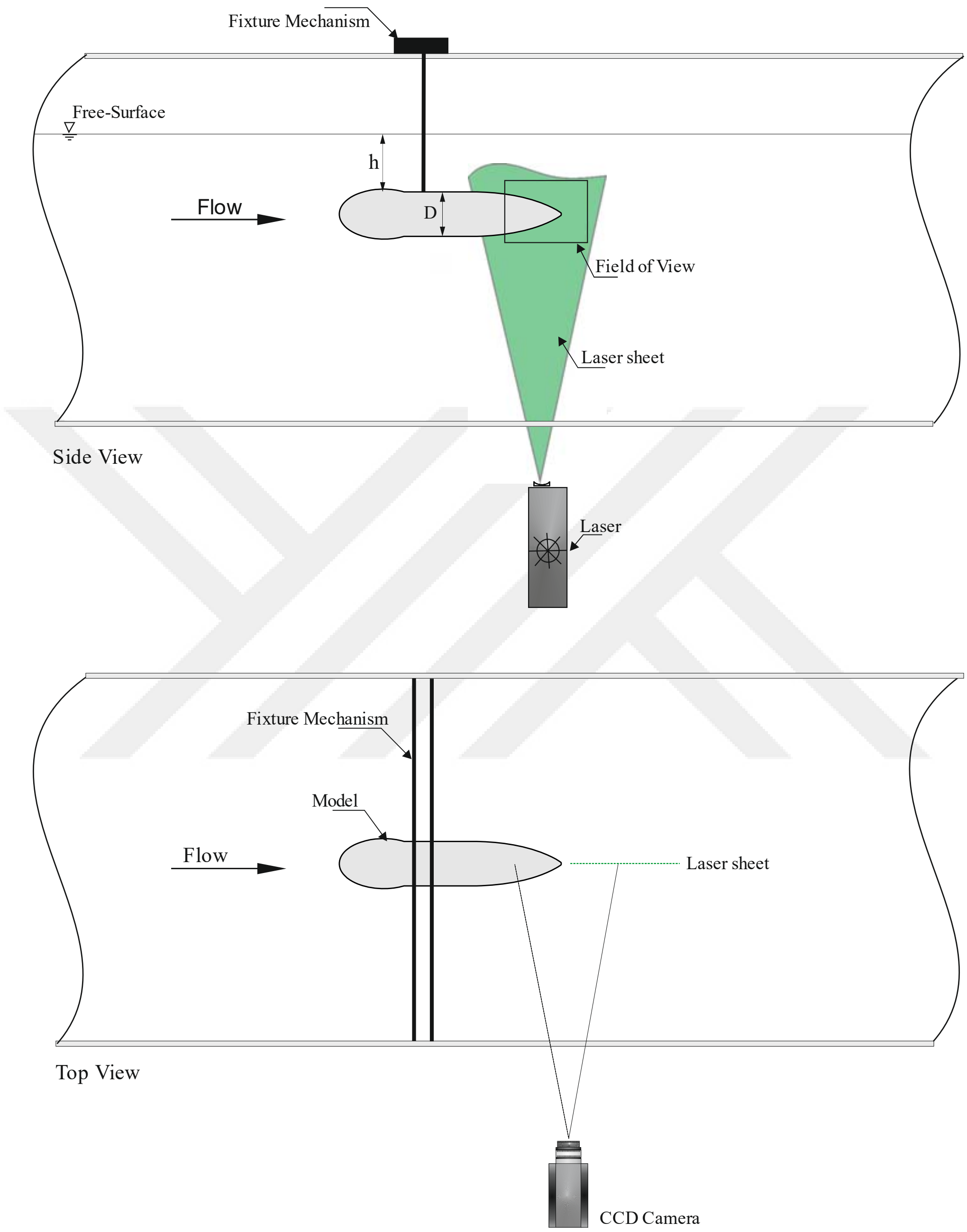

Figure 3.8. Setup for velocity measurement by PIV method

3.3. Numerical Setup

The numerical study carried out using the ANSYS-FLUENT software, which is used generally to model fluid flow, heat transfer, and chemical reactions in complex geometries. The package is written in C computer language giving it the ability to handle efficiently dynamic memory allocation, data structures, and solver control. The software package provides complete mesh flexibility, including the ability to solve problems using unstructured meshes that can be generated about complex geometries. The ANSYS-FLUENT software utilizes the finite volume method (FVM) to discretize the conservation equations. The FVM is a discretization approach in which an integral form of the conservation equations is converted to a set of algebraic equations that can be solved numerically. The integral form of a general conservation equation for the transport of a quantity, ϕ in an arbitrary fluid volume, Ω is given as follows:

$$\int_{\Omega} \frac{\partial}{\partial t}(\rho\phi)d\Omega + \oint \rho\phi\, \vec{\boldsymbol{V}} \cdot d\vec{\boldsymbol{A}} = \oint \Gamma_{\phi}\, \boldsymbol{\nabla}\phi \cdot d\vec{\boldsymbol{A}} + \int_{\Omega} S_{\phi} \cdot d\Omega \qquad (3.4)$$

where ρ = density, $\vec{V}$ = velocity vector, $\vec{A}$ = surface area vector, Γ_{ϕ} = diffusion coefficient for ϕ, and S_{ϕ} = source of ϕ per unit volume. If the quantity ϕ is set to one then the equation (3.4) represents the mass conservation equation, and if $\phi = \vec{V}$ then the equation becomes the momentum conservation equation. More information and technical details about the finite volume method (FVM) and its application to the conservation equation are given by Ferziger (2002).

3.3.1. The Fluid Domain and The Mesh

The dimensions of the fluid domain considered for the numerical study of the prescribed models are as following; 37.5D in the x-direction, 8D in the y-direction, and z-direction. The torpedo-like geometry was placed at 7.5D from the inlet boundary, at 4D from the channel bottom, and at 4D from the sides. The blockage ratio of the fluid domain is less than 1.4% depending on the angle of attack. The schematic representation of the domain is given in Figure 3.9.

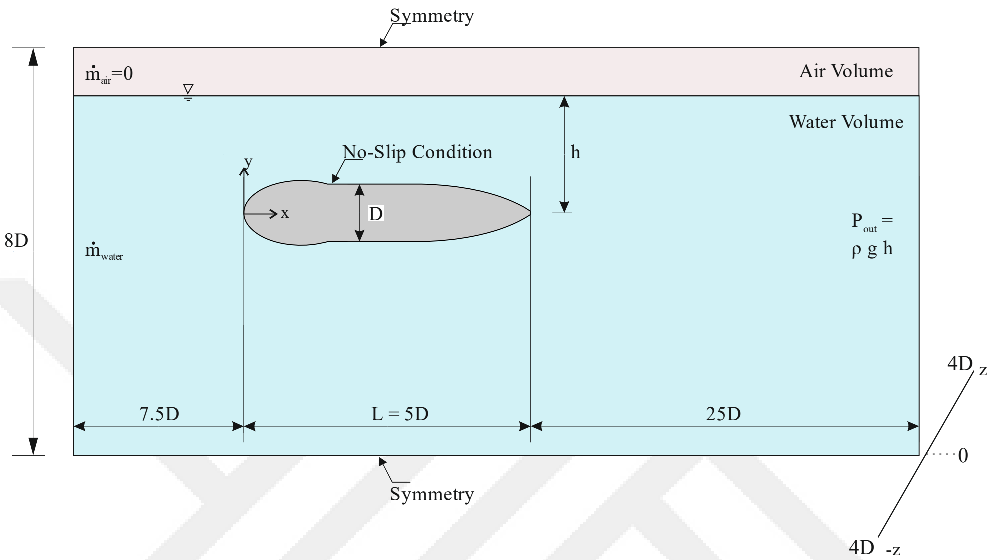

Figure 3.9. Fluid Domain dimension and assigned boundaries used in the numerical study

The domain was initially discretized into small tetrahedron control volumes (around 11 million elements) using the ANSYS Mesh Modeler, and later they were converted into polyhedron using the ANSYS-FLUENT software. After the conversion process, the polyhedron mesh contained around 3 million elements (Figure 3.10) for each model. To reduce discretization errors the size of control volumes was controlled by subdividing the whole fluid domain into three subdomains. The largest domain has control volumes in a size of 10 mm, the smaller domain has a control volume in a size of 5 mm, and the smallest domain has control volumes in a size of 1 mm. Also, to resolve the viscous sublayer ($y^+ < 1$), the control volumes around the models were refined by creating prism layers of control volumes that produce an average y^+ less than unity.

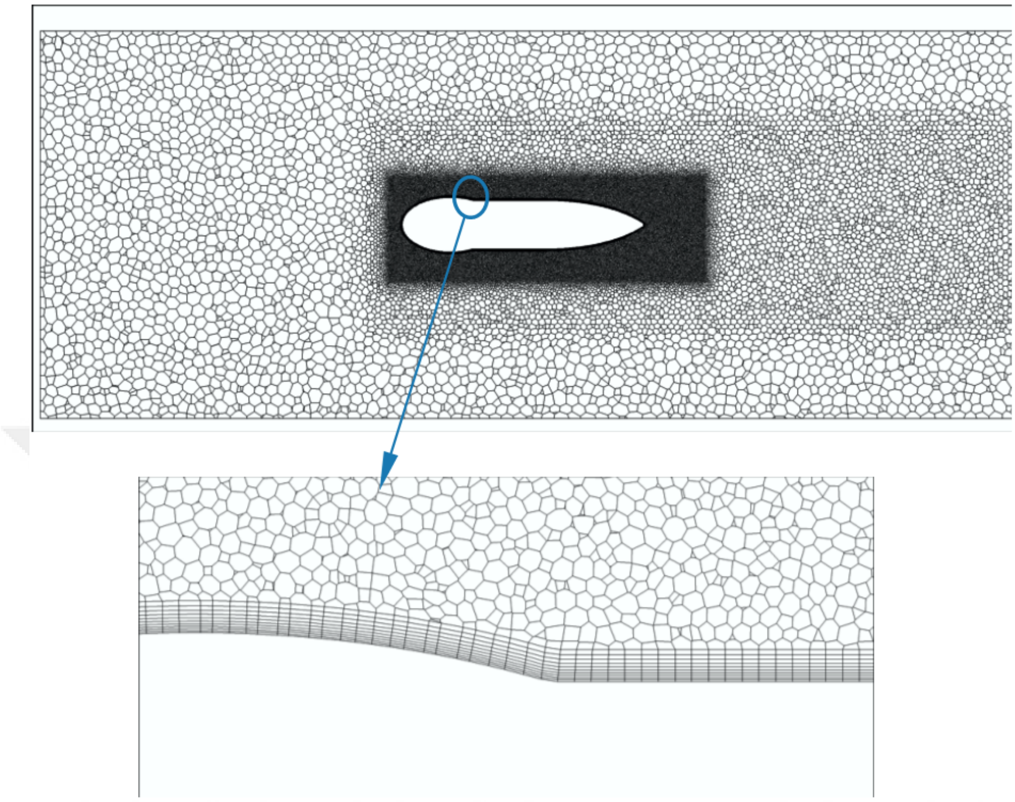

Figure 3.10. The generated mesh structured for the numerical study

3.3.2. Mathematical models

The flow around the models considered in this study is basically turbulent, thus, a suitable turbulence model should be selected regarding the cost of both time and resources even though Reynolds numbers were chosen as $Re=20x10^3$, and $Re=40x10^3$. The simulation of turbulent flows by numerically solving the Navier-Stokes equations requires resolving a very wide range of time and length scales, all of which affect the flow field. Such resolutions can be achieved with direct numerical simulation (DNS). However, DNS is computationally expensive, and its cost prohibits simulation of practical engineering systems with complex geometry or flow configurations. The other alternative is to perform a Large-Eddy Simulation (LES). The principal idea behind LES is to reduce the computational cost by ignoring the smallest length scales, which are the most computationally expensive to resolve, via low-pass filtering of the Navier–Stokes equations. Such low-pass filtering, which can be viewed as a time- and spatial-averaging, remove effectively the small-scale information from the numerical solution. Therefore, the large eddy simulation (LES) were selected in this study to analyze all the prescribed models. Also, another model should be incorporated into the solver in order to allow the study of the free-surface effect. For this purpose, the Volume-of-Fraction multiphase model was used. The following are more details about the numerical models (ANSYS, 2017).

3.3.2.1 Large Eddy Simulation Turbulence Model

Navier-Stokes and continuity equations, which are the general equations of fluid mechanics, are used in the modeling of turbulence flows. the filtered equations of Continuity and Navier-Stokes for incompressible flow are as followings:

$$\frac{\partial \bar{u}_i}{\partial x_i} = 0 \quad (3.5)$$

$$\frac{\partial \bar{u}_i}{\partial t} + \frac{\partial \bar{u}_i \bar{u}_j}{\partial x_i} = \frac{1}{\rho} \cdot \frac{\partial \bar{p}}{\partial x_i} - \frac{\partial \tau_{ij}}{\partial x_j} + \nu \frac{\partial^2 \bar{u}_i}{\partial x_i \partial x_j} \quad (3.6)$$

where, u_i is the velocity variable that is filtered through the Cartesian coordinate x_i, p is the pressure of the liquid, ρ is the density of the fluid and v is the kinematic viscosity of the liquid. In the LES turbulence model, equations that characterize large-scale vortices are primarily used. The fundamental principle of the LES turbulence model is based on sub-grid filtering. Using this process, small-scale vortices in the Navier-Stokes equations are eliminated, the average flow is modeled, large-scale vortices are captured, and the remaining small-scale vortices are estimated using the stated parameters. The LES turbulence model uses filtering techniques to distinguish these large-scale and small-scale vortices (Kim, Wilson,

& Chen, 2015). In equation (3.7, the Navier-Stokes equation is applied to the filtering technique. In this equation, the effect of small vortices on large vortices in small-scale stress tensors is calculated as;

$$\tau_{ij} = \overline{u_i u_j} - \bar{u}_i \bar{u}_j \quad (3.7)$$

Here we need to identify unknown and subgrid models based on the eddy viscosity approach:

$$\tau_{ij} - \frac{1}{3} \tau_{kk} \delta_{ij} = -2 \mu_t \bar{S}_{ij} \quad (3.8)$$

The stress residues on the subgrid-scale are presented in the adjusted pressure term after the results of the τkk pressure assessment. The μt is the viscosity of the fluid at the subgrid-scale and the $Si\ j$ is the stress rate and is expressed as follows:

$$\bar{S}_{ij} = \frac{1}{2}\left(\frac{\partial \bar{u}_i}{\partial x_j} + \frac{\partial \bar{u}_j}{\partial x_i}\right) \quad (3.9)$$

Basic and best known subgrid-scale models were proposed by Smagorinsky and later by Lilly. The eddy viscosity in both models is expressed as:

$$\mu_t = \rho\, l_s^2 \left|\bar{S}_{ij}\right| \quad (3.10)$$

In this equation l_s indicates the length of the fluid in the field of motion, and if the stress rate is expressed as:

$$\bar{S}_{ij} = \sqrt{\bar{S}_{ij}\bar{S}_{ji}}\, l_S \quad (3.11)$$

then, l_s is calculated as

$$l_s = \min(Ky, C_s V^{1/3}) \quad (3.12)$$

Here K Von Karman constant, y the distance to the nearest wall, C_s Smagorinsky constant and V is expressed as the volume of the flow to be calculated (ANSYS, 2017).

3.3.2.2 The volume of Fraction (VOF) Multiphase Model

The VOF model is one of the most commonly used interface modeling methods. Interface simulation is difficult because the interface geometry changes over time. This change in geometry is part of the solution. While other methods require the first geometry of the interface to determine the solution, the VOF model aims to solve this interface. The VOF model solves two or more immiscible fluid momentum equations. The volumetric ratio of the phase is specified as a variable within the control volume for each phase defined in the VOF model. The sum of the volumetric ratios of all phases for each control volume is 1. In other words, if the volumetric ratio of the cell within the q^{th} fluid is shown by the α_q, the following three conditions may occur (ANSYS, 2017).

$\alpha_q = 0$: The cell is empty (of the q^{th} fluid)

$\alpha_q = 1$: The cell is full (of the q^{th} fluid)

$0 < \alpha_q < 1$: The cell is a mixture of two fluids

Based on the value of α_q, the appropriate properties and variables are assigned to each cell with the domain.

The tracking of the interface between phases is achieved by the solution of a continuity equation for the volume fraction of one of the phases. For the q^{th} phase, this equation has the following form:

$$\frac{1}{\rho}\left[\frac{\partial}{\partial t}\left(\alpha_q \rho_q\right) + \nabla \cdot \left(\alpha_q \rho_q \vec{v_q}\right) = S_{\alpha_q} + \sum_{p=1}^{n}\left(\dot{m}_{pq} - \dot{m}_{qp}\right)\right] \quad (3.13)$$

where $\dot{m}_{qp}$ is the mass transfer from phase q to phase p and $\dot{m}_{pq}$ is the mass transfer from phase p to phase q. By default, the source term S_{α_q} in the equation is zero, but a fixed mass source can be defined for each phase. The volume fraction equation will not be solved for the primary phase; instead, the primary-phase volume fraction is determined based on the basis of the following condition:

$$\sum_{q=1}^{n} \alpha_q = 1 \tag{3.14}$$

The volume fraction equation can be resolved using either an implicit or an explicit scheme. In this study, the implicit scheme was used.

The properties appearing in the transport equations are determined by the presence of the component phases in each control volume. In a two-phase system, for example, if the phases are represented by the subscripts 1 and 2, and if the volume fraction of the second phase is being tracked, the density in each cell is given by

$$\rho = \alpha_2 \rho_2 + (1 - \alpha_2)\rho_1 \tag{3.15}$$

All other properties (e.g., viscosity) are computed in this manner.

3.3.3. Solver Settings

The setup parameters used in the ANSYS-FLUENT are shown in table 04. To investigate the free-surface effect, the VOF sub-model Open Channel Flow was used to define the free-surface height while keeping the torpedo-like geometry fixed within the created fluid domain. The implicit scheme was chosen for its more robust nature. The inlet and outlet were held in one piece instead of separating for each fluid due to the ability of the open channel flow sub-model to separate fluids at a free-surface height. Since the implicit scheme was used, the CFL condition ($C = \Delta t / \Delta x \leq 1$, where Δt is the time step size and Δx is the cell length range) was satisfied according to the range of $C \leq 50$ proposed by the ANSYS-FLUENT software. Time step size was taken as 0.068s to compare with previous CFD studies conducted in the project. Depending on the Reynolds number, and the submergence depth, the CFD analysis lasted between 8 and 36 hours.

Table 3.1. Solver Setup

Solver	Pressure based - Transient
Multiphase Model	• VOF model – Implicit Formulation • Body Force Formulation: Implicit Body Force • VOF Sub-model: Open Channel Flow • Interface Modelling Type: Sharp/Dispersed
Turbulence Model	LES -WALE – C_{wale}=0.326
Material	Phase-1: Air, Phase-2 Water, Surface Tension: Off
Boundary Conditions	• Inlet: Mass-flow inlet $\dot{m}_{air}$ = 0 kg/s, $\dot{m}_{water} = \rho \cdot u_{\infty} \cdot 8D \cdot (4D + h)$ • Outlet: Pressure outlet (hydrostatic pressure profile) • Model Boundary: Wall • All other domain boundaries are symmetry
Operating Conditions	• Specified Operating Density: 1.225 kg/m^3 • Operating Pressure: 1 atm – Gravity -9.81 m/s^2
Reference Values	• A_c: Frontal areas, L = 0.2m • ρ : 998.2 kg/m^3, μ = 0.001003 Pa·s • Velocity: 0.2 m/s for Re=40000, 0.1 m/s for Re=20000
Solution Method	• Scheme: Coupled • Gradient: Least Squares Cell-Based • Pressure: PRESTO! • Momentum: Bounded Central Differencing • Volume Fraction: Compressive • Transient Formulation: Bounded Second-Order Implicit
Monitors	Residual Absolute Criteria: 10^{-4}
Solution Initialization	• Standard Initialization • Open Channel Initialization Method: Flat • X velocity: 0.2 m/s for Re=40000, 0.1 m/s for Re=20000 • Water Volume Fraction: 1
Run Calculation	• Time step size: 0.068 s • Max iterations / time step: 20

4. RESULTS AND DISCUSSION

4.1. Flow Structures around Torpedo-Like Geometry of Stern-I Under the Influence of the Free-Surface

The model of the torpedo-like geometry considered in this section has the Stern-I profile which has defined in equations (3.1, (3.2, and (3.3. The free-surface effect on the flow structure around the model was examined first numerically for two different Reynolds numbers, and then the results were validated with the dye visualization technique, and the measured velocity field using the PIV method. Also, the flow structure was examined for various angles of attack at Re = $40x10^3$.

4.1.1. The Effect of Reynolds Number on The Flow Structures

The image captured from dye experiments for the wake structure at uniform flow condition is given in Figure 4.1. It is observed that for both Reynolds numbers (Re = $20x10^3$, and Re = $40x10^3$) the flow separates from the curve of the nose section at a point where the curve slope becomes negative. However, for Reynolds number of $40x10^3$ the vortex shedding occurs at a higher frequency rate than the Reynolds number, Re = $20x10^3$. The same results were observed also for the same model with 3- and 4-wings i.e. the wings have no effect on the flow structure around the nose, and mid-section parts of the model. On the other hand, the flow over the boundary of the stern section shows separation, and consequently, vortex shedding occurs for both Reynolds numbers, Re = $20x10^3$, and Re = $40x10^3$. Since the fluid momentum is lower at Re = $20x10^3$, the flow separates earlier than it does at Re = $40x10^3$, causing a larger wake region downstream of the model geometry. Also, at Re = $40x10^3$ small scale Kelvin-Helmholtz vortices were formed due to the decreasing stability of the shear layer. The flow structure is controlled by the appending wings for the stern section of the torpedo-like geometry. The wake region of the torpedo-like model with 4 wings appended is effectively controlled and suppressed the vortex shedding and its structure thoroughly.

Dye visualization was also performed at different submergence depth ratios, *h/D* in order to virtualize the flow structure downstream of the model. The results are given in Figure 4.2 show qualitatively how the free-surface affects the wake region downstream of the torpedo-like model for Re = $20x10^3$, and Re = $40x10^3$. It was observed that Kelvin-Helmholtz vortices, dominantly, form around the separated flow after $h/D \geq 1.50$, and that the flow structures obtained for $h/D \geq 1.5$ were similar to the flow structure under the uniform flow conditions given in Figure 4.1. This means that the free surface effect decreases with increasing submergence depth and becomes negligible when $h/D > 2.00$.

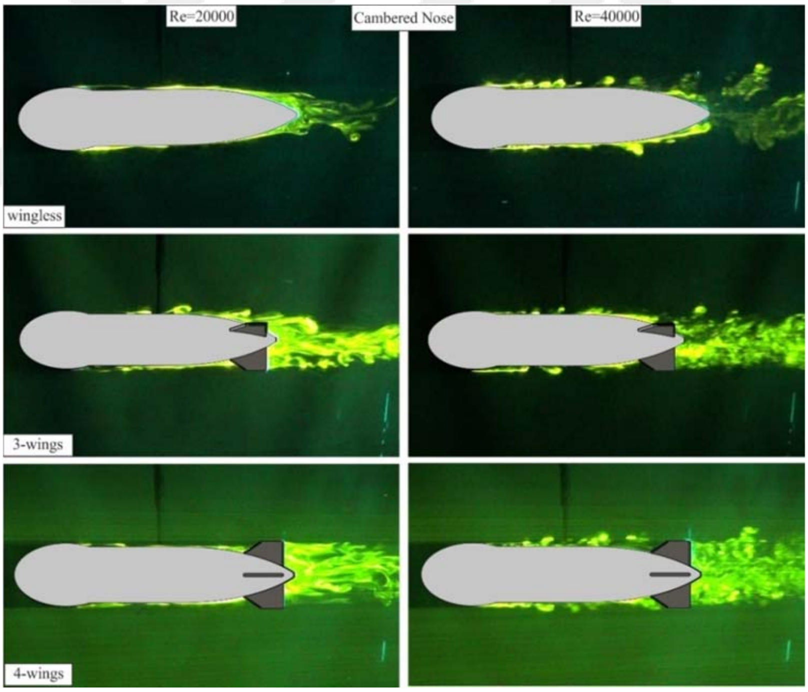

Figure 4.1. Dye visualization of the effect of Reynolds number on the flow structure around the torpedo-like geometry of cambered nose with wingless, 3-winged and 4-winged elliptical stern-I under uniform flow conditions for α = 0°

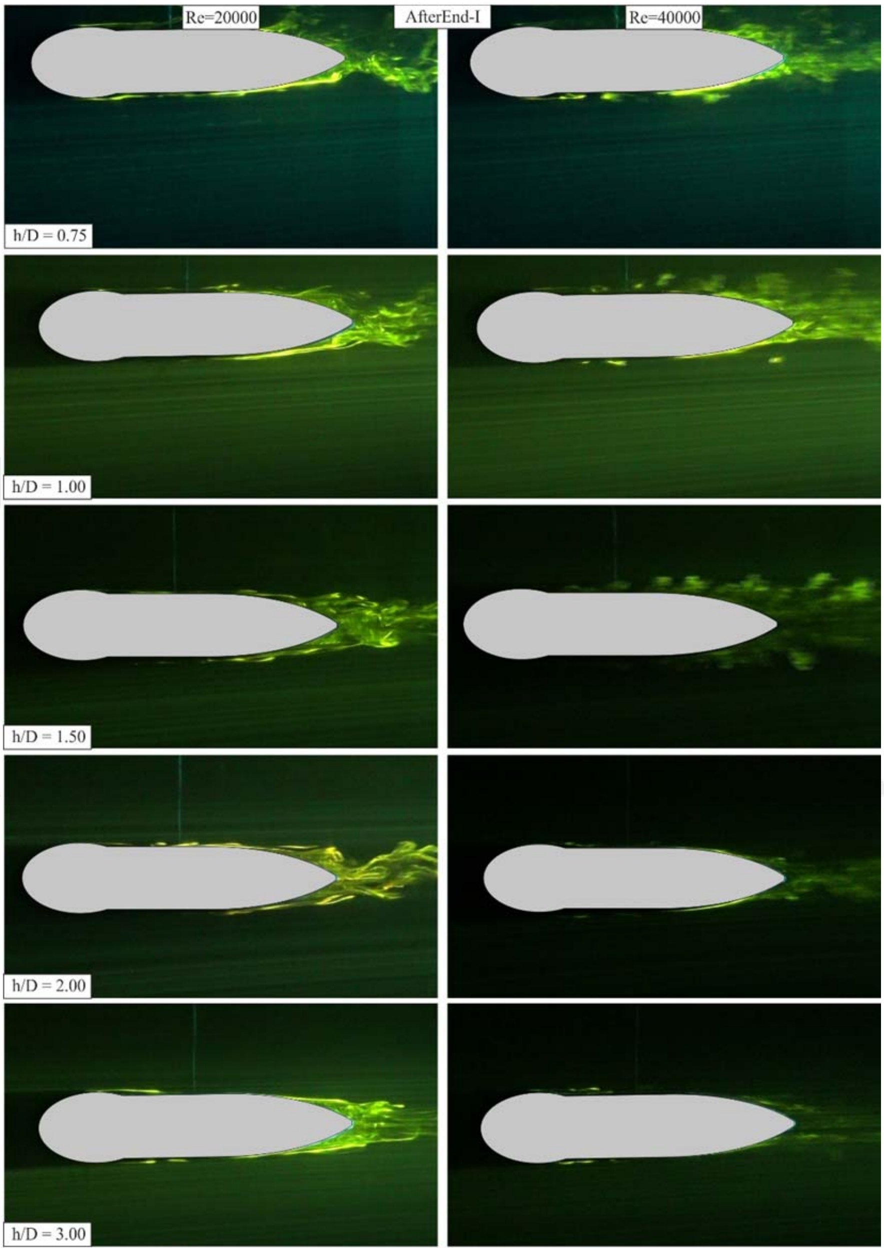

Figure 4.2. Dye visualization of the effect of Reynolds number on the flow structure around the torpedo-like geometry of cambered nose and wingless elliptical stern-I for α = 0° and submergence depth ratios, *h/D* of 0.75, 1.00, 1.50, 2.00, and 3.00

The numerical results obtained from large eddy simulation, and volume-of-fluid method for the submergence depth ratios of *h/D* = 0.75, 1.00, 1.50, 2.00, 3.00 at Re = $20x10^3$, and Re = $40x10^3$are shown in Figures 07 to 10. The contour for the dimensionless streamwise velocity component $<u/U_\infty>$ in the region around the torpedo-like geometry is shown in Figure 4.3. The results show that the free surface effect is higher at Re = $20x10^3$. For submergence depth, *h/D* of 0.75, very low-velocity distributions were observed in the shear layer developed above the torpedo-like geometry. At this depth, the Reynolds number of $20x10^3$ showed even lower values. However, when the depth is increased to *h/D* = 1, a jet-like flow was observed to form in the gap between the free-surface and the upper boundary of the geometry. Since the flow accelerates in the upper region at a higher rate than in the lower region of the wake, the flow structure becomes asymmetric. The effect of the jet-like flow on the wake region decreases with increasing submergence depth, *h/D* and it disappears completely for submergence depth ratios, *h/D* higher than 2 at Re = $40x10^3$, and higher than 3 at Re = $40x10^3$. Also, the results suggest that for *h/D* = 3, the free surface had no effect on flow structure. Figure 4.4 shows the contour of the time-averaged dimensionless velocity component $<v/U_\infty>$ in the normal direction to the free-stream velocity. In the region where *h/D* is close to the free surface, the positive velocity component is lower in the upper part than the lower part of the geometry. This is justified by the formation of jet-like flow in the upper region of the geometry. A near-symmetrical flow structure obtained for *h/D* > 2.5 indicates that the free surface effect decreases by increasing the submergence depth, *h/D*. However, the flow structure doesn't show exact symmetry due to the hydrostatic pressure variation. For submergence depth ratios, *h/D* lower than 2, the formation of jet-like flow in the region between the upper part of the geometry and the free surface causes an increase in the negative velocity which adversely affects the buoyancy force. Figure 4.5 shows the time-averaged dimensionless vorticity $<\omega\, L/U_\infty>$ contour as well as the effect of free-surface on the formed wake region. The vorticity also suggests that the free surface effect gradually decreases as the submergence depth ratio, *h/D* is increased. For *h/D* = 3.50, the shear layer extends to the wake region on both the upper and lower sides of the geometry and similar vorticity distribution observed for Re = 40x10^3 and Re = 20x10^3. However, when the submergence depth ratio decreases to 0.75 the vorticity magnitude of the upper part of the geometry is increased relative to the lower part due to the acceleration of the flow in the region in-between the free surface and the model geometry. Figure 4.6 shows the fluctuations level in the flow field by displaying the contours of the dimensionless turbulent kinetic energy $<TKE/U_\infty^2>$, where $\text{TKE} = 0.5 \cdot \left(\overline{u_x'^2} + \overline{u_y'^2} + \overline{u_z'^2}\right)$. For submergence depth ratios of *h/D* = 0.75 and 1.00, the free surface deformation causes the highest turbulent kinetic energy in the region surrounding the water and air above the geometry. Also, high turbulent kinetic energy values were observed in the wake region of the torpedo-like geometry, indicating that the jet-like flow influences the wake region. On the other hand, as the submergence depth ratio, *h/D* is increased (*h/D* ≥ 1.5) the turbulent high kinetic energy values were observed only in the wake region of the model geometry. The results show that at Re = 40x10^3 the turbulent kinetic energy is higher than those obtained at Re = 20x10^3. This means that the vortex shedding is stronger at Re = 40x10^3. In order to validate the results obtained from the numerical simulations, the results of the PIV experiment are given in Figures 11 to 13. PIV results appear to be consistent with CFD results for Re = 20x10^3. At low submergence depth ratio, *h/D* the wake region became asymmetric due to the jet-like flow. This effect disappears as the submergence depth ratio, *h/D* increases since the area between the free surface and the geometry is increased. Therefore, the averaged flow structure in the wake region became symmetrical for h/D = 3. On the other hand, the PIV results obtained at Re = 40x10^3 show that there is no distinguished wake region for all the submergence depth ratios. This indicates that the results of these cases should be examined in more detail later.

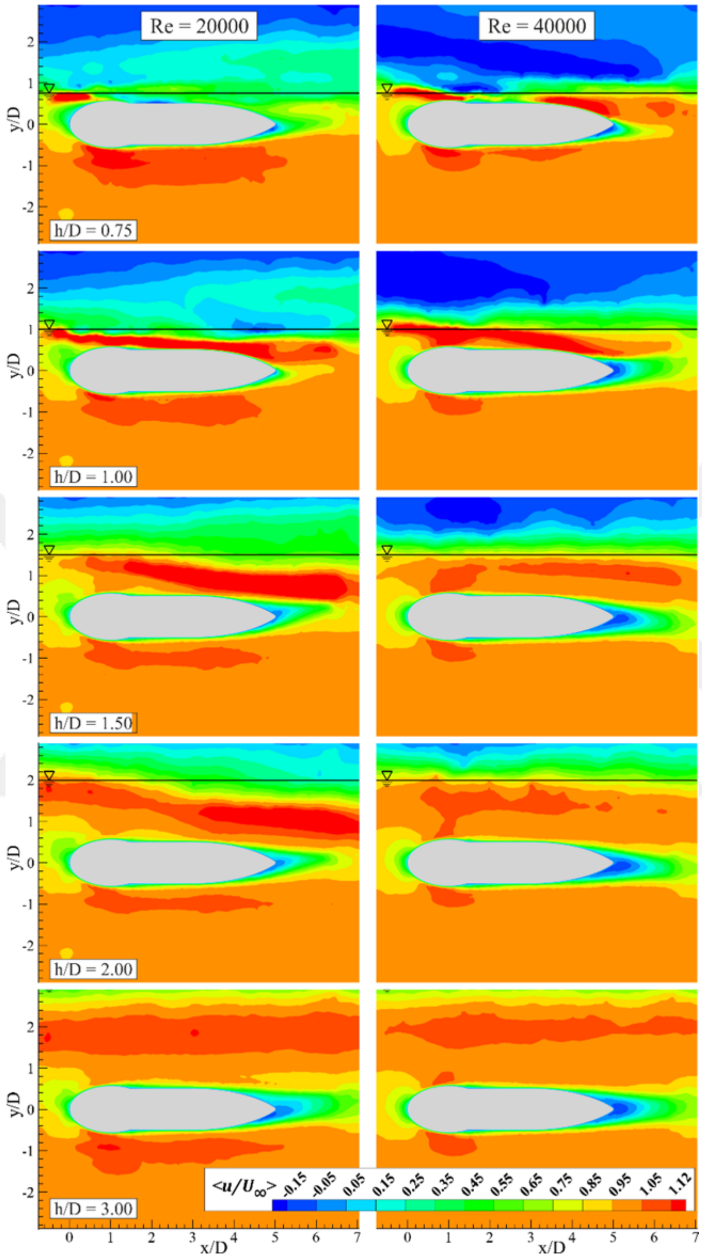

Figure 4.3. Contours of the time-averaged dimensionless streamwise velocity component $<u/U_{\infty}>$ calculated numerically for the torpedo-like geometry of cambered nose and elliptical stern-I without wing at submergence depth ratios, *h/D* of 0.75, 1.0, 1.5, 2.0, 3.0.

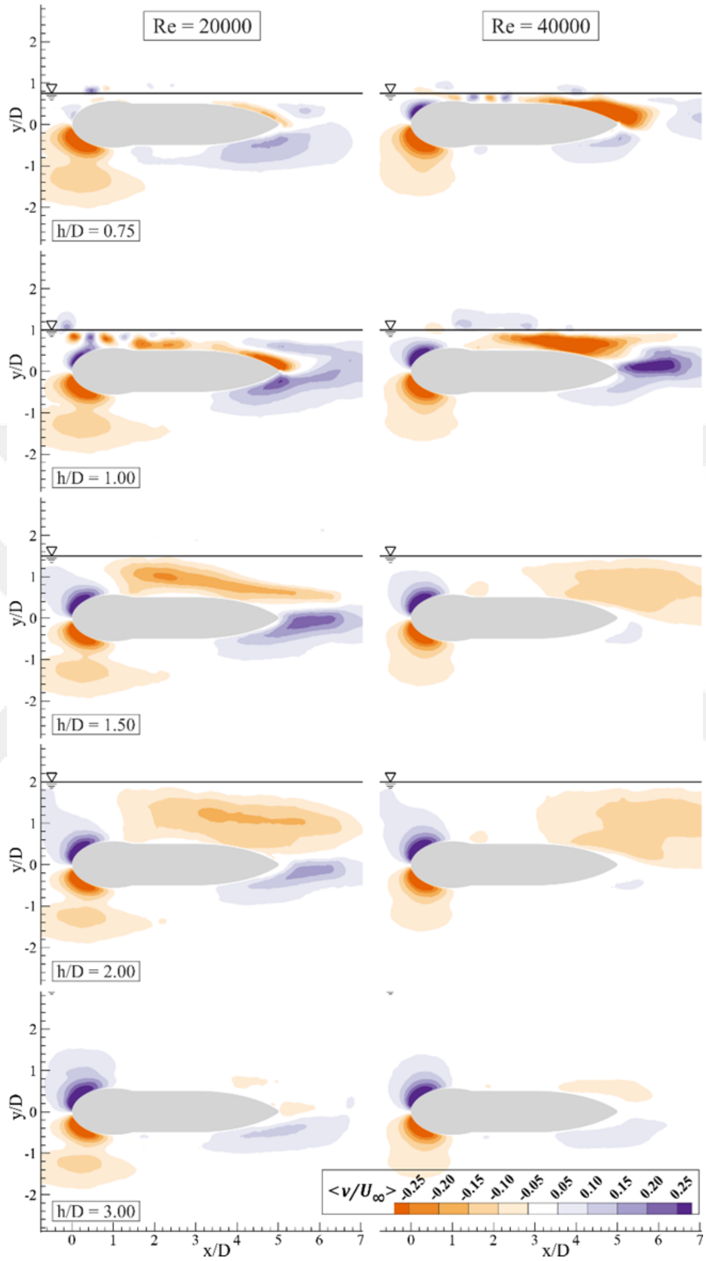

Figure 4.4. Contours of the time-averaged dimensionless crosswise velocity component $<v/U_\infty>$ calculated numerically for the torpedo-like geometry of cambered nose and elliptical stern-I without wing at submergence depth ratios, *h/D* of 0.75, 1.0, 1.5, 2.0, 3.0.

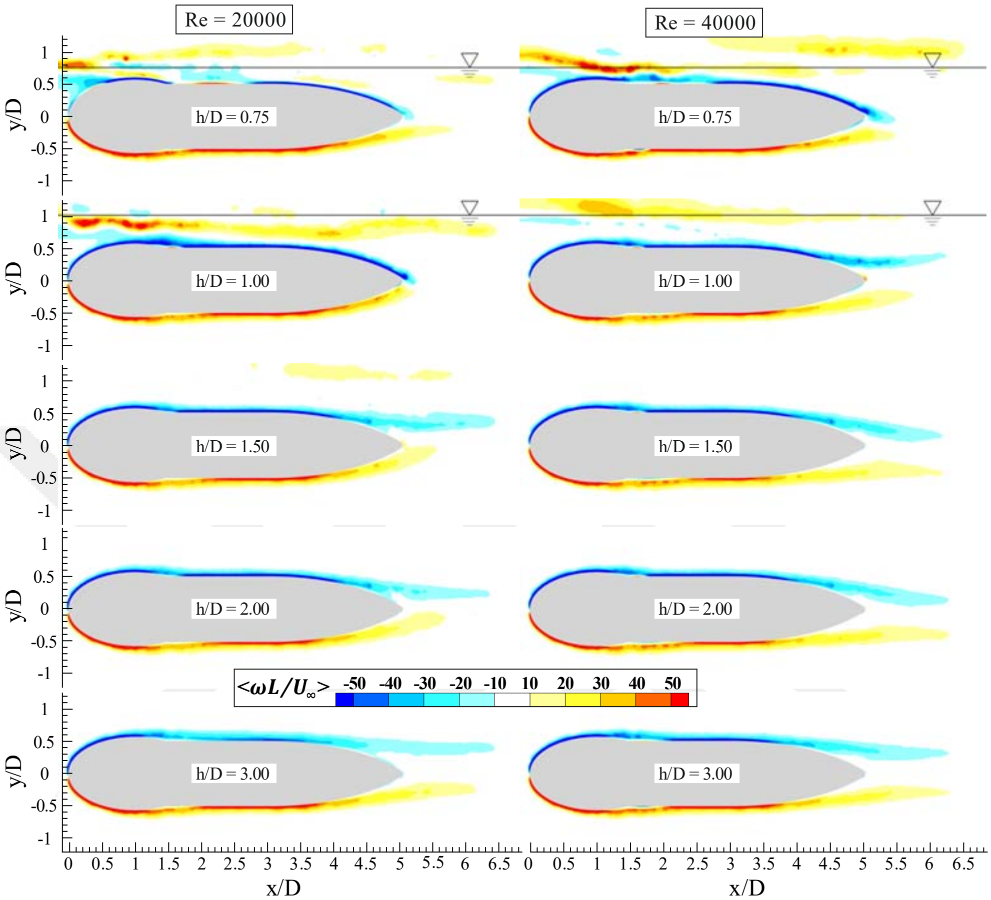

Figure 4.5. Variation of the time-averaged dimensionless vorticity contours $<\omega\, L/U_{\infty}>$ calculated numerically for the torpedo-like geometry of cambered nose and elliptical stern-I without wing at submergence depth ratios, *h/D* of 0.75, 1.0, 1.5, 2.0, 3.0.

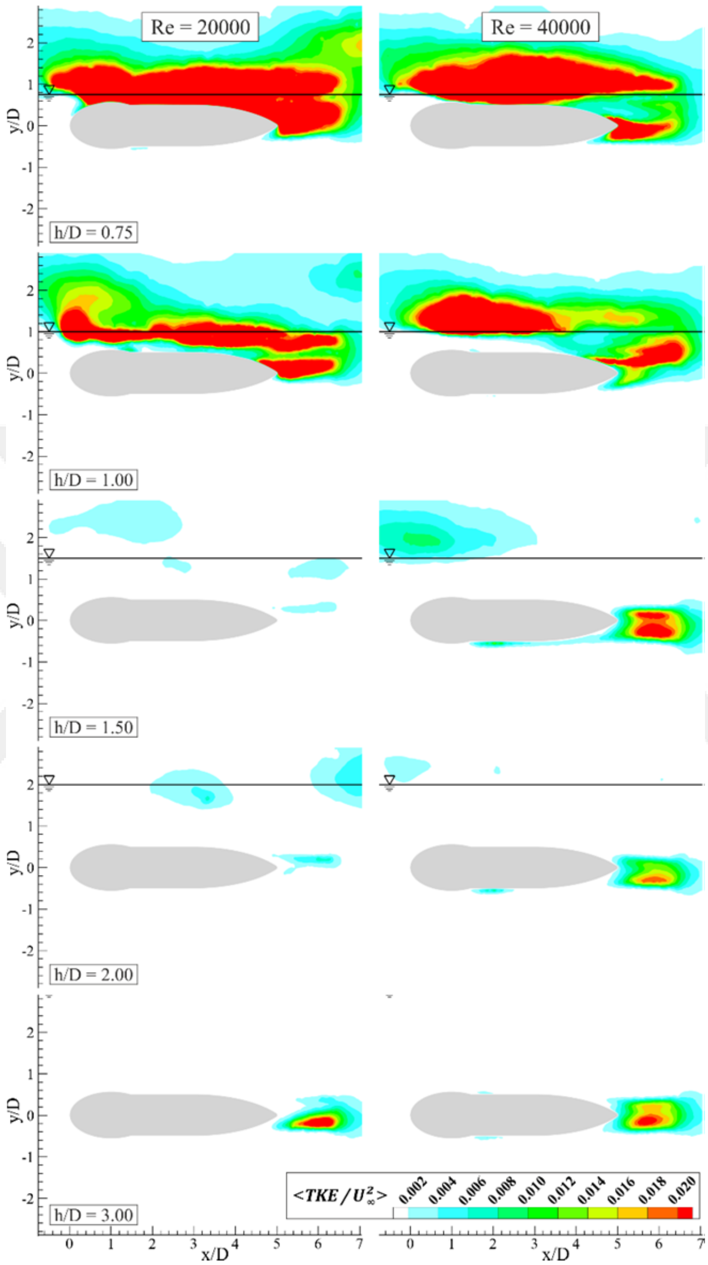

Figure 4.6. Distributions of the dimensionless turbulent kinetic energy $<TKE/U_{\infty}^{2}>$ contours calculated numerically for the torpedo-like geometry of cambered nose and elliptical stern-I without wing at submergence depth ratios, *h/D* of 0.75, 1.0, 1.5, 2.0, 3.0.

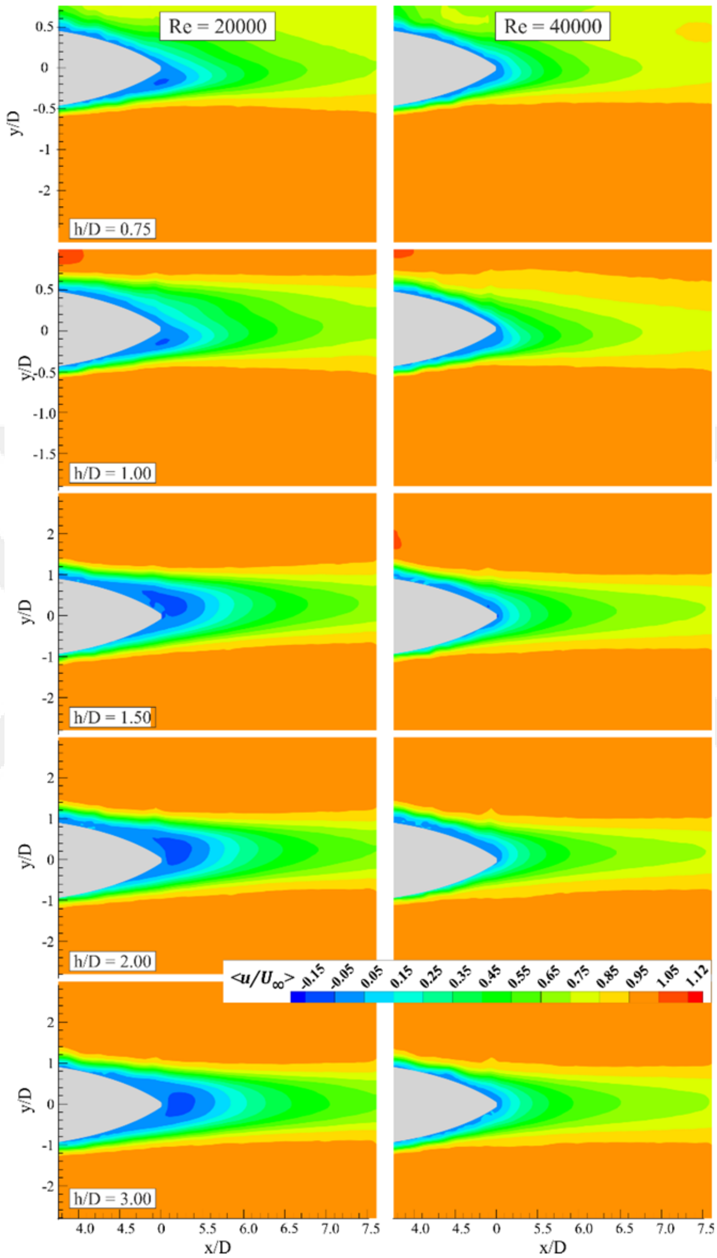

Figure 4.7. Contours of the time-averaged dimensionless streamwise velocity component $<u/U_{\infty}>$ calculated from the PIV measurements downstream of the torpedo-like geometry of cambered nose and elliptical stern-I without wing at submergence depth ratios, *h/D* of 0.75, 1.0, 1.5, 2.0, 3.0

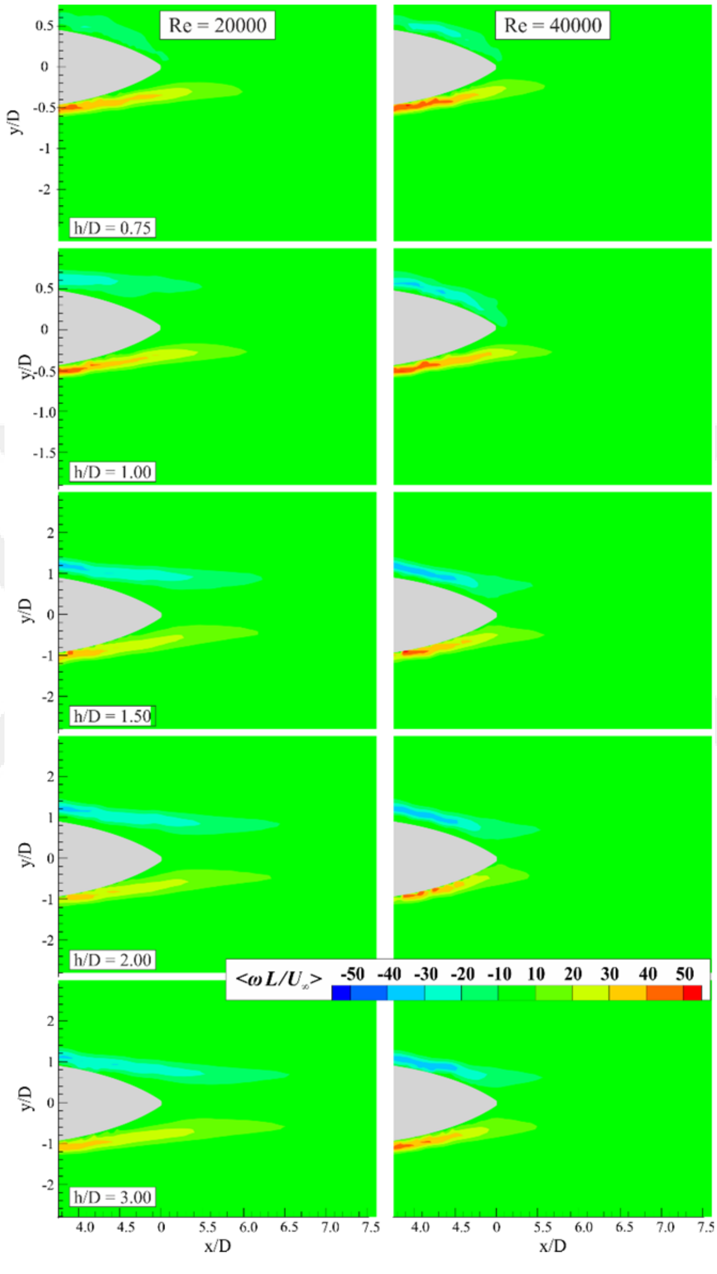

Figure 4.8. Variation of the time-averaged dimensionless vorticity contours $<\omega \, L/U_{\infty}>$ calculated from the PIV measurements downstream of the torpedo-like geometry of cambered nose and elliptical stern-I without wing at submergence depth ratios, *h/D* of 0.75, 1.0, 1.5, 2.0, 3.0.

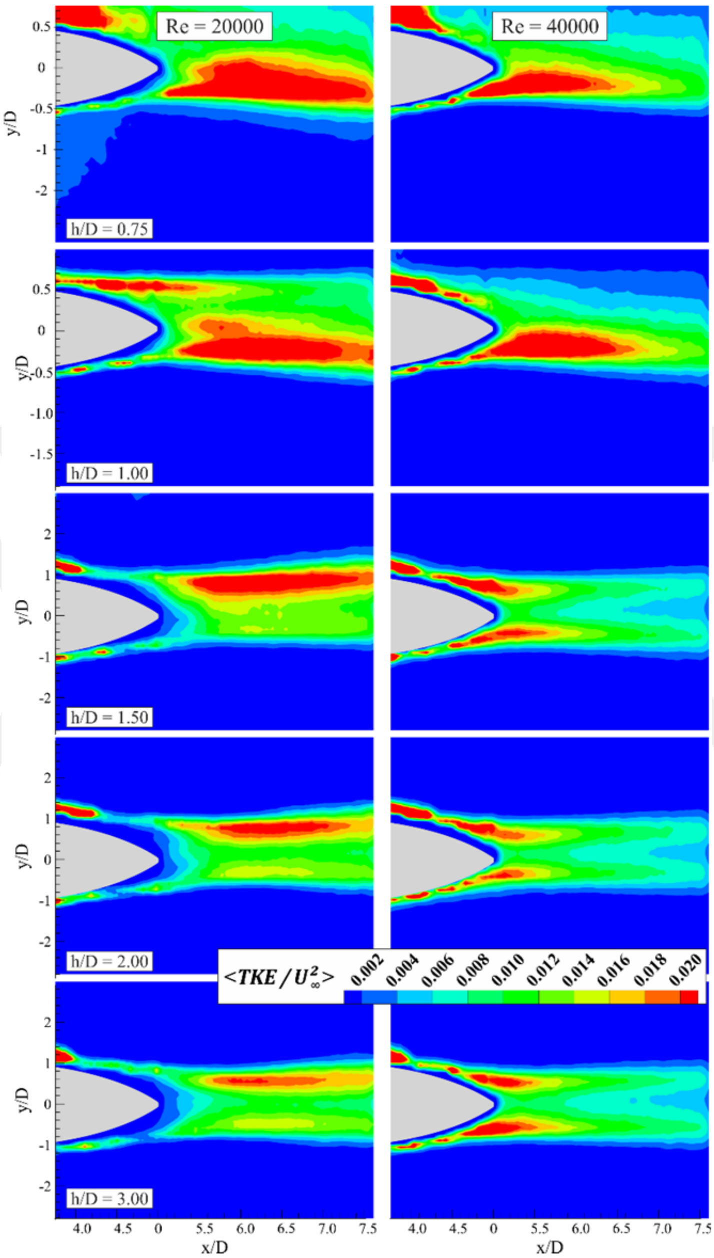

Figure 4.9. Distributions of the turbulent kinetic energy $<TKE/U_\infty^2>$ calculated from the PIV measurements downstream of the torpedo-like geometry of cambered nose and elliptical stern-I without wing at submergence depth ratios, *h/D* of 0.75, 1.0, 1.5, 2.0, 3.0.

4.1.2. The Effect of Angle of Attack on the Flow Structures

The time-averaged dimensionless contours of streamwise velocity component $< u/U_\infty >$, crosswise velocity component $< v/U_\infty >$, turbulent kinetic energy $< TKE/U_\infty^2 >$, and vorticity $< \omega\, L/U_\infty >$ for the cambered nose with elliptical stern-I geometry without wing at submergence depth ratios of *h/D* = 0.75, 1.00, 1.50, 2.00 and 3.00, and for angles of attack of α = 0°, 4°, 8° and 12° at Re=$40\text{x}10^3$are given in Figures 014 – 020. In all of these flow patterns, the free-surface is strongly effective for submergence depth ratios of 0.75 and 1.00, and for angles of attack α = 0°, 4°, 8°, and 12°, where its effect is demonstrated by the jet-like flow and the mixing of air with water in the region in-between the free-surface and upper boundary of the torpedo-like geometry.

In Figure 4.10 a strong recirculating region is observed along the mid-section part of the geometry for α = 4° and *h/D* = 0.75, which is explained by the strong interaction between the free-surface and the geometry. The figure also shows that for *h/D* = 1.00 the flow separates from the nose of the geometry and reattached to its boundary at some distance ahead. The reattachment of the flow to the boundary of the model results in a smaller flow recirculation region when compared to the case of *h/D* = 0.75. However, when the submergence depth ratio, *h/D* had increased the reattachment of the flow to the upper part of the model geometry occurred after a longer distance owing to the disappearing of the effect of the jet-like flow with depth. Also, it can be seen from Figure 015 that at higher angles of attack the flow field becomes more complex for the submergence depth ratios, *h/D* of 0.75 and 1.00 due to the interaction of the free-surface of the upper part of the model geometry. It should be noted that the cambered nose of the geometry promotes the separated flow to reattach to the boundary earlier than it would be with other nose profiles.

For higher submergence depth ratios, *h/D* the free-surface effect reduces as the jet-like flow effect is reduced and at *h/D* ≥ 3 the wake region regains its symmetry for the α = 0°. It is also observed that when the angle of attack is increased from 0° to 12° negative velocity magnitudes disappear downstream of the model geometry, but the flow separation on the upper part of the geometry becomes larger and more dominant than the lower part, thus a wider wake region. Furthermore, while the variation of time-averaged velocity components, $< u/U_\infty >$ and $< v/U_\infty >$ at α = 0° in the wake region is symmetrical with respect to the centerline of the model geometry, the variation becomes more complicated and asymmetric, and the wake regions become larger at α = 4°, 8°, and 12°.

The contours of the crosswise velocity component in Figures 016 and 017 show higher negative values under the influence of the free-surface. The change in the direction of the crosswise velocity component from positive to negative values creates a fluctuating load on the body as the fluid flows from the nose to the stern of the model geometry. Also, the negative values of the crosswise velocity patterns for α = 8° and 12°, and for *h/D* = 0.75 and 1.00 occupy the whole flow field around the body while the positives values exist in the far wake region. This occurs due to the reliving effect and the three-dimensional nature of the flow. Cross comparison of the angle of attack effects (α = 4°, 8°, and 12°) on the flow structures for *h/D* = 3.0 shows asymmetrical flow patterns except for α = 0°.

The dimensionless turbulent kinetic energy $<TKE/u_\infty^2>$ contours presented in Figures 018 and 019 show the fluctuations level in the flow field. For submergence depth ratio of 0.75 and 1.0, the turbulent kinetic energy, $<TKE/u_\infty^2>$ contours have higher values around the free-surface which might be due to the formation of the aforementioned jet-like flow and no-slip condition at the air-water interface. Since the effect of the jet-like flow decreases away from the free-surface, the $<TKE/u_\infty^2>$ values are damped out and finally disappear beyond the submergence depth ratios of *h/D* ≥ 1.5. The fluctuation levels of flow structure around the nose and mid-section of the torpedo-like geometry for the α = 0° are so small that the strength of the turbulent kinetic energy diminishes at *h/D* = 2.0 and 3.0. In general, the interactions between core and wake flow regions around the boundary of the stern section of the model geometry results in a higher rate of turbulent kinetic energy along the outer boundary of wake regions.

Under the effect of the angles of attacks of α = 4°, 8° and 12°, the turbulent kinetic energy, $<TKE/u_\infty^2>$ values are higher in the upper region of the model geometry. This means that the model geometry has larger fluctuations magnitude in that region. For the submergence depth ratios, *h/D* of 1.0, 1.5 and 2.0, the turbulent kinetic energy,$<TKE/U_\infty^2>$ contours enhanced considerably around the reattachment points on the upper surface around the mid-section of the torpedo-like geometry.

The time-averaged dimensionless vorticity contours $<\omega\, L/u_\infty>$ obtained for the cambered nose and elliptical stern-I geometry without wing at submergence depth ratios, *h/D* of 0.75, 1.00, 1.50, 2.00 and 3.00, and for angles of attack of 0°, 4°, 8°, and 12° are shown in Figures 020 and 021. Rotational flow occurs in the region between the free-surface and the upper part of the model geometry and over the free surface for *h/D* = 0.75 and 1.0. As the angles of attack increase, the separated flow from the nose section induces the acceleration of the velocity which increases the velocity gradients in both streamwise and crosswise direction. This physical phenomenon accumulates the vorticity strength around the nose and free surface. Magnitudes of the vorticity concentrations are higher on the upper side of the torpedo-like geometry than the lower side due to the free-surface effects. For the angle of attack value of α = 0°, vorticity concentrations elongate down-to-the wake region. On the other hand, when the angle of attack is increased from α = 4° to 12°, the vorticity concentration warps the model geometry. The magnitude of vorticity concentrations around the centerline of the wake region for the submergence depth ratios, *h/D* ≥ 2 are very close to zero due to the lower velocity gradient and the elimination of the negative and positive small eddies each other.

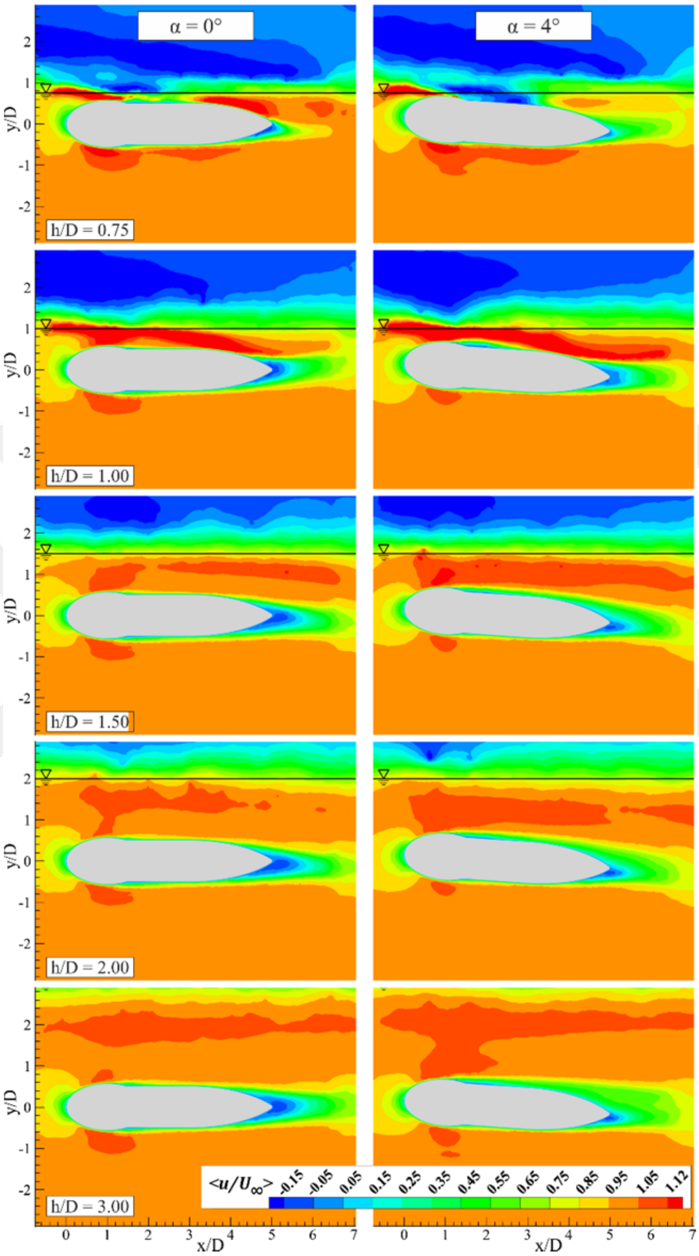

Figure 4.10. Contours of the time-averaged dimensionless streamwise velocity component $<u/U_{\infty}>$ calculated numerically for the torpedo-like geometry of cambered nose and elliptical stern-I without wing at submergence depth ratios, *h/D* of 0.75, 1.0, 1.5, 2.0, 3.0 and for the angle of attack of 0° and 4°

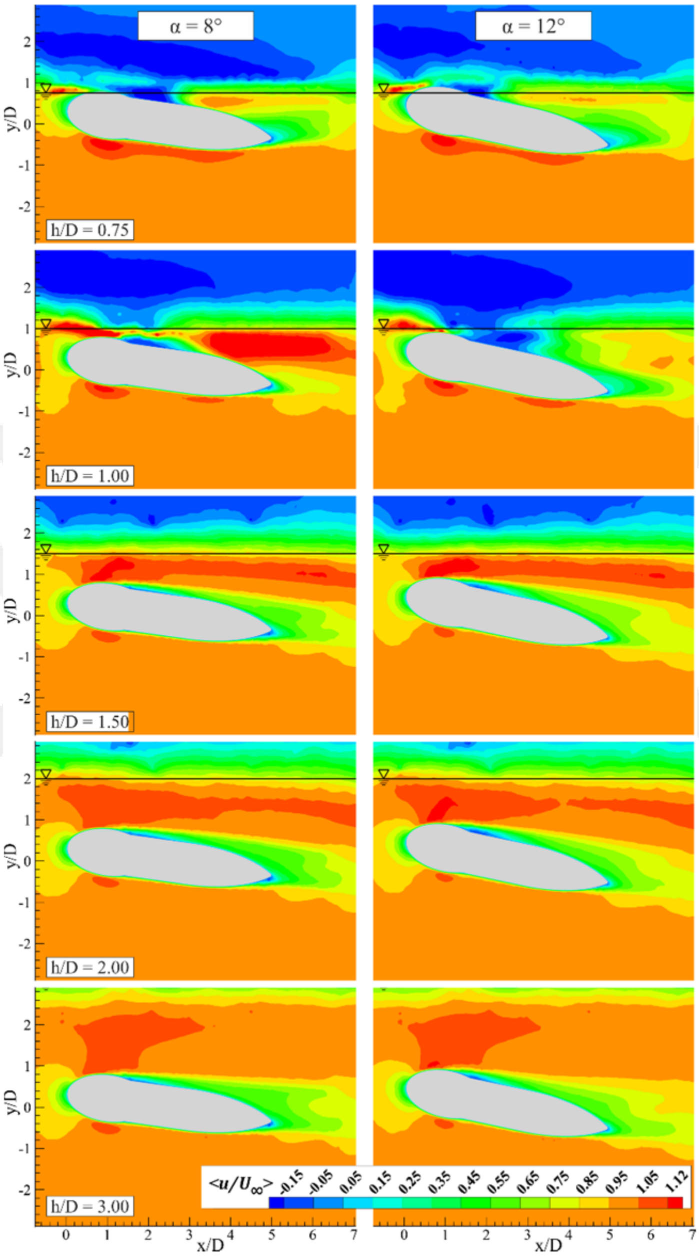

Figure 4.11. Continuation of figure 014 for the angles of attack of 8°, and 12°

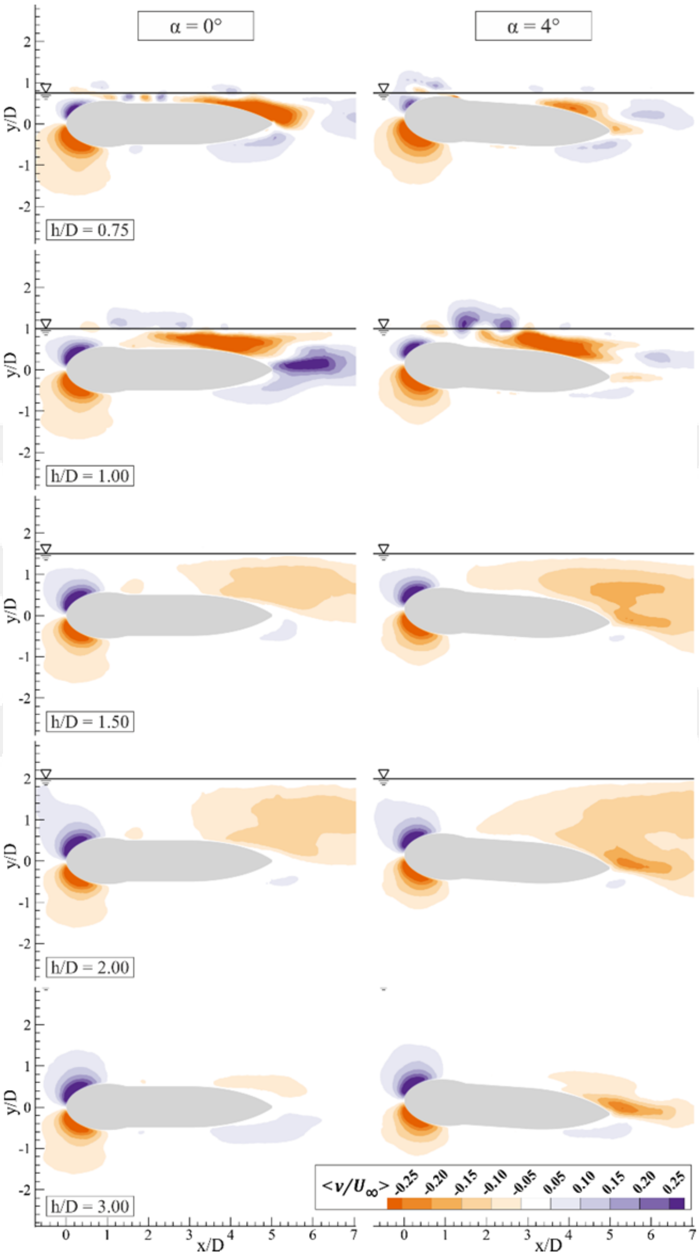

Figure 4.12. Contours of the time-averaged dimensionless crosswise velocity component $<v/U_{\infty}>$ calculated numerically for the torpedo-like geometry of cambered nose and elliptical stern-I without wing at submergence depth ratios, *h/D* of 0.75, 1.0, 1.5, 2.0 3.00 and for the angles of attack of 0° and 4°

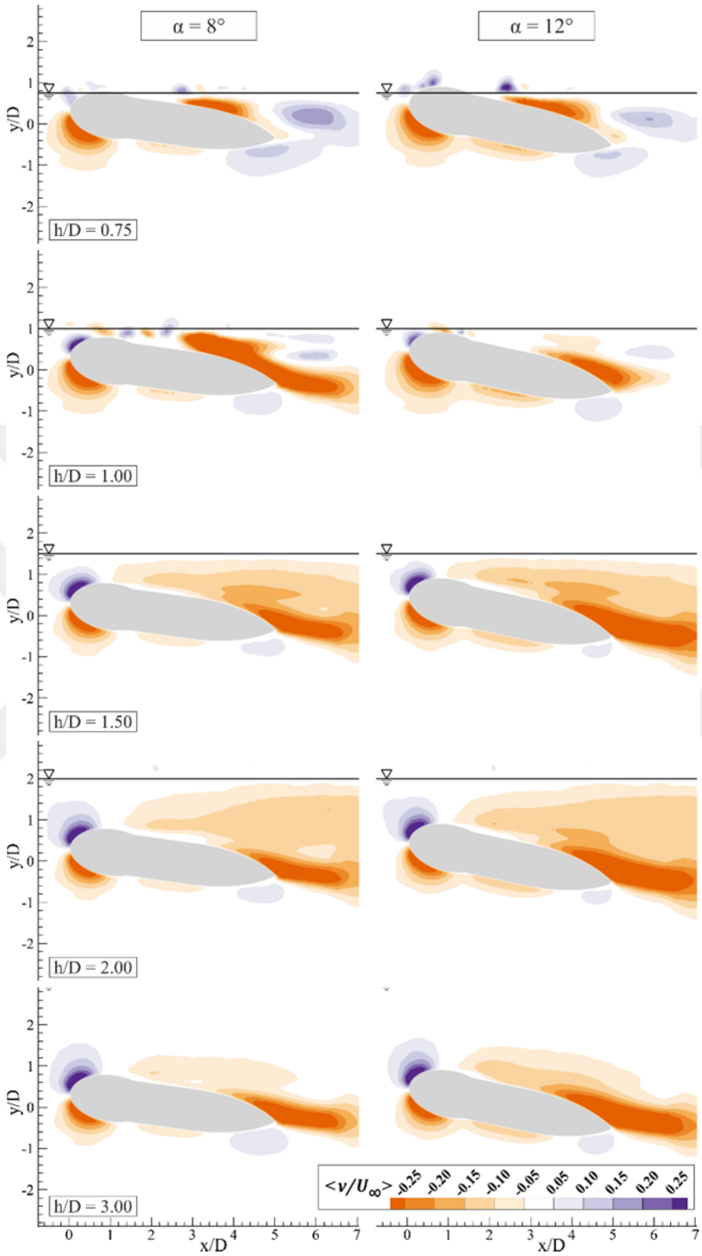

Figure 4.13. Continuation of figure 016 for the angle of attack of 8° and 12°.

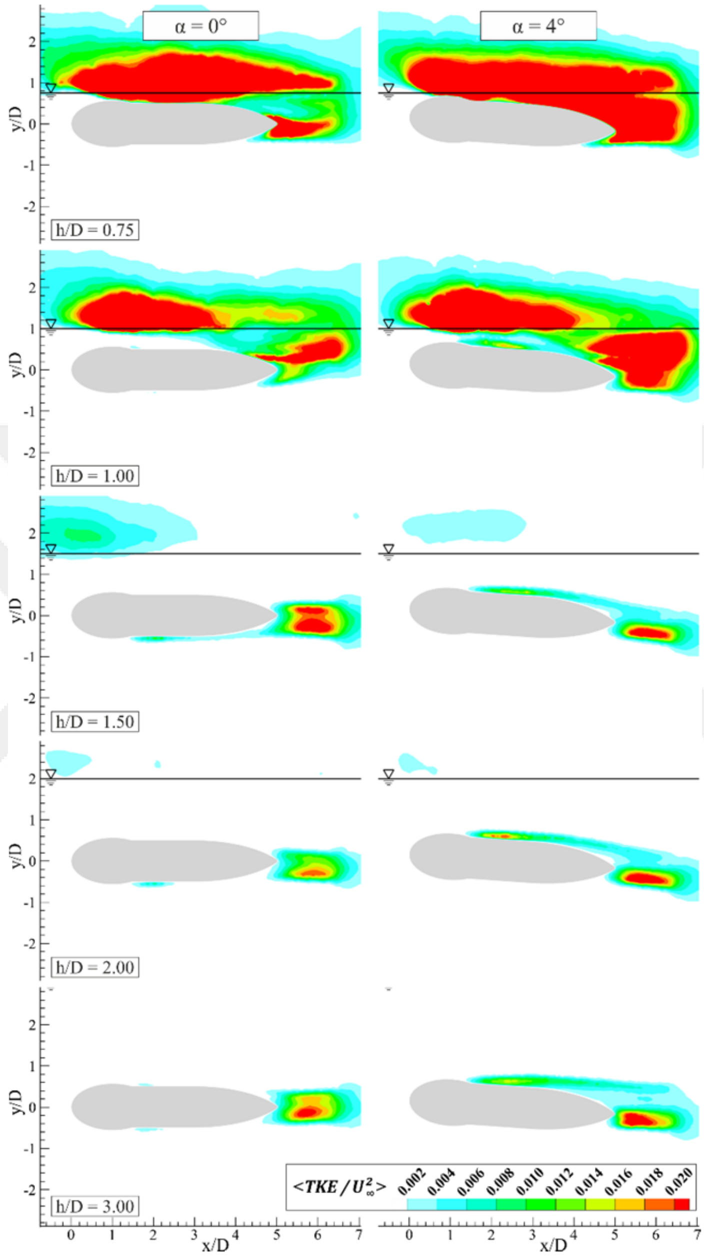

Figure 4.14. Distributions of the turbulent kinetic energy $<TKE/U_{\infty}^{2}>$ contours calculated numerically for the torpedo-like geometry of cambered nose and elliptical stern-I without wing at submergence depth ratios, *h/D* of 0.75, 1.0, 1.5, 2.0, 3.0 and for the angles of attack of 0° and 4°

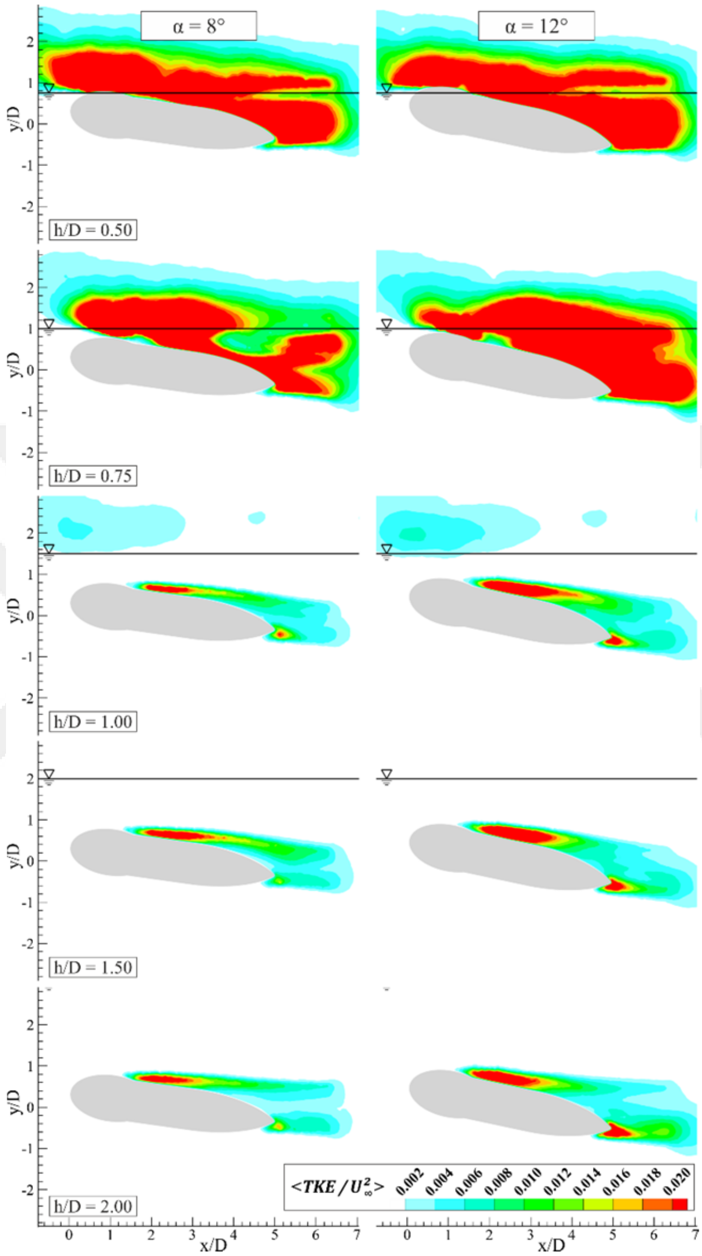

Figure 4.15. Continuation of figure 018 for the angles of attack of 8° and 12°.

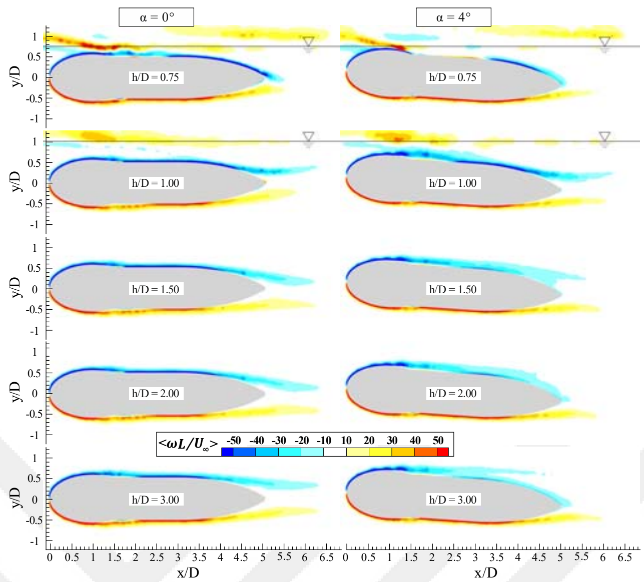

Figure 4.16. Variation of the time-averaged dimensionless vorticity $<\omega \cdot L/U_{\infty}>$ contours calculated numerically for the torpedo-like geometry of cambered nose and elliptical stern-I without wing at submergence depth ratios, *h/D* of 0.75, 1.0, 1.5, 2.0, 3.0 and for the angles of attack of 0°, 4°, 8°, 12°.

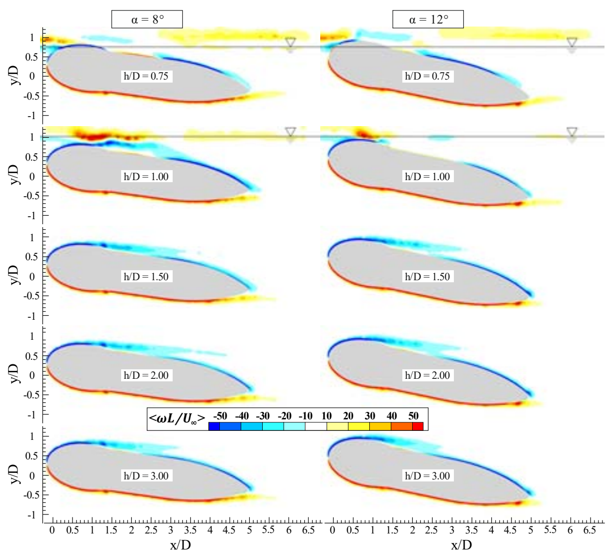

Figure 4.17. Continuation of figure 020 for the angles of attack of 8° and 12°.

4.2. Comparison of Flow Characteristics of the Torpedo-Like Geometry Having Elliptical Stern-I and Stern-II.

Comparison of the time-averaged dimensionless streamwise velocity distributions $<u/U_\infty>$, cross-stream velocity distributions $<v/U_\infty>$, vorticity contours $<\omega L/U_\infty>$ and patterns of $<TKE/U_\infty^2>$ were calculated numerically for the cambered nose and wingless elliptical stern-I geometry (left column) and wingless elliptical stern-II geometry (right column) at submergence depths of *h/D* =0.50, 0.75, 1.00, 1.5, 2.0, 2.5, 3.0, and 3.5 and for the angle of attack of α = 0° at Re = 40x10^3 are given in Figures 022 – 028. The interpretation of the results given in Figures 14 – 21 for α = 0° at Re = 40x10^3 is the same as in the left column of the images shown in Figures 022 – 028. The torpedo-like geometry having a cambered nose and wingless elliptical stern-I (left column) has a slightly smaller wake region and vortex formation length that is very similar to the elliptical stern-II model geometry (right column). In general, the numerical results obtained from the simulations performed for the two model geometries (elliptical stern-I and stern-II) suggest that at the macrostructure level there is no considerable variation in the flow characteristics between the two models of the torpedo-like geometries. It should be mentioned that for each parameter set the ANSYS-Fluent case setup was exactly the same for both models (stern-I and stern-II).

Figure 4.25 shows a comparison of the time-averaged dimensionless streamwise velocity contours $<u/U_\infty>$, crosswise velocity contours, $<v/U_\infty>$ calculated from PIV measurement for the torpedo-like geometries having the profiles of stern-I (left column) and stern-II (right column) without wing at submergence depths of *h/D* = 0.50, 0.75, 1.00 and 1.5 for the angle of attack of α = 0° and at Re = 20x10^3. When the geometry is located near the free-surface as in the cases of *h/D* = 0.5, 0.75 and 1.0, the velocity contours for both $<u/U_\infty>$ and $<v/U_\infty>$ have asymmetrical velocity distributions due to the hydrodynamic pressure effects and wavy form of the free-surface. As the submergence depth ratio, *h/D* increases, the contours of the velocity become close to the symmetry with respect to the axis passing along the centerline of the model geometry. Under the free-surface effect, the contours of the crosswise velocity component, $< v/U_\infty >$ on the upper side of the wake exist which is less than the velocity components, $< v/U_\infty >$ on the lower side. Vortex formation length of the model geometry with the wingless elliptical stern-I profile (left column) is slightly longer than the wingless elliptical stern-II profile.

Comparison of the time-averaged dimensionless vorticity contours $< \omega\, L/U_\infty >$ calculated from the PIV measurements for the torpedo-like geometry of cambered nose and wingless elliptical stern-I (left column), and wingless elliptical stern-II (right column) at submergence depth ratios of *h/D* = 0.75, 1.0, 1.5, 2.0, 2.5, 3.0 and 3.5 for the angle of attack of $\alpha = 0°$ at Re=20x10^3 (See first and third columns) and Re=40x10^3 (See second and fourth columns) is presented in Figure 4.26. The concentrations of the vorticity for Re=40x10^3 cover less area of wake region than the case of Re=20x10^3. Vertical wake size of the vorticity structure is larger for the wingless elliptical stern-II model geometry (right two columns) than the elliptical stern-I model geometry (See left two columns) for both Reynolds numbers. The vorticity concentrations in the clockwise direction develop over the upper surface of the geometry have a smaller magnitude with respect to the lower one due to the free-surface effect. It can be seen from all obtained images (numerically and experimentally) that the vorticity contours have higher strength in the boundary layer region around the model geometry and in the upper side region of the model geometry due to the velocity gradient.

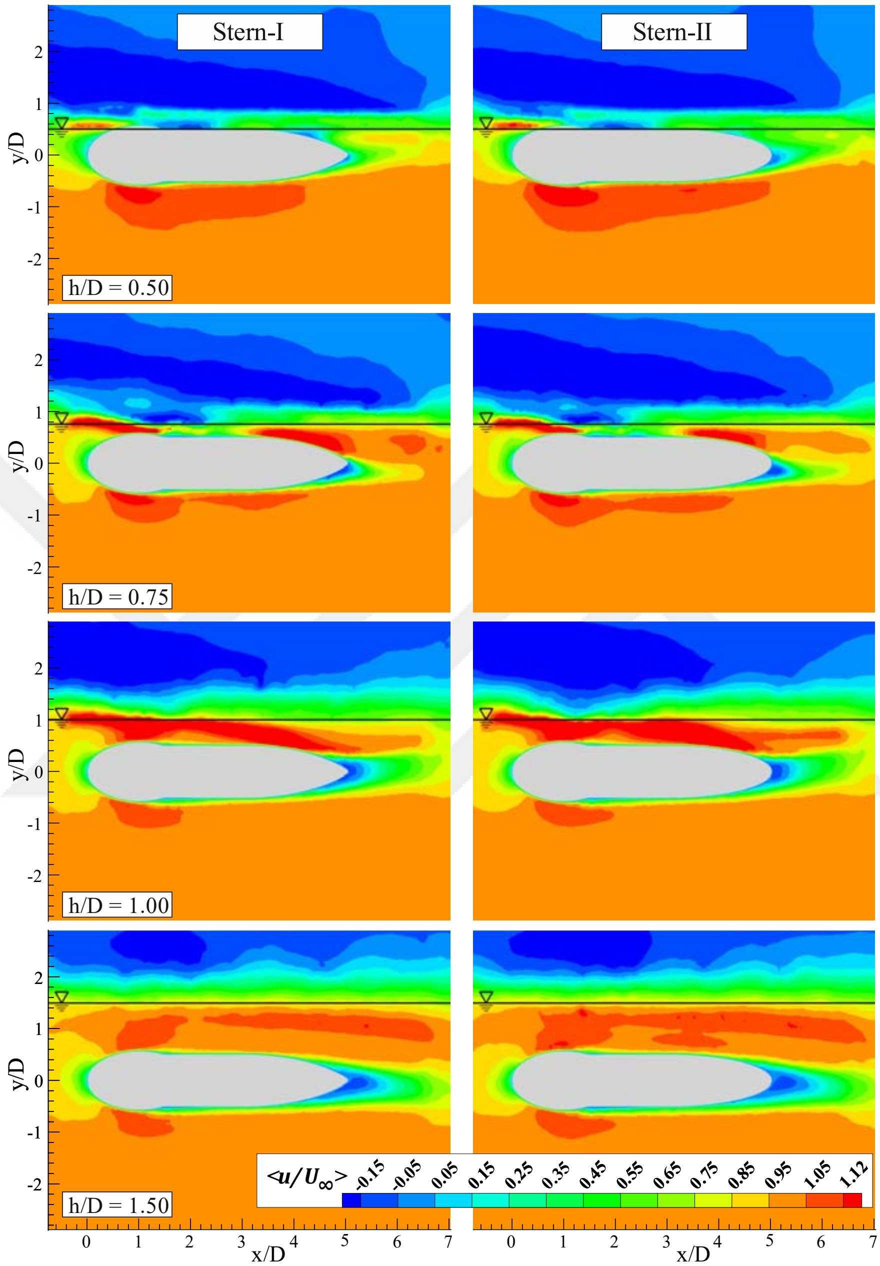

Figure 4.18. Contours of the time-averaged dimensionless streamwise velocity component $<u/U_\infty>$ calculated numerically for the torpedo-like geometry of elliptical stern-I and stern-II without wing at submergence depth ratios, *h/D* of 0.5, 0.75, 1.0 and 1.5 and for Re = 40x10^3 and α = 0°

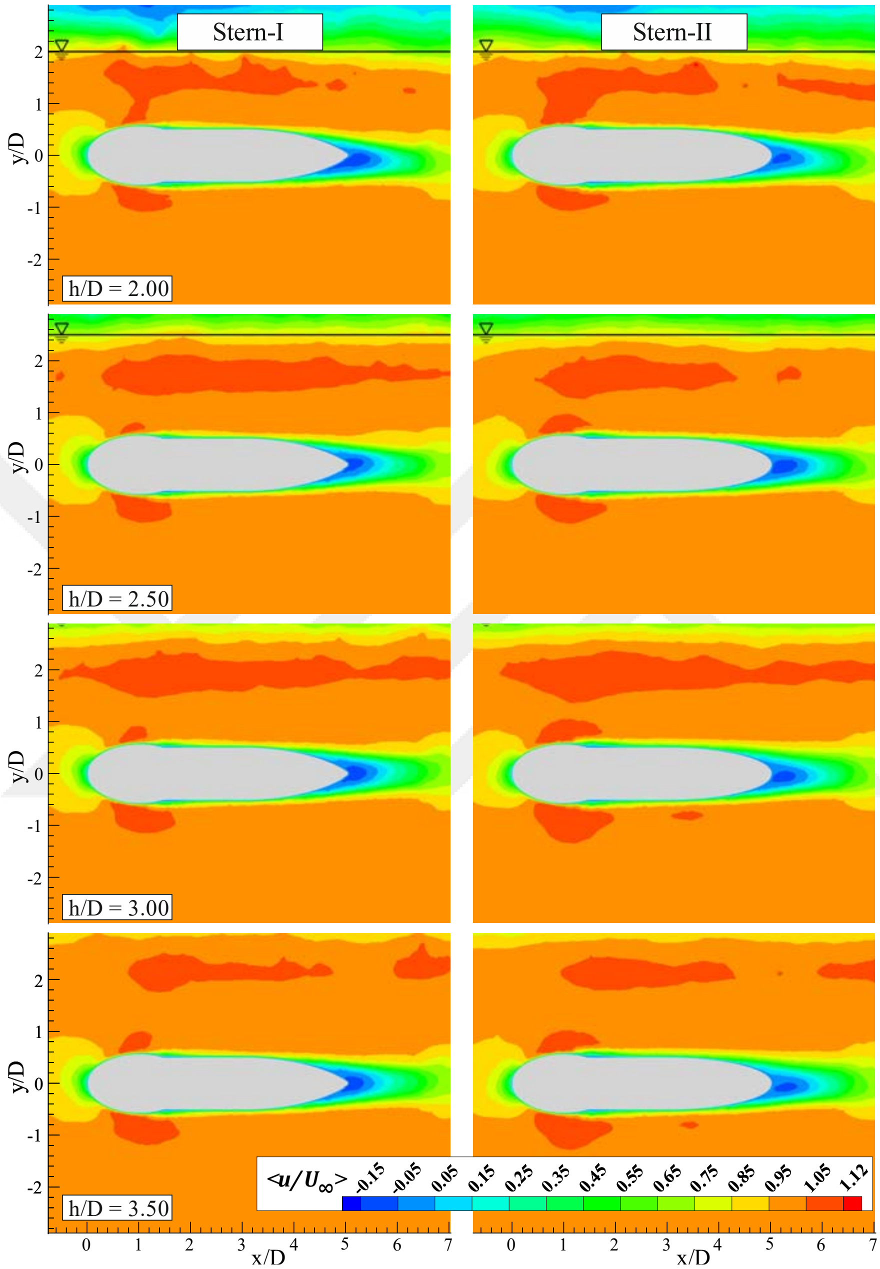

Figure 4.19. Continuation of Figure 4.18 for submergence depth ratios, *h/D* of 2.0, 2.5, 3.0, and 3.5

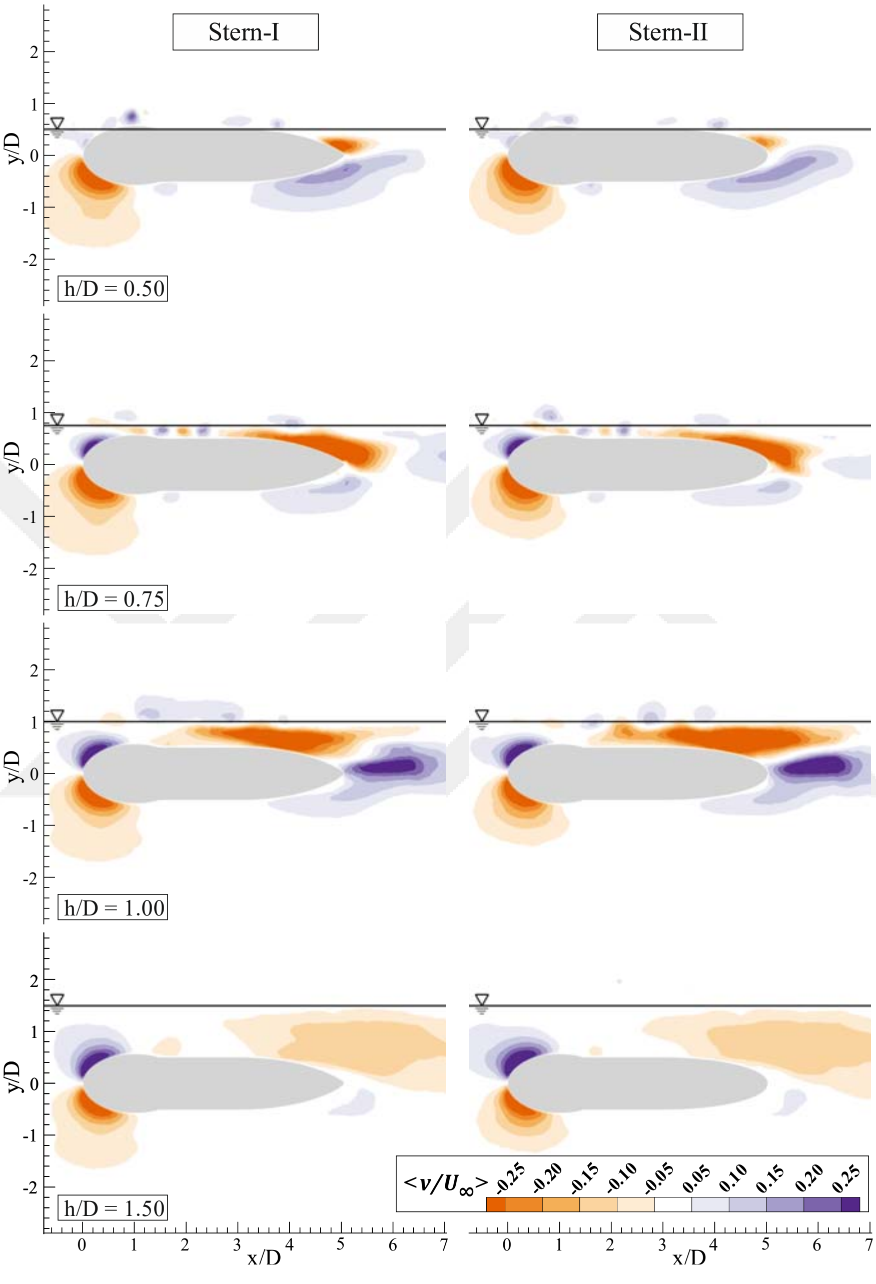

Figure 4.20. Contours of the time-averaged dimensionless streamwise velocity component $<v/U_\infty>$ calculated numerically for the torpedo-like geometry of elliptical stern-I and stern-II without wing at submergence depth ratios, *h/D* of 0.5, 0.75, 1.0 and 1.5 and for Re = 40x10^3 and α = 0°

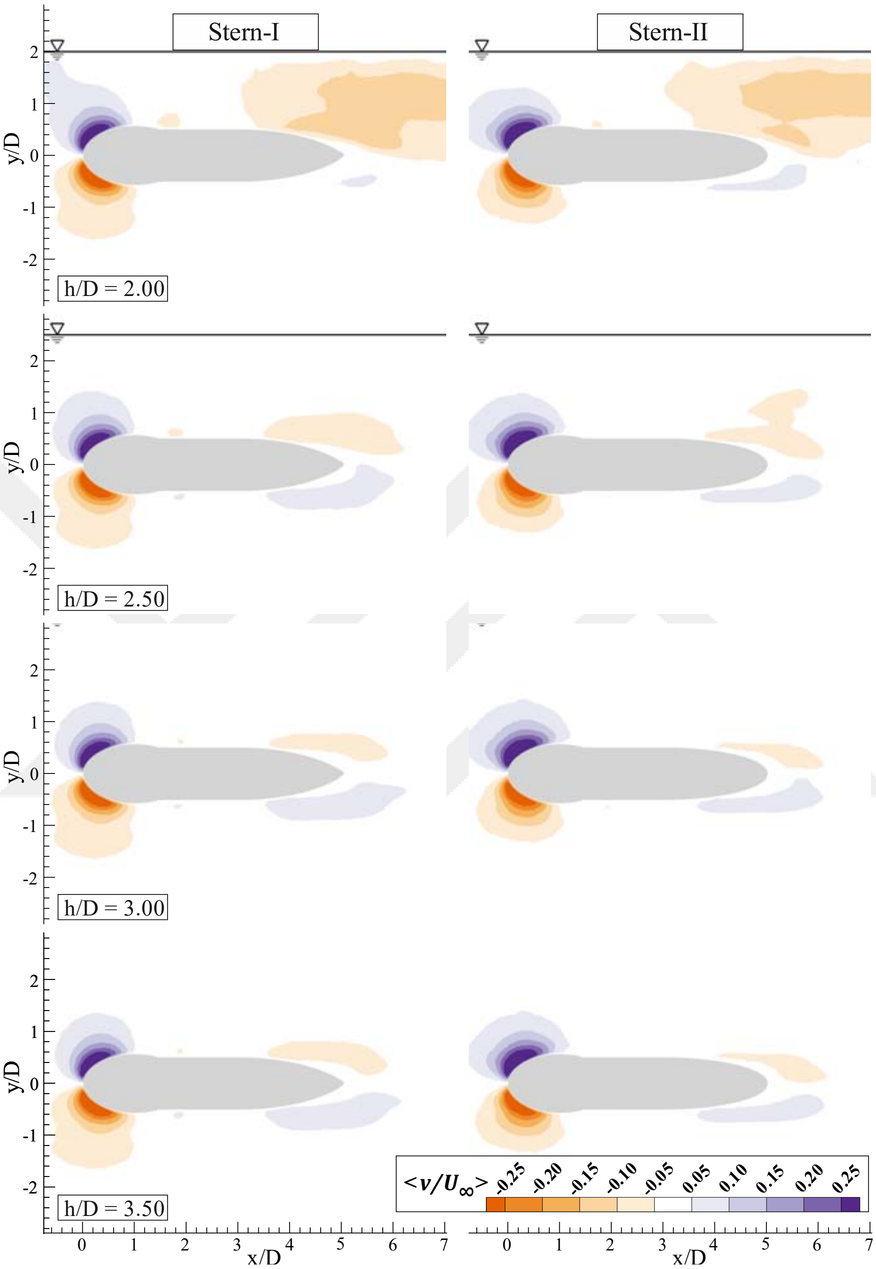

Figure 4.21. Continuation of Figure 4.20 for submergence depth ratios, *h/D* of 2.0, 2.5, 3.0, and 3.5

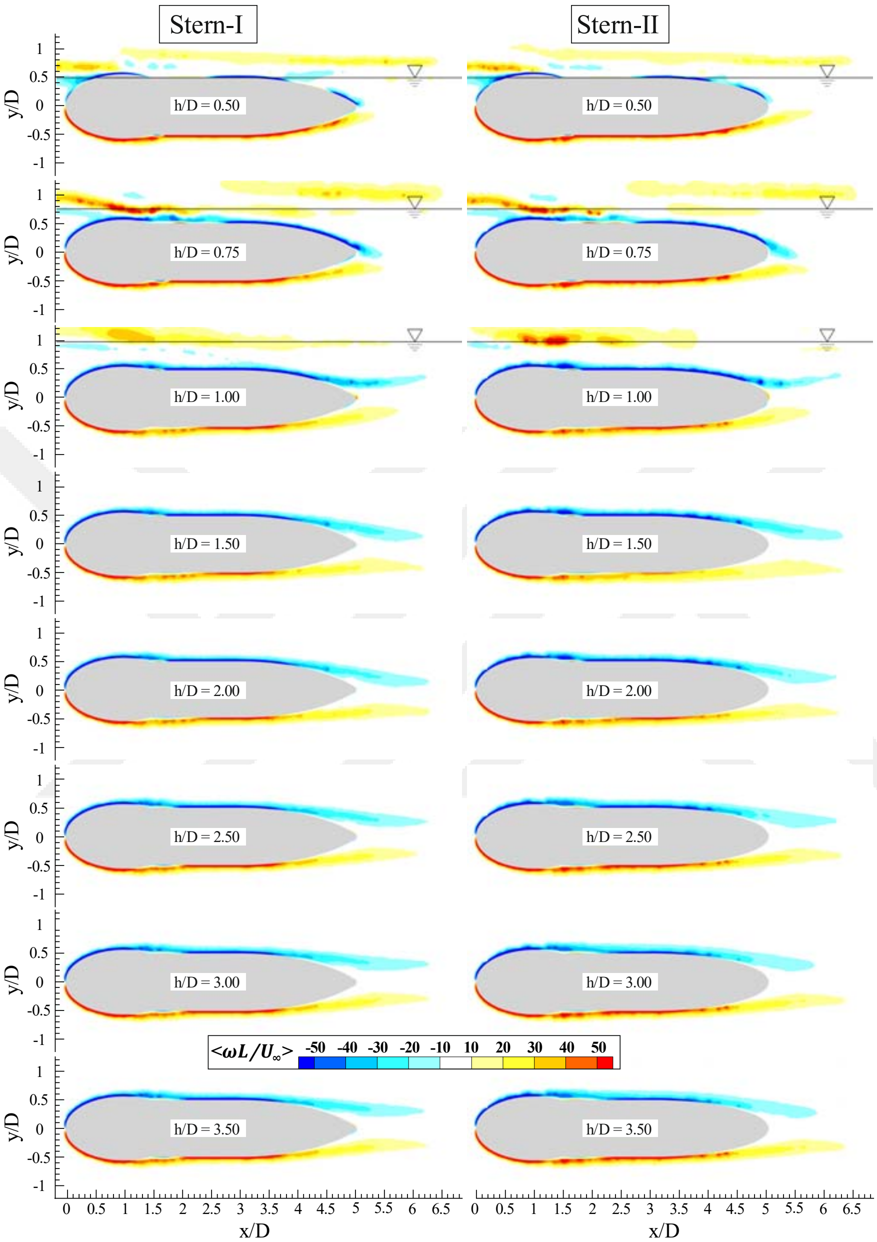

Figure 4.22. Contours of the time-averaged dimensionless vorticity $<\omega L/U_\infty>$ calculated numerically for the torpedo-like geometry of elliptical stern-I and stern-II without wing at submergence depth ratios, *h/D* of 0.5, 0.75, 1.0, 1.5, 2.0, 3.0 and 3.5 for Re = $40\text{x}10^3$ and α = 0°

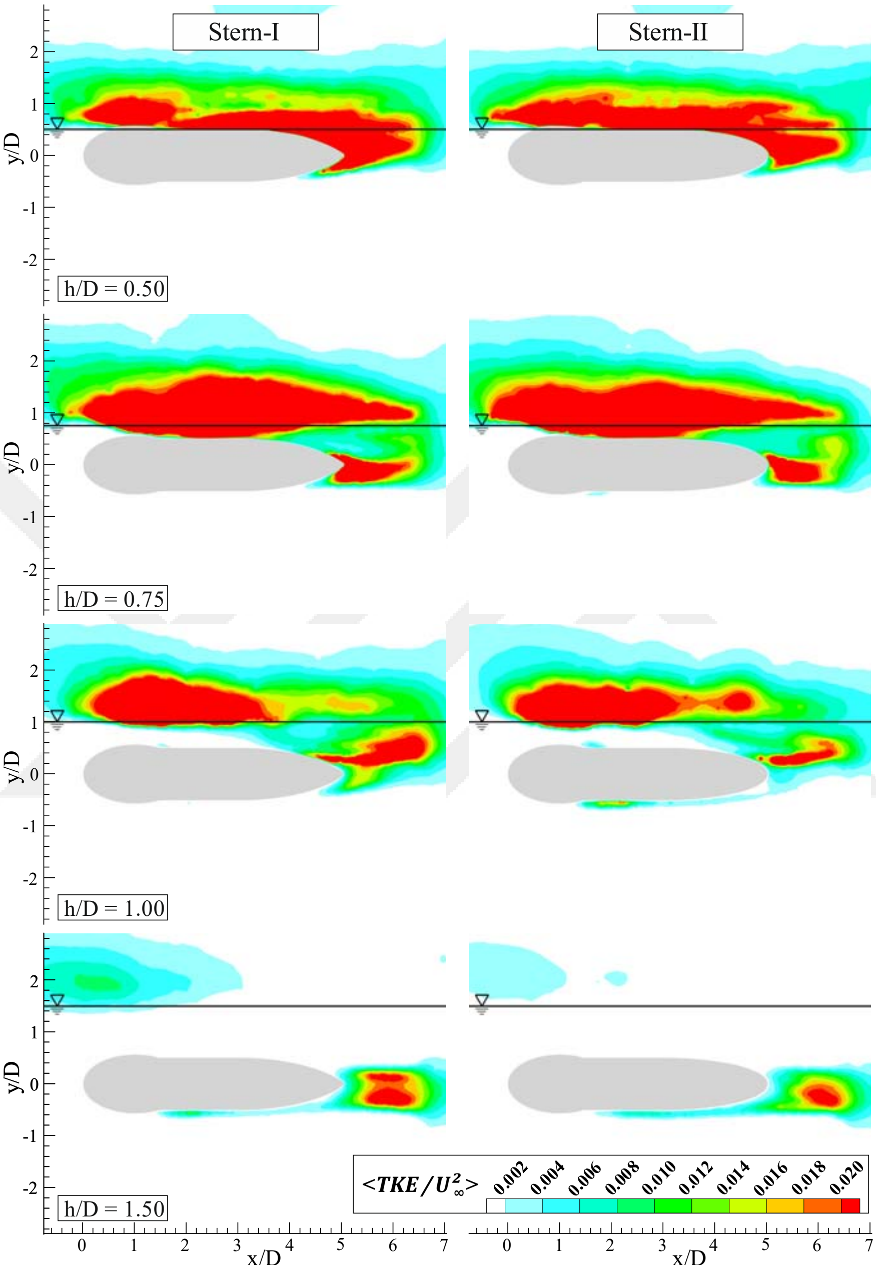

Figure 4.23. Distribution of the time-averaged turbulent kinetic energy $<TKE/U_\infty^2>$ calculated numerically for the torpedo-like geometry of elliptical stern-I and stern-II without wing at submergence depth ratios, *h/D* of 0.5, 0.75, 1.0 and 1.5 and for Re = $40x10^3$ and α = 0°

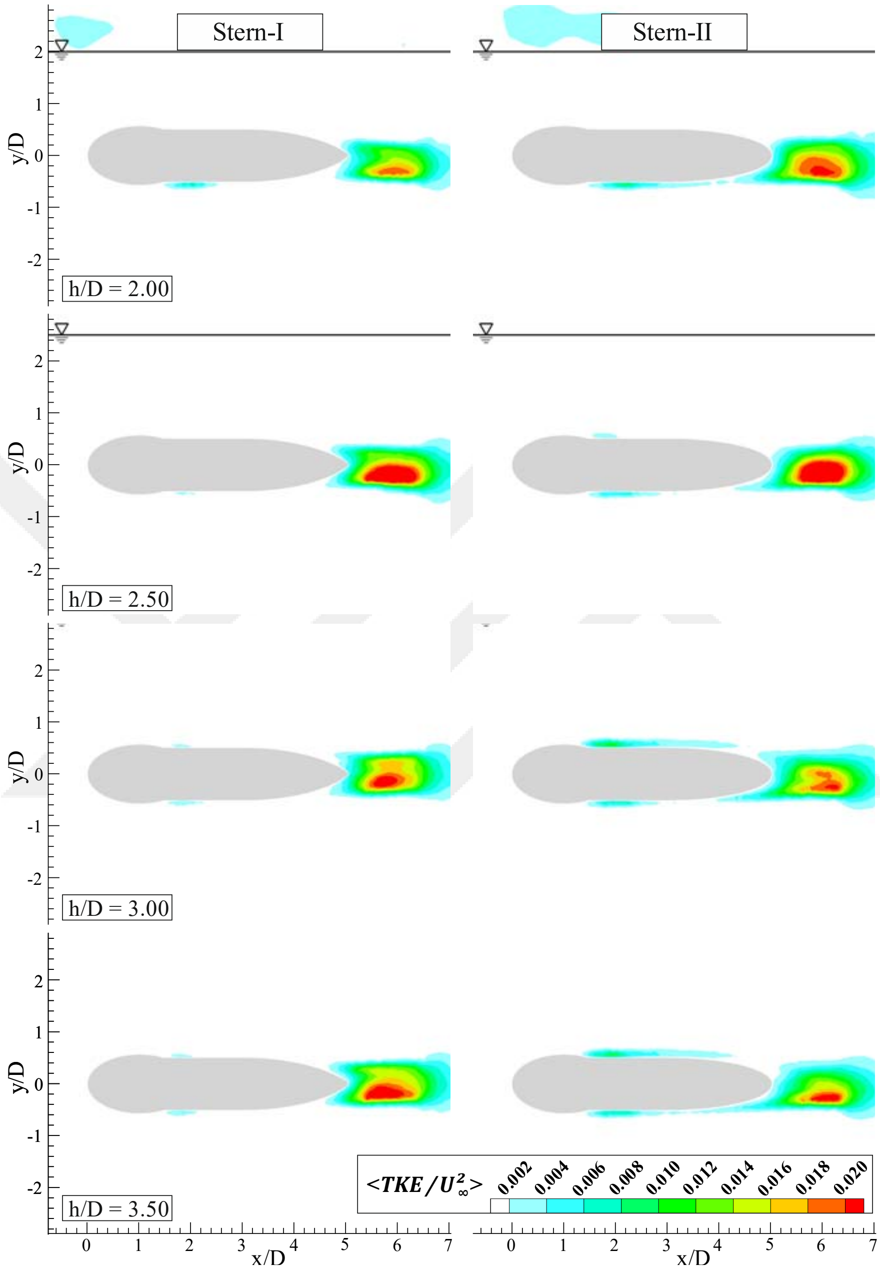

Figure 4.24. Continuation of Figure 4.23 for submergence depth ratios, *h/D* of 2.0, 2.5, 3.0, and 3.5

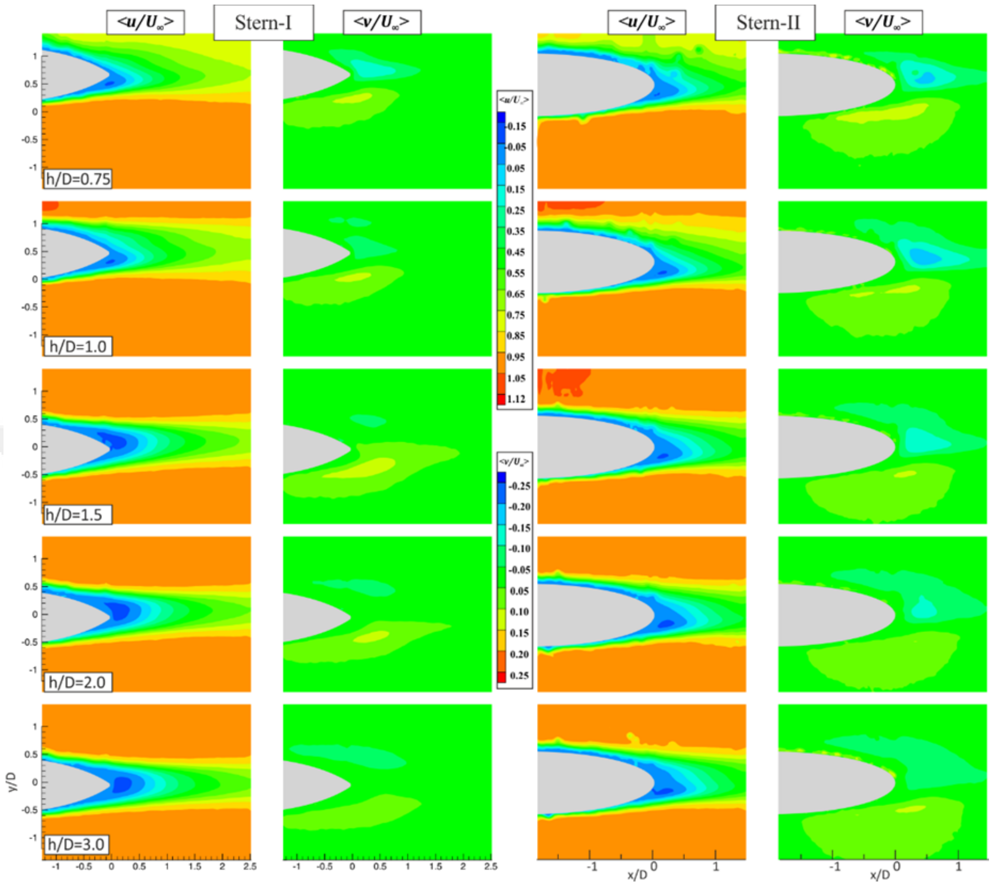

Figure 4.25. Contours of the time-averaged dimensionless streamwise $<u/U_\infty>$ and crosswise $<v/U_\infty>$ velocity components calculated from the PIV measurements for the torpedo-like geometry of elliptical stern-I and stern-II without wing at submergence depth ratios, *h/D* of 0.75, 1.0, 1.5, 2.0 and 3.0 for Re = $20x10^3$ and α = 0°

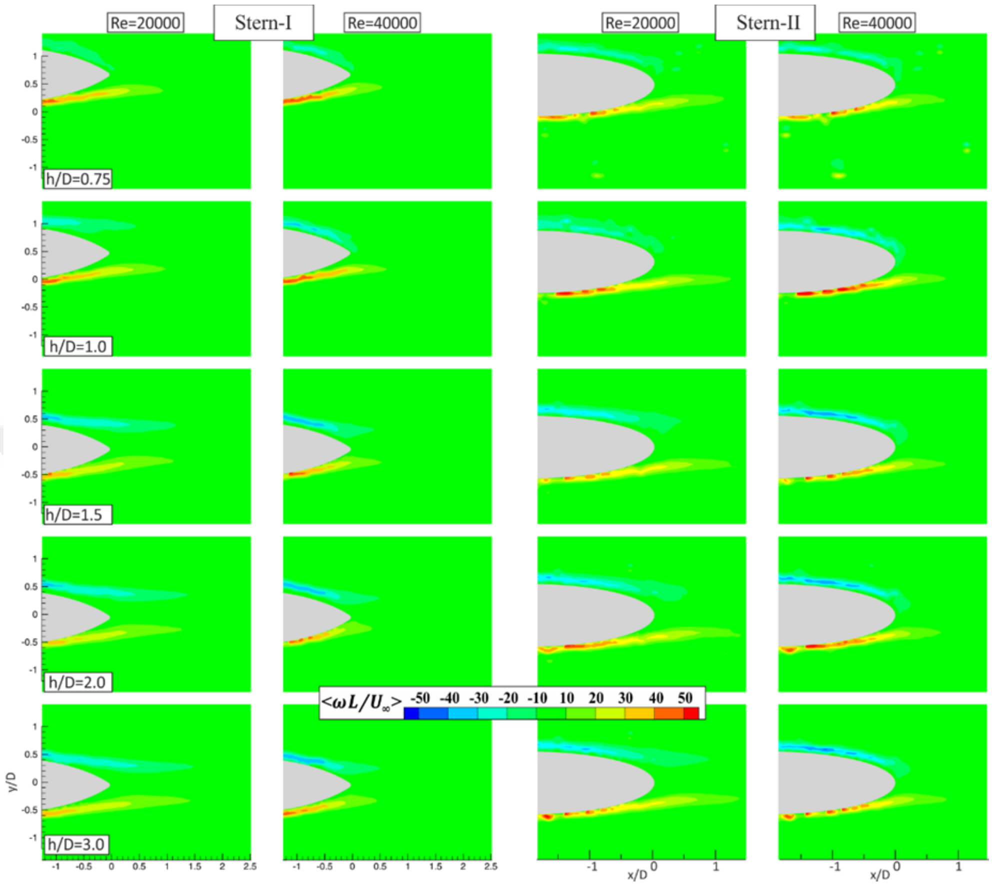

Figure 4.26. Contours of the time-averaged dimensionless vorticity $<\omega L/U_\infty>$ calculated from the PIV measurement for the torpedo-like geometry of elliptical stern-I and stern-II without wing at submergence depth ratios, *h/D* of 0.75, 1.0, 1.5, 2.0 and 3.0 for Re = 40x10^3 and Re = 20x10^3, and α = 0°

4.2.1. Streamlines

The time-averaged streamline topology calculated numerically for the cambered nose and wingless elliptical stern-I geometry (left column) and wingless elliptical stern-II model geometry (see right column) without wing at submergence depth ratios of *h/D* = 0.50, 0.75, 1.00, 1.5, 2.0, 2.5, 3.0 and 3.5 for angle of attack of α = 0° and Re=40x10^3 are given in Figures 031 and 032. At the submergence depth ratio of *h/D* = 0.5 for both appendages, the time-averaged streamlines, <Ψ>

in touching the free-surface case of the model geometry as seen in the first column and row of figure 031 have similar trends where nodal occurs due to the surface deformation. There is a separation bubble on the lower surface of the geometry in the close region of the base due to the flow separation while the separation bubble does not exist in the upper side of the geometry. The fluid flowing around the periphery of the model geometry brings out a saddle point immediately after the base point. For the rear section of the elliptical stern-II model geometry (See right column) that has a more elliptical curved surface, the separated bubble occurs around the periphery of the bordering of the stern. A saddle point for h/D = 0.5 occurs at a longer distance from the base of the geometry. The streamline is directed towards the free-surface owing to the lower pressure and rotational flow between the free-surface and uniform flow outer of the wake region. When the submergence depth ratio, h/D is increased as half size of geometrical diameter for example, at h/D = 0.75, the jet flow coming from the upper side of the geometry eliminates the nodal point and increase the distance of the saddle points from the rear side of the model geometry for the both appendages. The separated bubble size that occurred under the lower surface of the geometry is bigger than the upper one. The separation bubble emerging from the upper surface close to the rear end is moved towards the centerline of the geometry because of the effect of incoming flow from the restricted region between the upper surface of the model geometry and the free surface. Merging of the streamlines emanating from the circumference of the geometry takes place under the centerline of the wake region for both appendages. Further increment of the submergence depth ratio as h/D = 1.0, the separation bubble on the upper surface disappears for both appendages while the streamline patterns are creating a nodal-like flow stream above the centerline of the wake region. These converged streamlines combine with the free surface which is far away from the flow field of interest. For the submergence depth ratio of h/D = 1.5, foci occur in clockwise rotation over the upper surface and counterclockwise rotation over the bottom surface of the model in limited circulation and the shape of the foci is extending towards the wake due to the elliptical geometry of the rear part. The saddle points of the streamlines are placed approximately 0.7D from the base of both geometries. For the submergence depth ratios of *h/D* = 2.0, 2.5, 3.0 and 3.5, the influence of the free surface on the streamline topology diminishes and they almost have a symmetrical shape in the wake region. The cambered nose and elliptical stern-I geometry are slightly shorter owing to the less curved surface than the elliptical stern-II geometry, which is approximately 0.5D and 0.6D from the base of both geometries for *h/D* = 3.5, respectively. There are small foci occurring in the bottom section due to the three-dimensional flow characteristics.

The time-averaged streamline topology determined from the PIV measurements for the cambered nose and wingless elliptical stern-I geometry at submergence depths of *h/D* = 0.75, 1.0, 1.5, 2.0 and 3.0 for angle of attack of α = 0° for Re = $20x10^3$ (left column) and Re = $40x10^3$ (right column) is shown in Figure 4.29. Because of the unexpected PIV system error, the PIV measurements will be repeated in the future. However, the obtained streamline topology for all examined submergence depth ratios somehow different from the numerically calculated streamline topology, which might be laser reflection on the surfaces, insufficient laser source, other optical sources, and mechanical errors. The variations of the streamlines at *h/D* = 0.75 and 1.0 appear to be asymmetrical due to the dominant effect of the free surface. The separated flow encircles the stern part of the geometry for *h/D* = 1.5 and 2.0 at Re = $20x10^3$ whereas the streamline topology has almost symmetrical appearance having two foci recirculated counterclockwise and clockwise in the bottom and the upper half of the wake region for *h/D* = 3.0, respectively. The free-surface effect in the wake region of the torpedo-like geometry has been disappeared for *h/D* ≥ 2.0. For the submergence depth ratios of *h/D* = 2.0 and 3.0 at Re = $40x10^3$, the streamlines stick the surface of the geometry for the PIV measurements in the right column while the rotational wake region occurs for the numerical results given in Figure 4.28.

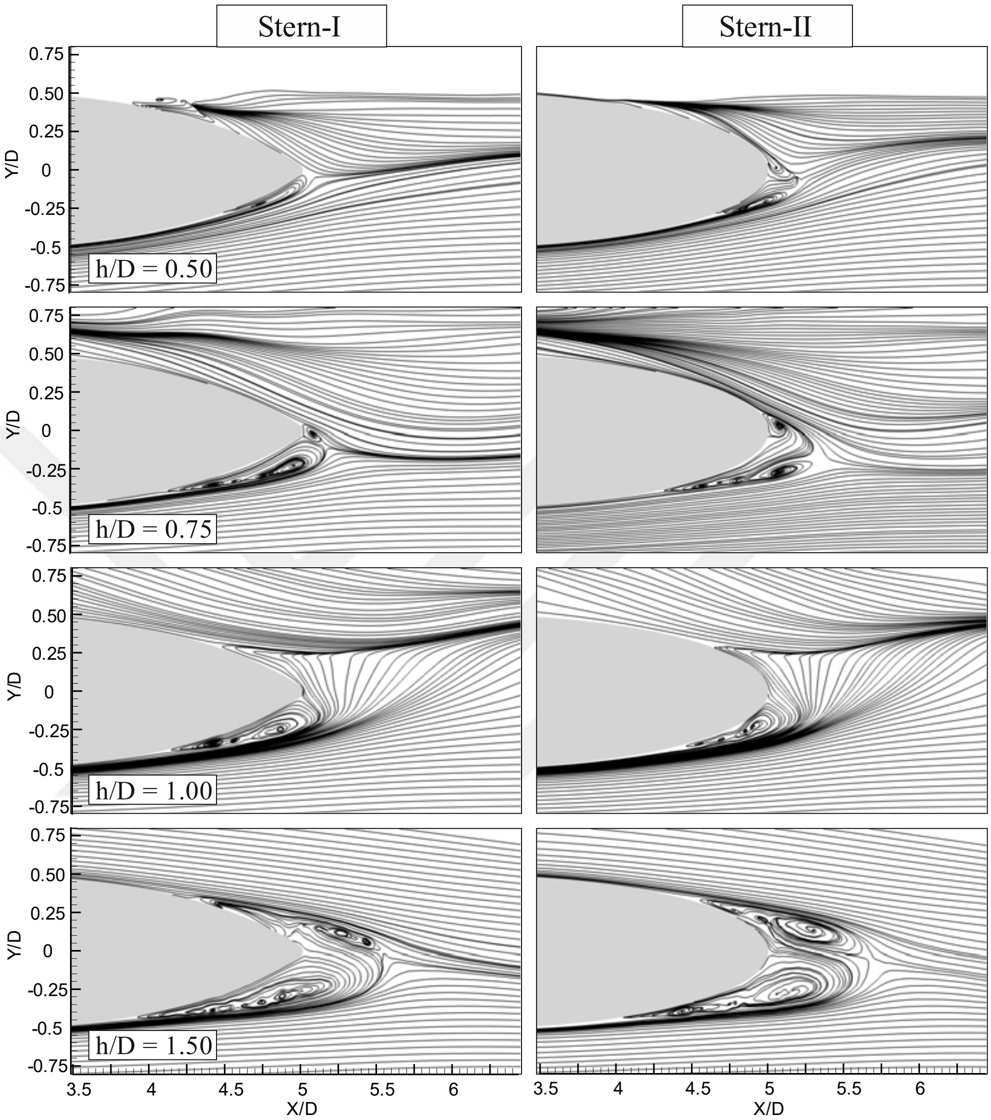

Figure 4.27: The time-averaged streamline topology <*Ψ*> calculated numerically for the torpedo-like geometry of elliptical stern-I and stern-II without wing at submergence depth ratios, *h/D* of 0.5, 0.75, 1.0 and 1.5 and for Re = $40x10^3$ and α = 0°

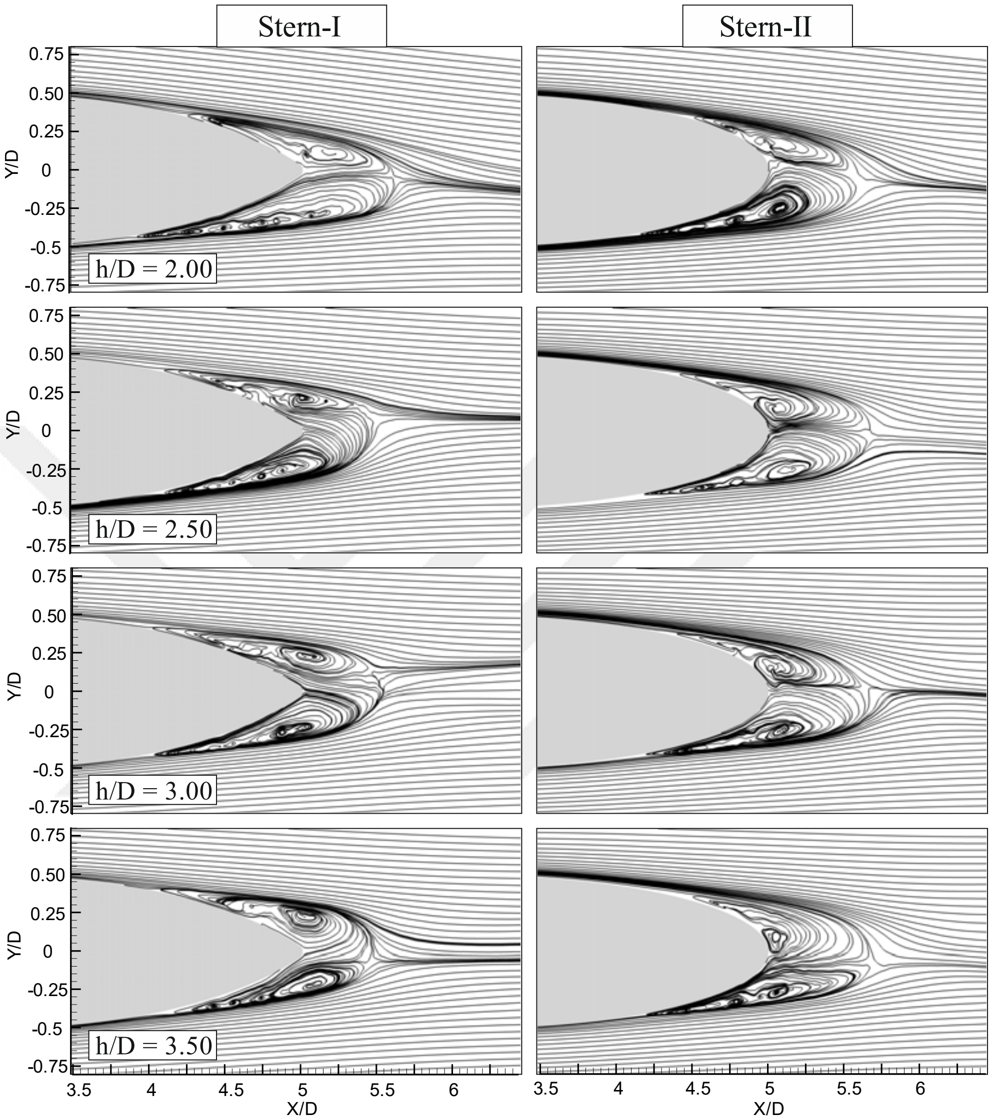

Figure 4.28: Continuation of 031 for submergence depth ratios, *h/D* of 2.0, 2.5, 3.0, and 3.5

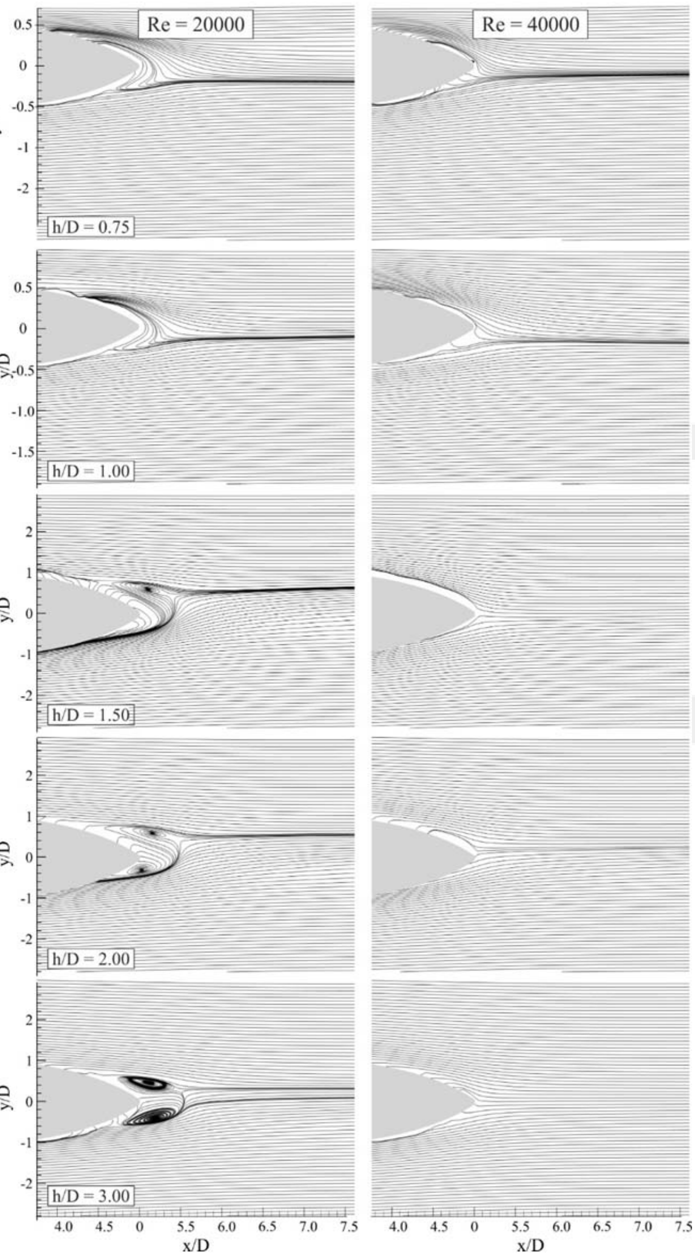

Figure 4.29. The time-averaged streamline topology <Ψ> calculated from the PIV for results the torpedo-like geometry of elliptical stern-I and stern-II without wing at submergence depth ratios, *h/D* of 0.75, 1.0, 1.5, 2.0 and 3.0, for Re = $20x10^3$ and $40x10^3$, and α = 0°

4.3. Comparison of Flow Characteristics of The Torpedo-Like Geometry Having 3-Winged And 4-Winged Stern-I

Comparison of the time-averaged dimensionless streamwise velocity contours $<u/U_\infty>$, cross-stream velocity contours $<v/U_\infty>$, vorticity contours $<\omega L/U_\infty>$ and TKE/U_∞^2 contours calculated from the CFD results for the cambered nose and elliptical stern-I geometry with 3-winged (See left column) and 4-winged (See right column) at submergence depth ratios of *h/D* = 0.50, 0.75, 1.0, 15, 2.0, 2.5, 3.0 and 3.5 for angle of attack of α = 0° at Re=40x10^3 are shown in Figures 034 – 040. For the touching and piercing the free surface cases for the 3-winged and 4-winged torpedo-like geometry, the incoming flow towards the model geometry accelerates close to the bottom side surface and around the nose. The magnitude of the velocity increase as much as 5% of the free stream, U_∞. The wake region has very small negative velocity. The wake region size of the 3-winged geometry is smaller than the 4-winged one. Because of the solution analogy for free surface flow with the turbulence LES model and VOF model together, mass flow rate occurs from the air-side to the water-side all along the water free-surface, the rate of air which enters to the water increases when the gap between the model geometry and water free-surface increases from *h/D*=0.5 to 0.75. the jet-like flow retards the reattachment of the separated flow (i.e, vortex shedding) to the free surface. For the *h/D* = 1.0, the highest acceleration realizes the region between the free surface and upper surface of the model. Lower velocity field increases at *h/D* = 1.0 case compared to the submergence depth ratios of *h/D* = 0.5 and 0.75. The free surface affects the velocity magnitudes until *h/D* = 2.0. After this submergence depth ratio, *h/D*, the separated flow around the model geometry is trying to be symmetric. For the contours of crosswise velocity component, $<v/U_\infty>$ have a similar variation and smaller velocity magnitude are observed around the wings because these wings retard the flow separation from the surface of the model geometry. For *h/D*=3.5, the distributions of crosswise velocity component $<v/U_{\infty}>$ becomes almost symmetrical. The vorticity contours are presented in Figure 4.34, for the submergence depth ratio of *h/D* = 1.0, the flow over the free surface or the flow between the model geometry and water free-surface creates a larger variation of velocity gradient and time-averaged dimensionless vorticity, $<\omega\ L/U_{\infty}>$. For the higher submergence depth ratio, *h/D* the dimensionless vorticity concentrations, $<\omega\ L/U_{\infty}>$ around the free surface diminish. For the submergence depth ratios higher than *h/D* = 2.0, the vorticity, $<\omega\ L/U_{\infty}>$ contours wrap the model body until the beginning of wings where a small eddy starts to develop. The dimensionless turbulent kinetic energy contours $<TKE/U_{\infty}^2>$ calculated from the CFD predictions for the cambered nose and elliptical stern-II geometry with 3-winged (see left column) and 4-winged (See right column) at submergence depth ratios of *h/D* = 0.5, 0.75, 1.0 1.5, 2.0, 2.5, 3.0 and 3.5 for angle of attack of α = 0° and Re = $40x10^3$ is exhibited in Figures 039 and 040. The dimensionless TKE occurs with a higher ratio around the intermediate surface between air and water for the submergence depth ratios of *h/D* = 0.5, 0.75 and 1.0. For the higher values of the submergence ratios such as *h/D* = 2.0 – 3.5, the dimensionless TKE variation occurs dominantly in the wake region. The magnitudes of the dimensionless TKE in the case of the 4-wings is lower than the 3-winged case.

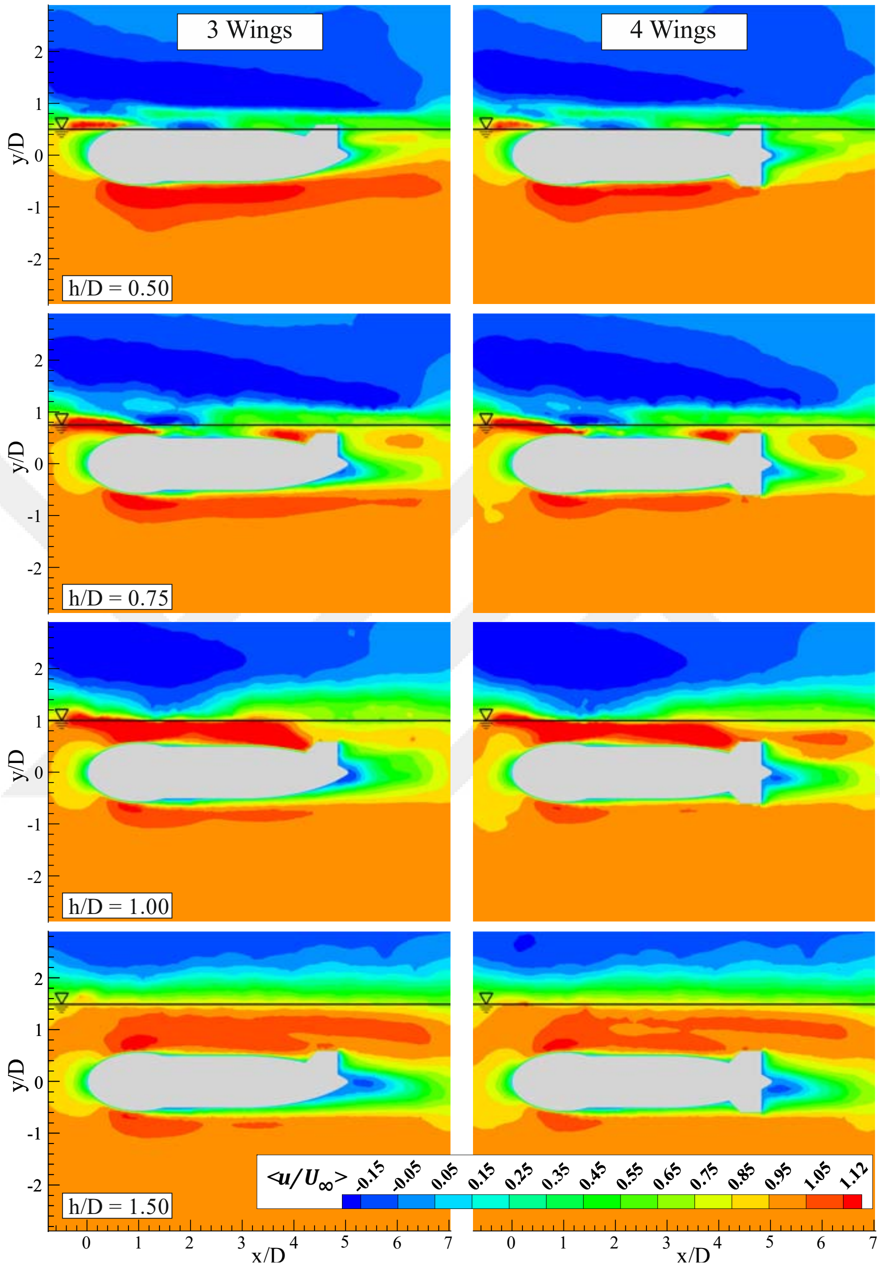

Figure 4.30. Contours of the time-averaged dimensionless streamwise velocity component $<u/U_\infty>$ calculated numerically for the torpedo-like geometry of elliptical stern-I with 3-winged and 4-winged at submergence depth ratios, *h/D* of 0.5, 0.75, 1.0 and 1.5 and for Re = 40x10^3 and α = 0°

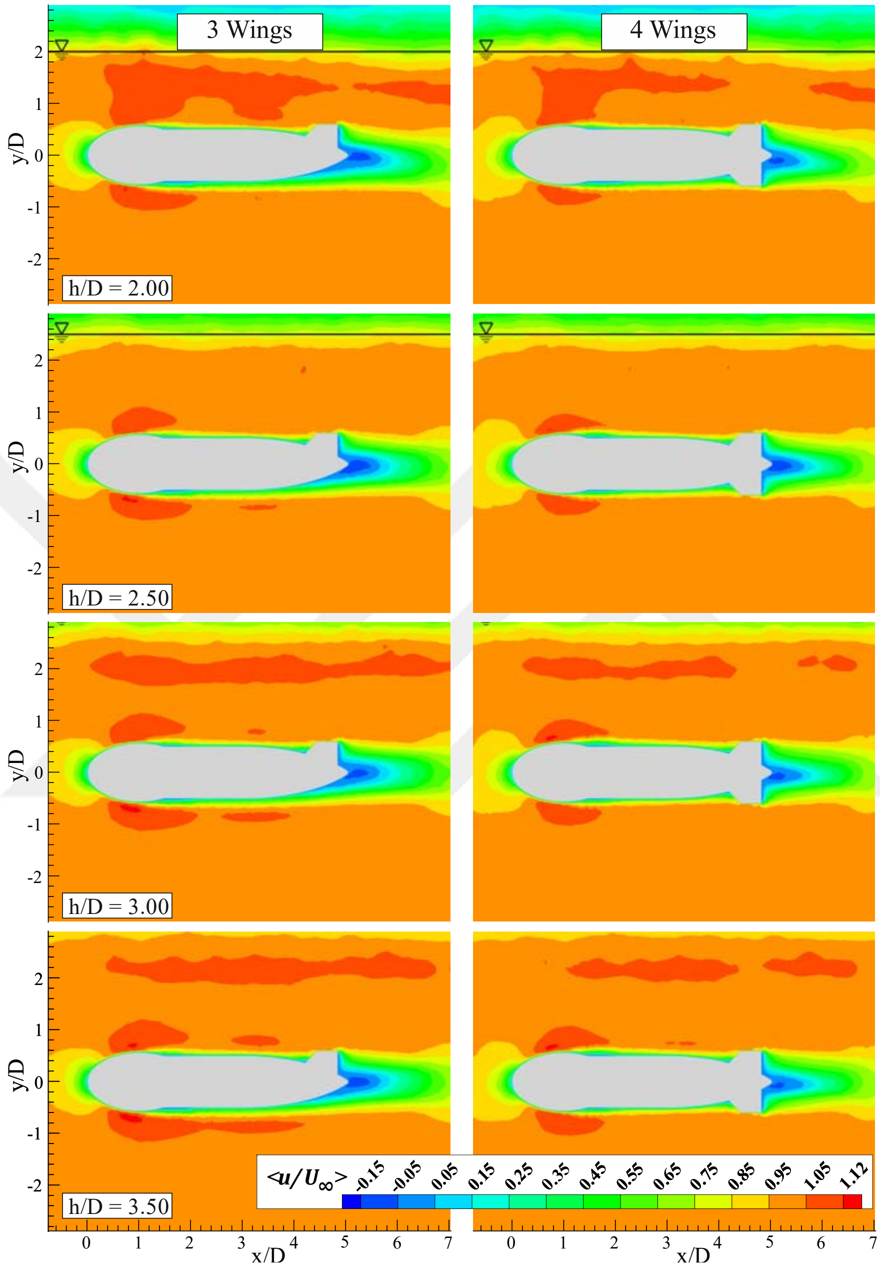

Figure 4.31. Continuation of Figure 4.30 for submergence depth ratios, *h/D* of 2.0, 2.5, 3.0, and 3.5

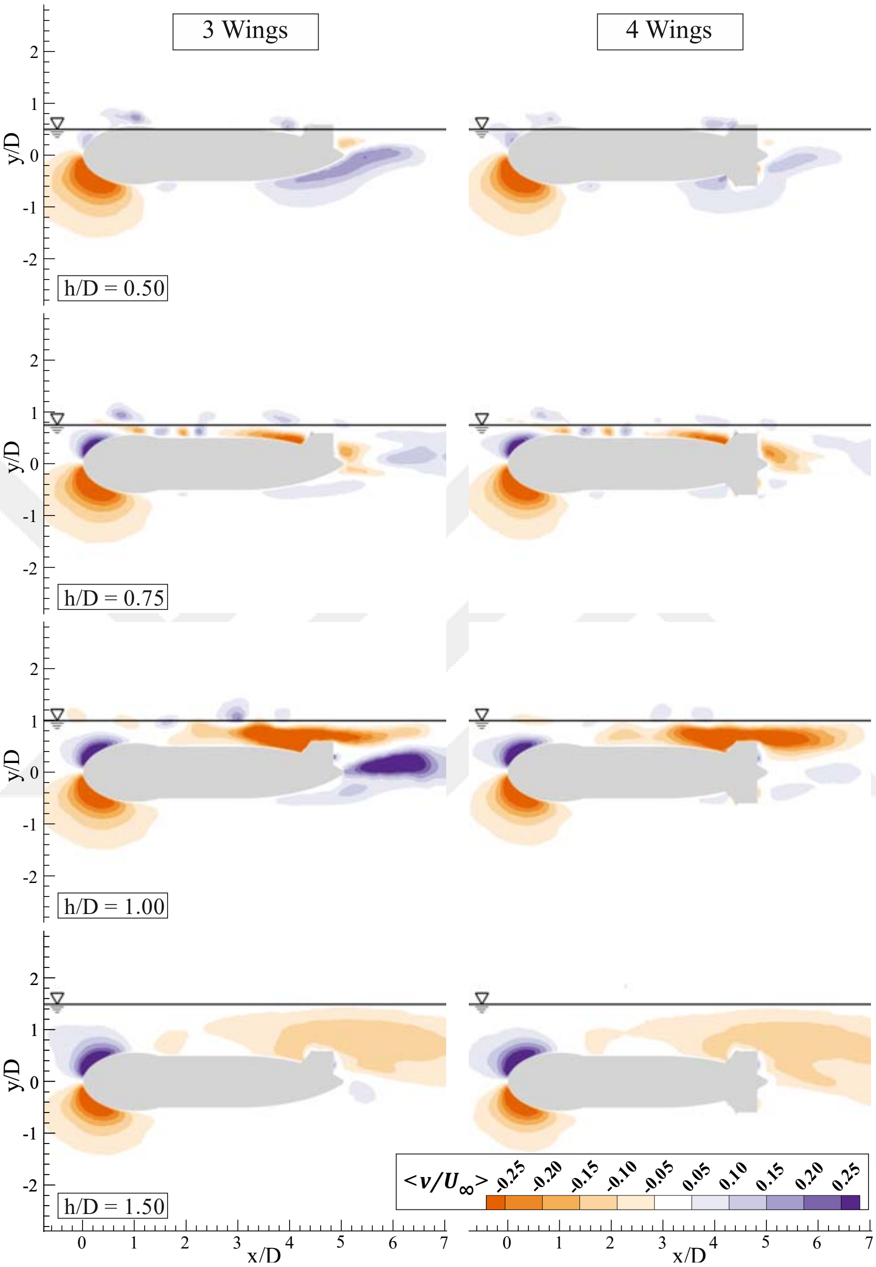

Figure 4.32. Contours of the time-averaged dimensionless crosswise velocity component $<v/U_\infty>$ calculated numerically for the torpedo-like geometry of elliptical stern-I with 3-winged and 4-winged at submergence depth ratios, *h/D* of 0.5, 0.75, 1.0 and 1.5 and for Re = 40×10^3 and α = 0°

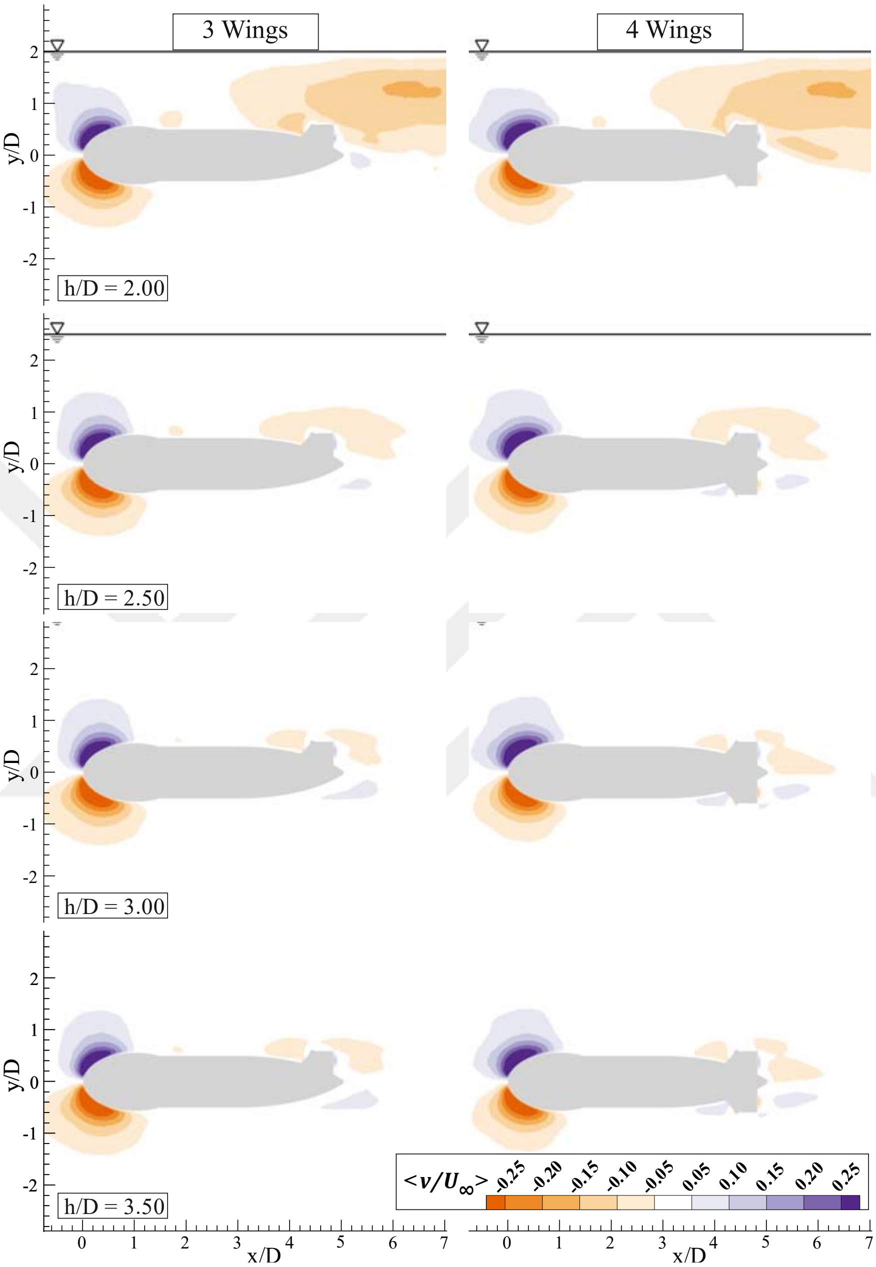

Figure 4.33. Continuation of Figure 4.32 for submergence depth ratios, *h/D* of 2.0, 2.5, 3.0, and 3.5

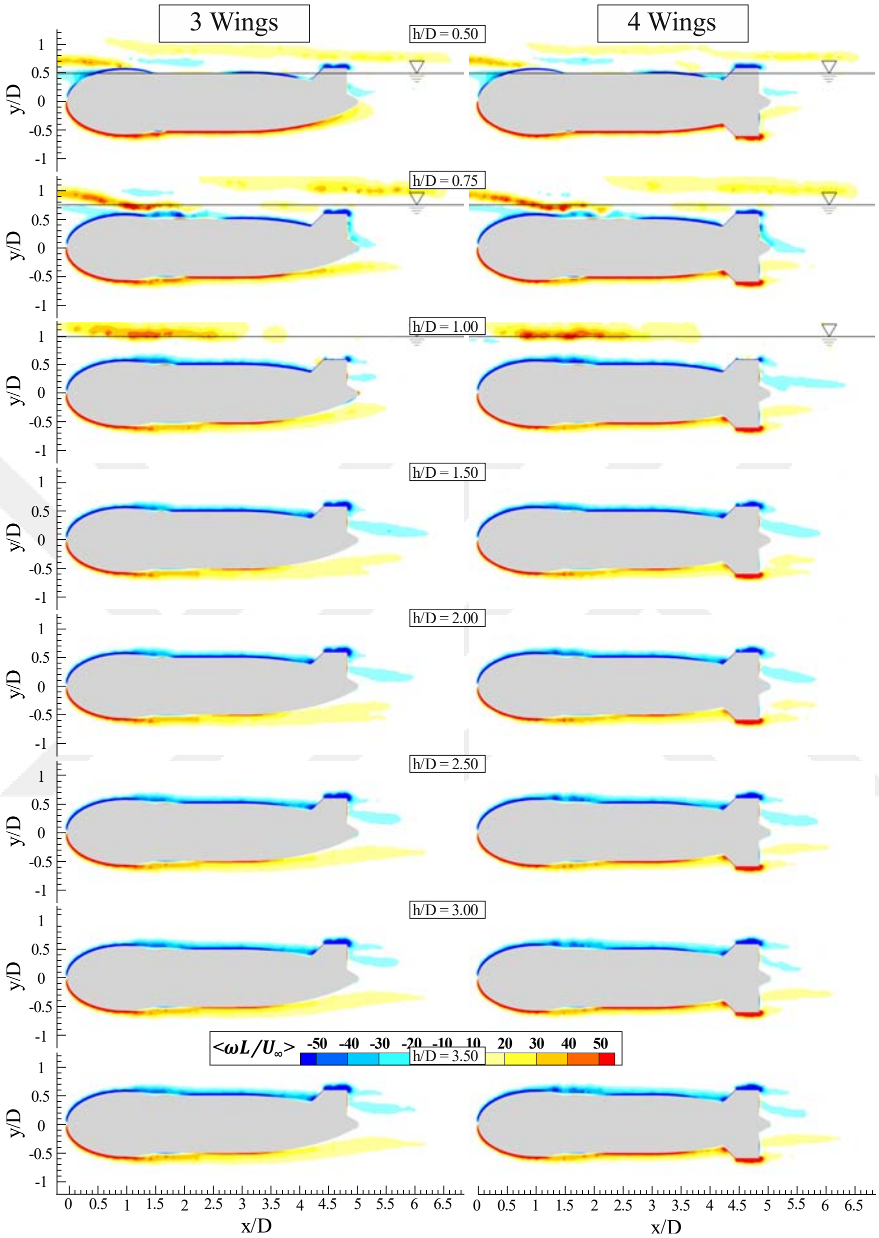

Figure 4.34: Contours of the time-averaged dimensionless vorticity $<\omega\, L/U_{\infty}>$ calculated numerically for the torpedo-like geometry of elliptical stern-I with 3-winged and 4-winged at submergence depth ratios, *h/D* of 0.5, 0.75, 1.0, 1.5, 2.0, 2.5, 3.0, and 3.5 and for Re = $40x10^3$ and α = 0°

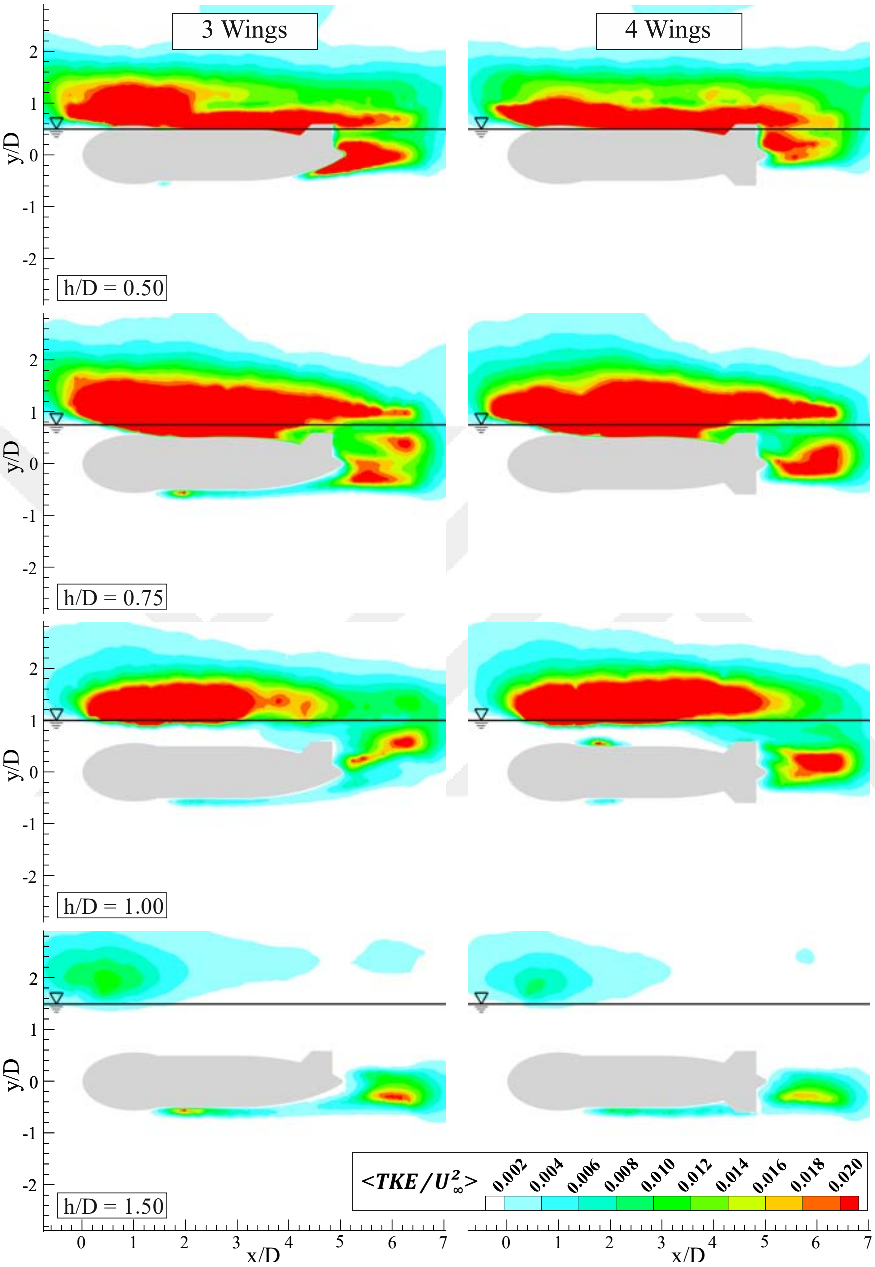

Figure 4.35. Contours of the time-averaged turbulent kinetic energy $<TKE/U_{\infty}>$ calculated numerically for the torpedo-like geometry of elliptical stern-I with 3-winged and 4-winged at submergence depth ratios, *h/D* of 0.5, 0.75, 1.0 and 1.5 and for Re = 40×10^3 and α = 0°

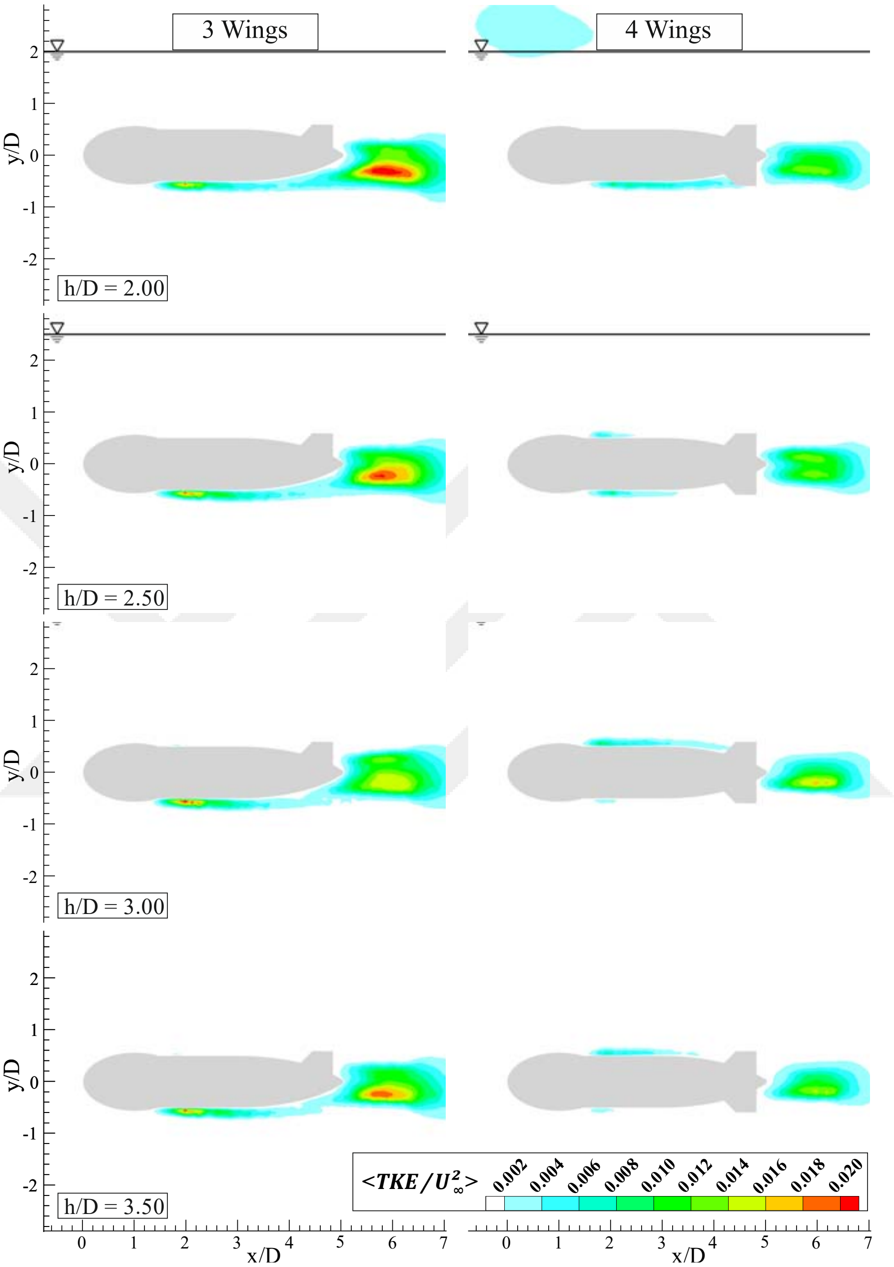

Figure 4.36: Continuation of Figure 4.35 for submergence depth ratios, *h/D* of 2.0, 2.5, 3.0, and 3.5

4.3.1. Streamlines

Variation of the time-averaged streamline topology calculated from the CFD results for the cambered nose and elliptical stern-I geometry with 3-winged (See left column) and with 4-winged (See right column) at submergence depths ratios of *h/D* = 0.50, 0.75, 1.00, 1.5, 2.0, 2.5, 3.0, and 3.5 for angle of attack of α = 0° at Re = $40x10^3$ is depicted in Figures 041 and 042. For the submergence depth ratio of *h/D* = 0.5, the time-averaged streamline topology <Ψ> calculated numerically for the geometry having 3-wings inserted to the model geometry do not create a separation bubble in the lower surface while nodal point occurs over the upper surface due to the free-surface modification. Right in front of the wing, a tiny horseshoe vortex is developed due to the joint of the model body. A saddle point appears very close to the base of the geometry. For the 4-winged case, a horseshoe vortex occurs which starts to develop in front of the upper side of the wing and a recirculated bubble appears downstream of the wing. For both 3-winged and 4-winged cases, the flow passing the wing is directed towards the free-surface owing to the lower pressure distributions. For *h/D* = 0.75, the jet-like flow emanating from the upper side of the geometry eliminates the horseshoe vortex for both the 3-winged and 4-winged cases. A small size separated bubble appears on the lower surface of the model geometry at the wing location for the 3-winged geometry where the separation bubble occurs downstream of the 4-winged case. The streamlines topology <Ψ> reveals that the fluid in the core flow region is directed towards the wake from the upper surface of the torpedo-like geometry. The pattern of streamlines, <Ψ> picks up a line below the center of the geometry which elongates horizontally from the saddle point. Under this line, the streamlines demonstrate parallel lines which indicate that the velocity distribution is uniform in the indicated region. For the submergence depth ratio of *h/D* = 1.0, the free-surface effect decreases, wake region size of both 3-winged and 4-winged cases have a larger area and the separation bubble originates from the bottom surface. Wake region recovers in a short distance for the 4-winged cases. In summary, the streamline topology <Ψ> reveals that the flow maintains the asymmetric structure. For the higher submergence depth ratios of *h/D* = 2.5, 3.0 and 3.5, the streamline topology indicates two limited sizes of recirculating baubles rotation in opposite directions. The spiral-shaped contours of the streamline in both sides according to the line passing through a centerline of the model geometry are not equal due to the possibility of mixing the flow caused by wings. A saddle point occurs around 0.6D from the base of the cambered nose and elliptical stern-I geometry with 3-winged and 4-winged models. The appearance of the time-averaged streamlines, <Ψ> shows that the uniform flow condition takes place in a shorter distance which less than 1D. These can be interpreted that the insertion of wings at the rear end of the model controls the flow characteristics substantially.

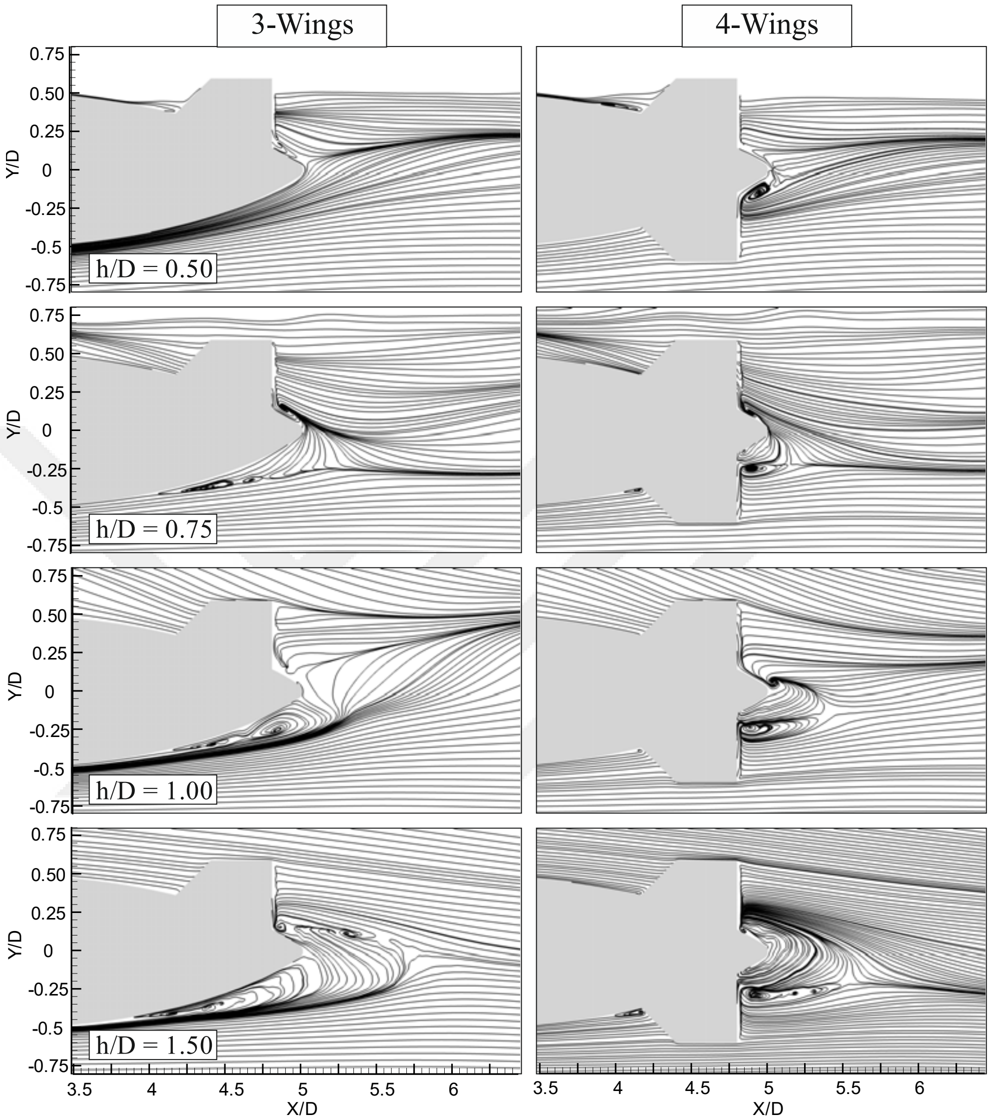

Figure 4.37. The time-averaged streamline topology <Ψ> calculated numerically for the torpedo-like geometry of elliptical stern-I with 3-winged and 4-winged at submergence depth ratios, *h/D* of 0.5, 0.75, 1.0 and 1.5 and for Re = 40×10^3 and α = 0°

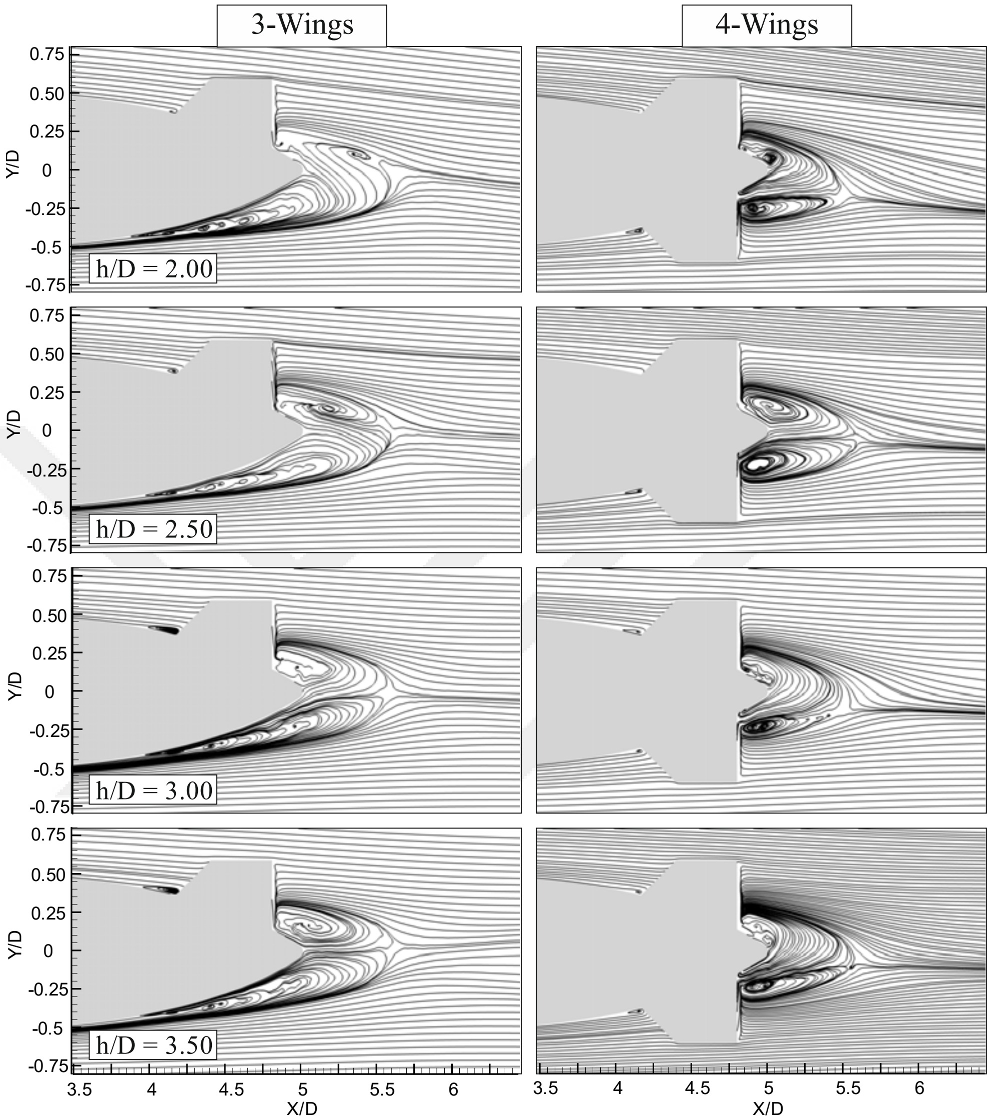

Figure 4.38. Continuation of Figure 4.37 for submergence depth ratios, *h/D* of 2.0, 2.5, 3.0, and 3.5

4.4. Variation of Instantaneous and Time-Averaged Drag Coefficients for Torpedo-Like Geometries

Variation of instantaneous drag coefficient, C_D with time for the cambered nose geometry and four different stern sections; wingless elliptical stern-I, wingless elliptical stern-II, 3-wings elliptical stern-I, and 4-winges elliptical stern-I are shown in Figures 043 – 046. Re=40x10^3 case, drag coefficient, C_D converges around 15s which is almost 212 iteration steps. However, at Re=20 x10^3, the instantaneous drag coefficient, C_D still fluctuates expanding the duration of time beyond 17 sec (i.e., 168 iteration steps). Because of the limited computer facility, the lower Reynolds number case needs larger computer facility and time for convergence and hence the results can be predicted more precisely. The instantaneous drag coefficient, C_D values decrease as the submergence depth ratio, *h/D* of the torpedo-like geometry are positioned to a deeper location in the water flow domain for both Reynolds numbers (Re=20 x10^3 and 40 x10^3). Variation bands of the instantaneous drag coefficient, C_D are around ±5% for Re = 40x10^3 while it is more than ±15% for Re = 20x10^3. The reason for these variations might be due to the effect of the free surface, having lower kinetic energy at Re=20 x10^3 and increasing hydrodynamic pressure with depth.

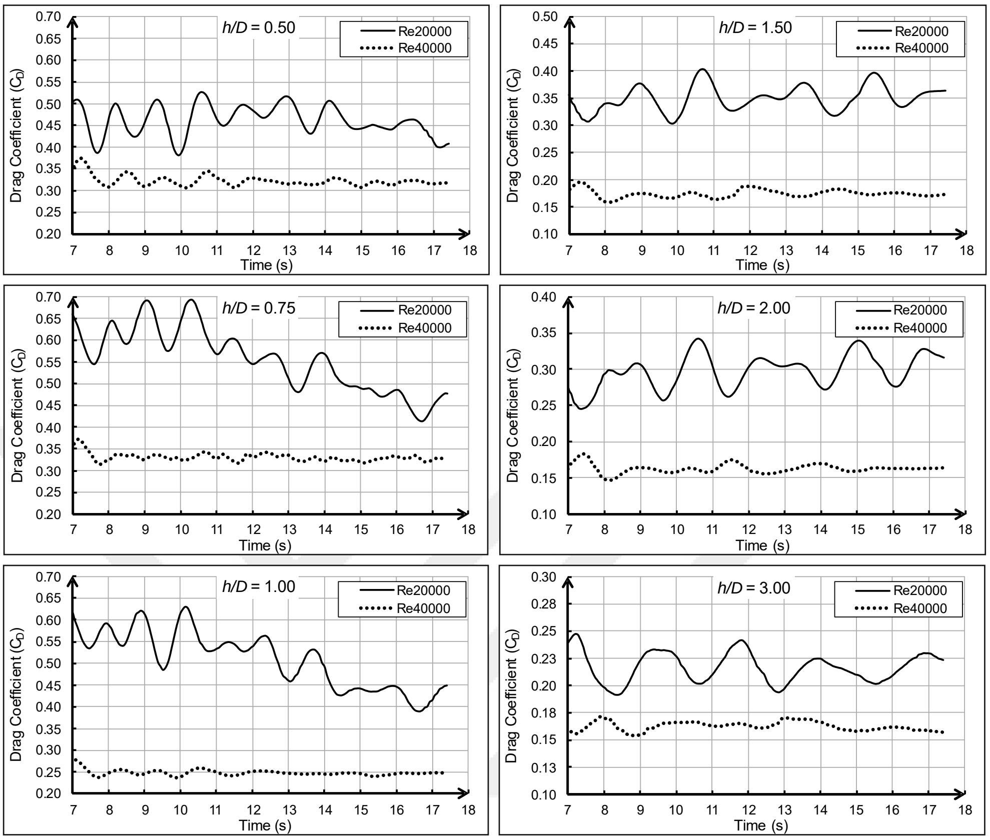

Figure 4.39. Variation of instantaneous drag coefficient, C_D with time for the cambered nose geometry with wingless stern-II at the angle of attack, α = 0° and submergence depth ratios of 0.5 ≤ *h/D* ≤ 3.0 for Reynolds numbers of Re=2x10^4 and 4x10^4

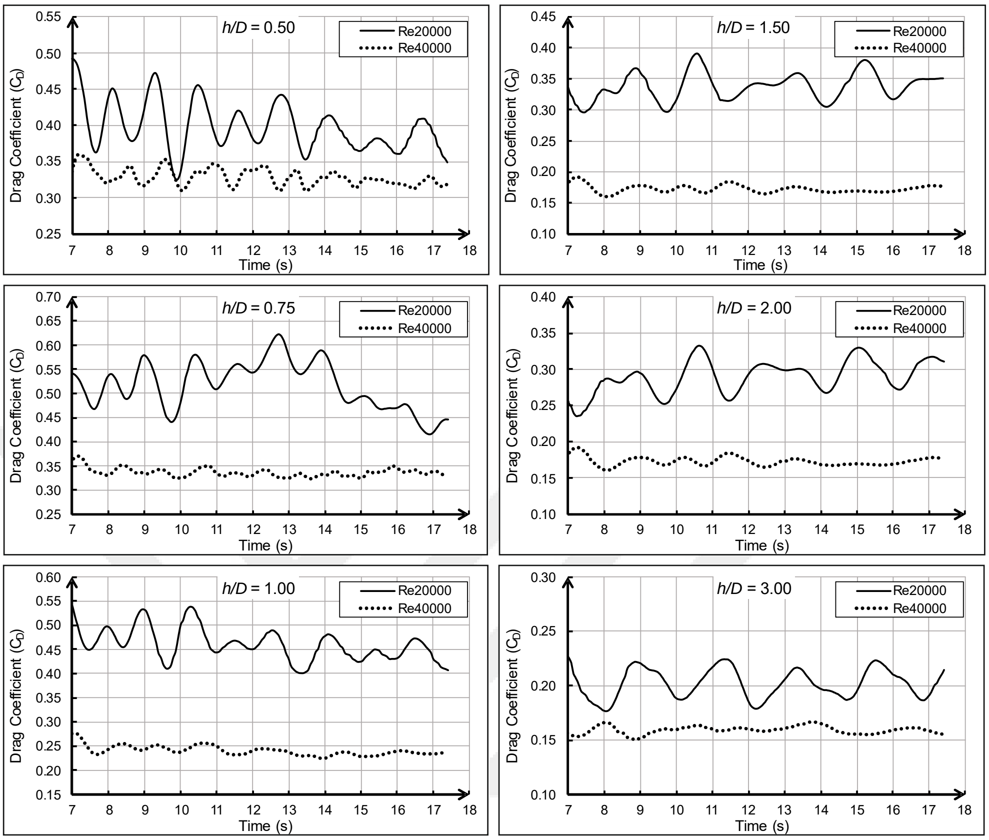

Figure 4.40. Variation of instantaneous drag coefficient, C_D with time for the cambered nose geometry with wingless stern-I at the angle of attack, α = 0° and submergence depth ratios of $0.5 \le h/D \le 3.0$ for Reynolds numbers of Re=2x10^4 and 4x10^4

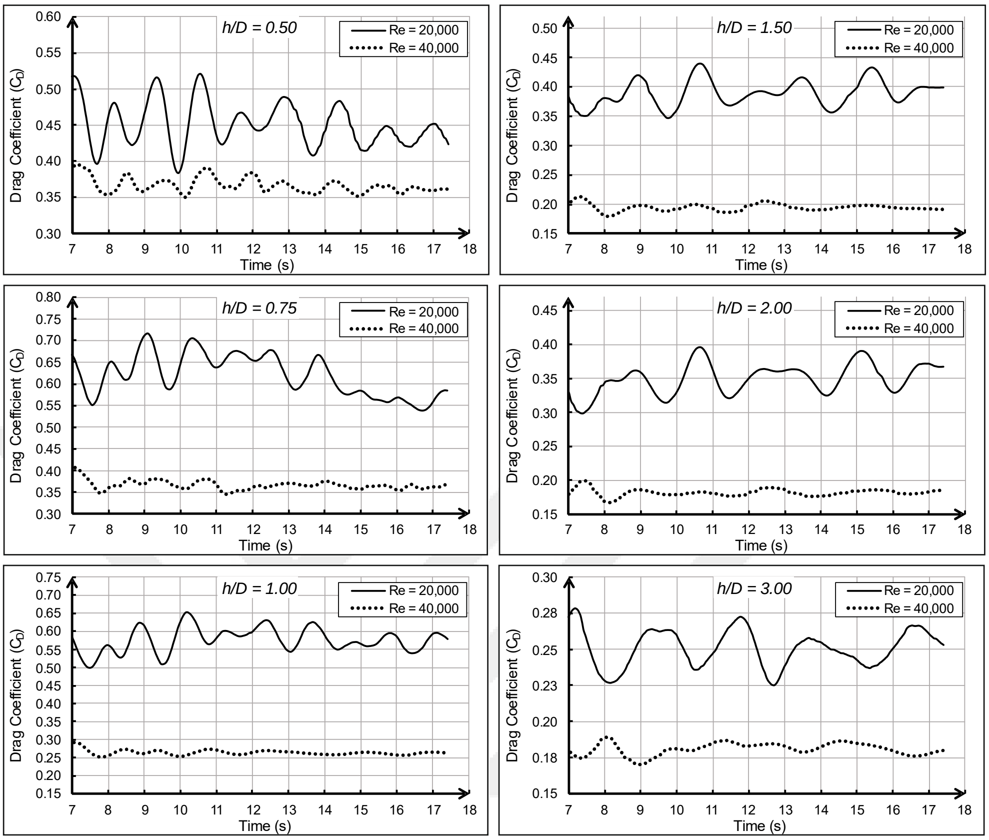

Figure 4.41. Variation of instantaneous drag coefficient, C_D with time for the cambered nose geometry with 3-winged stern-I at the angle of attack, α = 0° and submergence depth ratios of 0.5 ≤ *h/D* ≤ 3.0 for Reynolds numbers of Re=2x10^4 and 4x10^4

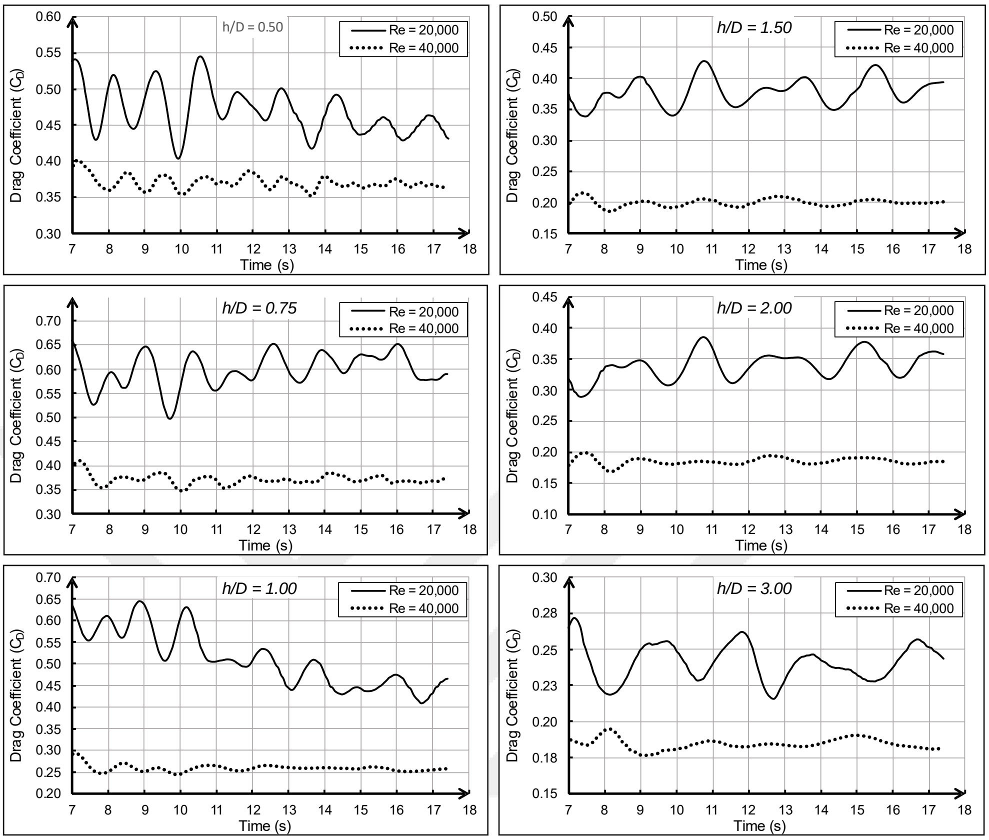

Figure 4.42. Variation of instantaneous drag coefficient, C_D with time for the cambered nose geometry with 4-winged stern-I at the angle of attack, α = 0° and submergence depth ratios of 0.5 ≤ *h/D* ≤ 3.0 for Reynolds numbers of Re=$2x10^4$ and $4x10^4$

Variation of time-averaged drag coefficient, C_D values depending on the submersion ratio and Reynolds numbers for the cambered nose and the aforementioned four different stern sections which are given in Tables 05– 08 and Figures 047 – 051.

Table 4.1 Variation of time-averaged drag coefficient values for the torpedo-like geometry of the cambered nose and wingless stern-I

h/D	Re = 20000	Re = 40000
0.50	0.3989	0.3256
0.75	0.5105	0.3375
1.00	0.4609	0.2419
1.50	0.3367	0.1732
2.00	0.2891	0.1590
2.50	0.2080	0.1571
3.00	0.2020	0.1600
3.50	0.2161	0.1669

Table 4.2 Variation of time-averaged drag coefficient values for the torpedo-like geometry of the cambered nose and wingless stern-I

h/D	Re = 20000	Re = 40000
0.50	0.4574	0.3287
0.75	0.5553	0.3322
1.00	0.5127	0.2482
1.50	0.3478	0.1740
2.00	0.2966	0.1632
2.50	0.2243	0.1577
3.00	0.2158	0.1620
3.50	0.2279	0.1669

Table 4.3 Variation of time-averaged drag coefficient values for the geometry consisting of the cambered nose and elliptical stern-I with 3-wings at Re = 40x10^3.

h/D	0°	4°	8°	12°
0.50	0.3680	0.3716	0.3498	0.3889
0.75	0.3682	0.4195	0.5070	0.4963
1.00	0.2671	0.2940	0.4005	0.6006
1.50	0.1943	0.2022	0.2504	0.3263
2.00	0.1815	0.1876	0.2321	0.2946
2.50	0.1782	0.1891	0.2368	0.3018
3.00	0.1819	0.1954	0.2431	0.3134
3.50	0.1884	0.2010	0.2506	0.3179

Table 4.4 Variation of time-averaged drag coefficient values for the geometry consisting of the cambered nose and elliptical stern-I with 4-wings at Re = 40x10^3

h/D	0°	4°	8°	12°
0.50	0.3719	0.3836	0.3858	0.4203
0.75	0.3715	0.4370	0.5168	0.5257
1.00	0.2611	0.2892	0.4133	0.6243
1.50	0.1999	0.2063	0.2594	0.3349
2.00	0.1857	0.1937	0.2365	0.3074
2.50	0.1823	0.1960	0.2458	0.3163
3.00	0.1853	0.2013	0.2548	0.3264
3.50	0.1920	0.2063	0.2603	0.3336

Variations of time-averaged drag coefficient values against submergence depth ratios, *h/D* for the geometry consisting of the cambered nose and four different stern sections (wingless stern-I, wingless stern-II, 3-winged stern-II, and

4-winged stern-II) at Re = $20x10^3$ and Re = $40x10^3$ for angle of attack values of 0°, 4°, 8°, and 12° are displayed in Figures 047 – 051. All of the examined torpedo-like geometries have similar trends. The time-averaged drag coefficient values for the angle of attacks (4°, 8°, and 12°) are increasing for submergence depth ratios of *h/D* = 0.5, 0.75 and 1.0. After *h/D* = 2.0 the drag coefficient values decrease and become almost constant for each angle of attack. For the larger angle of attack, the bigger time-averaged drag coefficient values were found. The stern-I profile with 3-wings and 4-wings have caused higher time-averaged drag coefficient values with respect to the wingless stern-I. However, it found that the wings geometries affect the wake region flow characteristics positively.

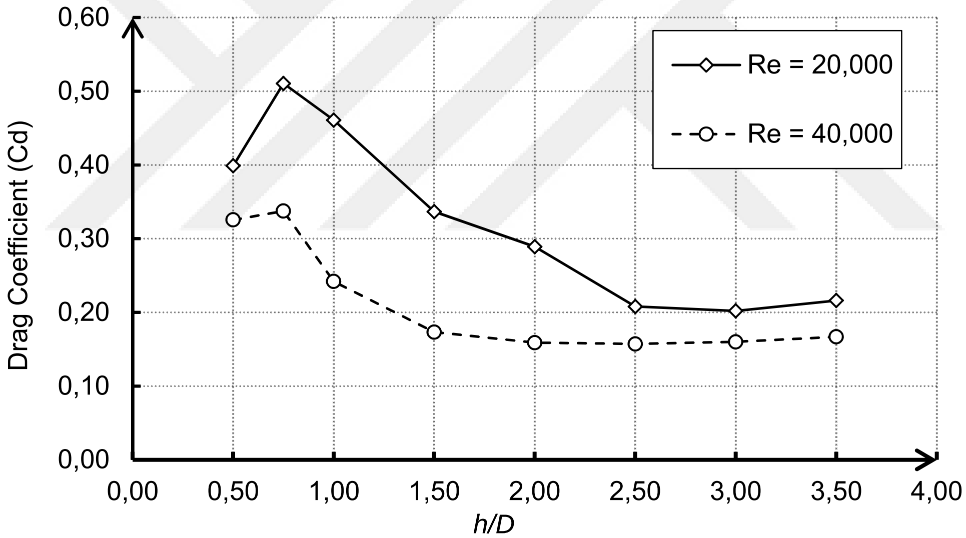

Figure 4.43. Variations of time-averaged drag coefficient values against to submergence depth ratios for the geometry consisting of the cambered nose and wingless elliptical stern-I at Re = $20x10^3$ and Re = $40x10^3$

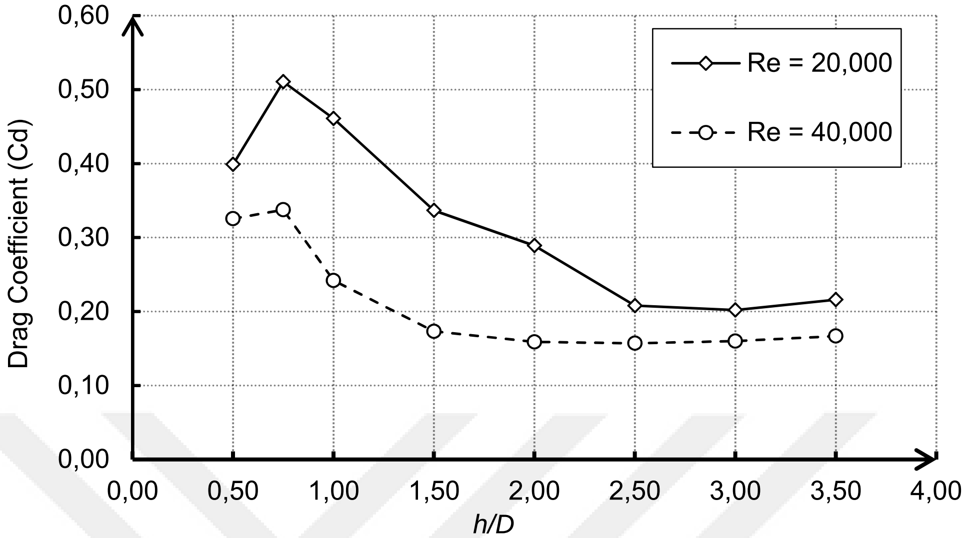

Figure 4.44. Variations of time-averaged drag coefficient values against to submergence depth ratios for the geometry consisting of the cambered nose and wingless elliptical stern-II at Re = $20x10^3$ and Re = $40x10^3$

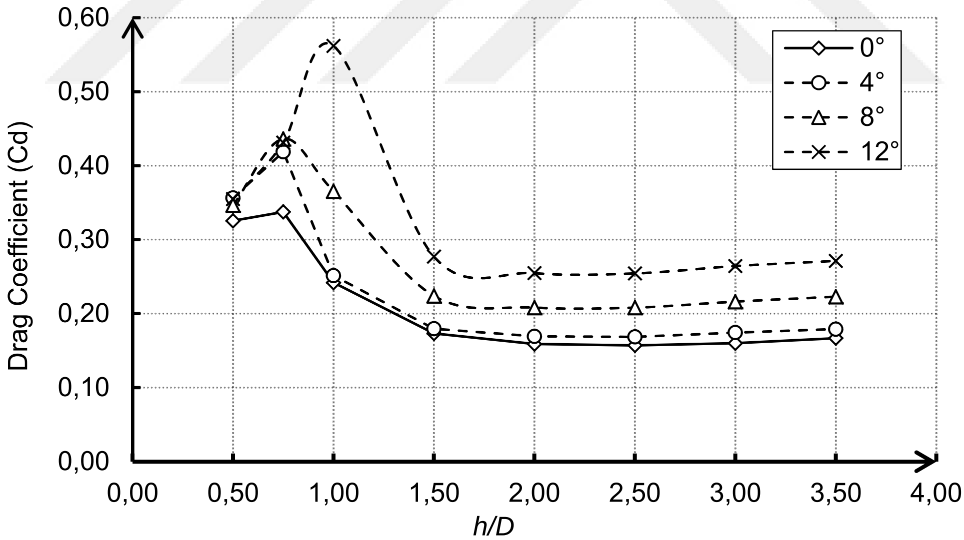

Figure 4.45: Variations of time-averaged drag coefficient values against to submergence depth ratios for the geometry consisting of the cambered nose and wingless elliptical stern-I at Re = $40x10^3$ for angles of attack values of 0°, 4°, 8°, and 12°.

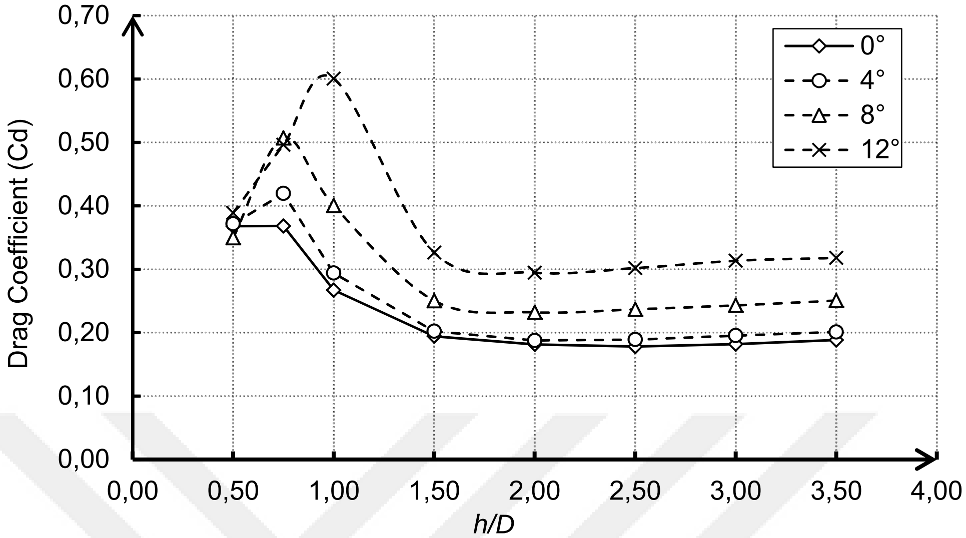

Figure 4.46. Variations of time-averaged drag coefficient values against to submergence depth ratios for the geometry consisting of the cambered nose and elliptical stern-I with 3-winged at Re = $40x10^3$ for angles of attack of 0°, 4°, 8°, and 12°.

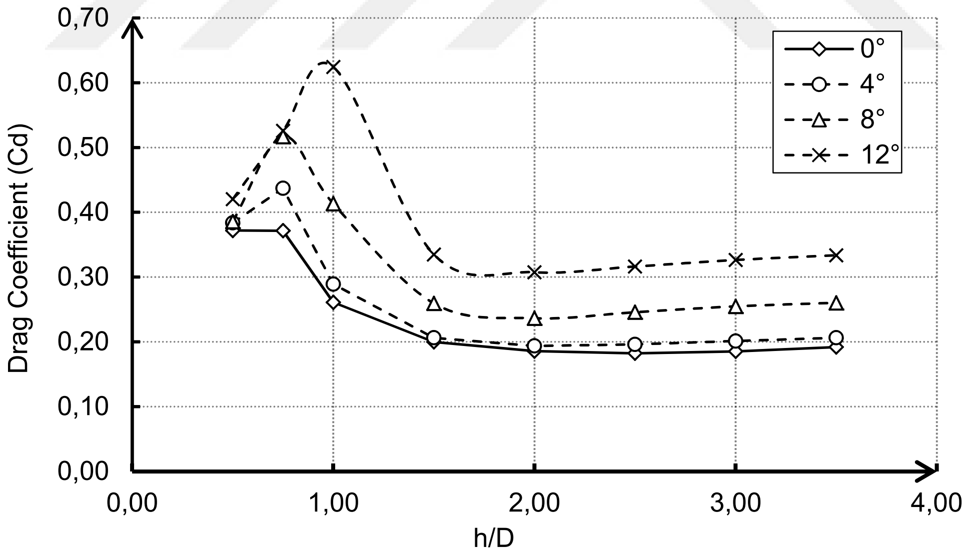

Figure 4.47. Variations of time-averaged drag coefficient values against to submergence depth ratios for the geometry consisting of the cambered nose and elliptical stern-I with 4-winged at Re = $40x10^3$ for angles of attack of 0°, 4°, 8°, and 12°.

4.5. Variation of Vortex Shedding Frequency

The dominant vortex shedding frequency, f_s is determined from the power spectra of instantaneous drag values calculated numerically for the model geometries. Statistical characteristic of the instantaneous values of streamwise velocities $<u/U_\infty>$ are determined in order to get information in the frequency domain by using spectral analysis, i.e. Fast Fourier Transformation (FFT). FFT analysis in the wake of the model reveals significant quasi-periodic flow oscillations. As is known, the most powerful spectral peak reflects the vortex shedding frequency in the spectra. The input data number for frequency spectra should be the power of 2 (Ozgoren, 2006). In this section, vortex shedding frequency, f_s in the wake region for four different torpedo-like geometries examined by the numerical analysis is calculated from the Fast Fourier Transformation, (FFT) process by deriving the velocity in the direction of flow at different points in XY-plane over time, and then the graphs of power spectral density with vortex shedding frequency, f_s are established. The obtained vortex shedding frequencies f_s are given in Table 4.5.

Table 4.5. Variation of vortex shedding frequency, f_s for the four models of the torpedo-like geometries at the angle of attack, α = 0°

h/D	Wingless Stern-I Re (x10^3)		Wingless Stern-II Re (x10^3)		3-winged Stern-I Re (x10^3)		4-winged Stern-I Re (x10^3)	
	20	40	20	40	20	40	20	40
0.50	0.875	0.840	0.850	0.840	0.788	0.840	0.788	0.840
0.75	0.869	0.840	0.525	0.840	1.100	0.840	0.875	0.840
1.00	0.875	0.869	0.875	0.910	0.875	0.840	0.875	0.840
1.50	0.700	0.770	0.438	0.840	0.490	0.802	0.438	0.770
2.00	0.438	0.770	0.438	0.700	0.438	0.770	0.438	0.770
2.50	0.490	0.446	0.438	0.780	0.438	0.490	0.485	0.490
3.00	0.438	0.490	0.438	0.840	0.438	0.630	0.438	0.613
3.50	0.875	0.840	0.850	0.840	0.788	0.840	0.788	0.840

The values representing the dimensionless frequency ($St = f\ L/U_\infty$) of the dominant frequency values are calculated for different submergence depth ratios at Reynolds numbers of 20 x10^3 and 40 x10^3. Figures 052 and 053 show the variation of Strouhal number with submergence depth ratios, h/D for the four models of torpedo-like geometries. The highest vortex shedding frequency, f_s for the torpedo-like geometry having Stern-II occurs at Re = 20x10^3 and h/D = 1. At the submergence depth ratios of h/D = 0.5 and 1, the Strouhal numbers, St were approximately the same. This is due to the jet-like flow formed between the upper boundary of the model geometry and the water free-surface, resulting in the higher flow of vortex shedding by affecting the separated circulating flow in the wake region. In the case of h/D = 0.5 where the upper boundary of the model geometry is in contact with the water free-surface, the vortex shedding occurs only at the lower boundary of the torpedo-like geometry. The separated flow is directed by momentum transfer to the free surface with the effect of inertial forces as described in the Reynolds number. This non-permanent flow causes more complex turbulent flow under the effect of the free surface. Free-surface deformation also occurs due to the partial contact of geometry with the free surface. The surface deformation occurs and transforms in a waveform and this also increases the rate of turbulence within the wake. An increase of the Strouhal number, St were observed for the four examined torpedo-like geometries owing to the interaction between the separated flow and the streamwise velocity fluctuations caused by the deformation of water free-surface. The high frequency of vortex shedding at submergence depth ratios, h/D = 0.75 and 1 is explained by the momentum transfer to the wake region which is caused by the formation of the jet-like flow in the region in-between the upper side of the model geometry and the free surface (Figures 052 and 053).

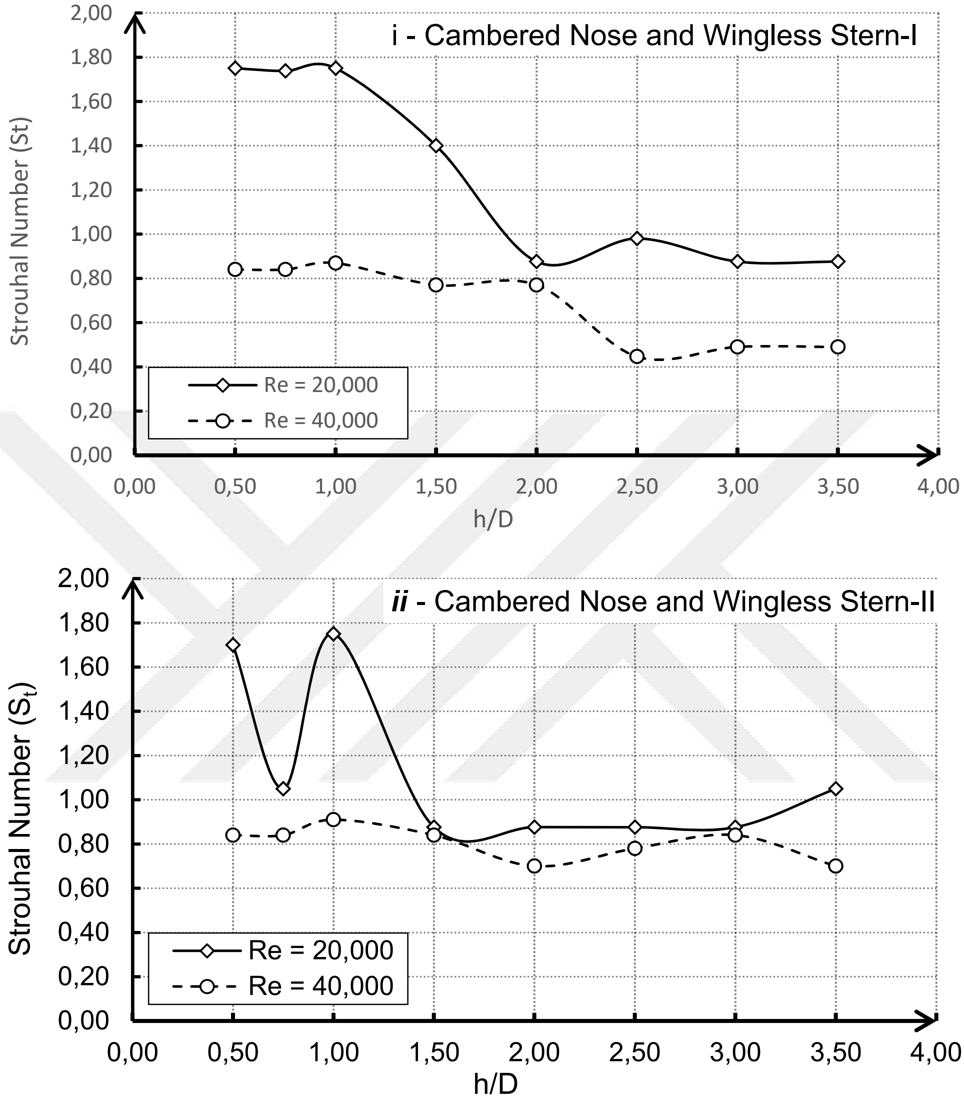

Figure 4.48. Variations of Strouhal numbers, S_t against submergence depth ratios *h/D* for the geometry consisting of the cambered nose and wingless elliptical (i) Stern-I and (ii) Stern-II for the angle of attack α = 0° at Re = 20x10^3 and 40x10^3

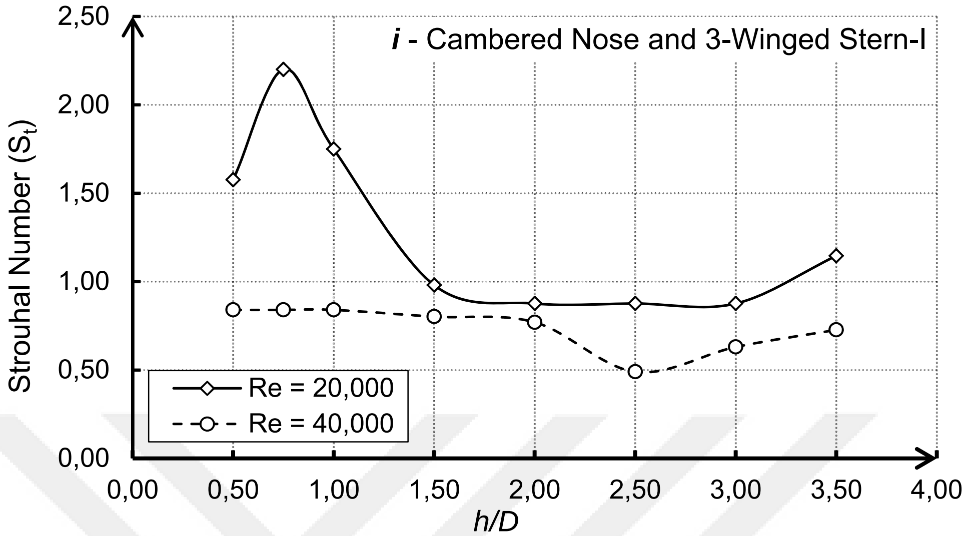

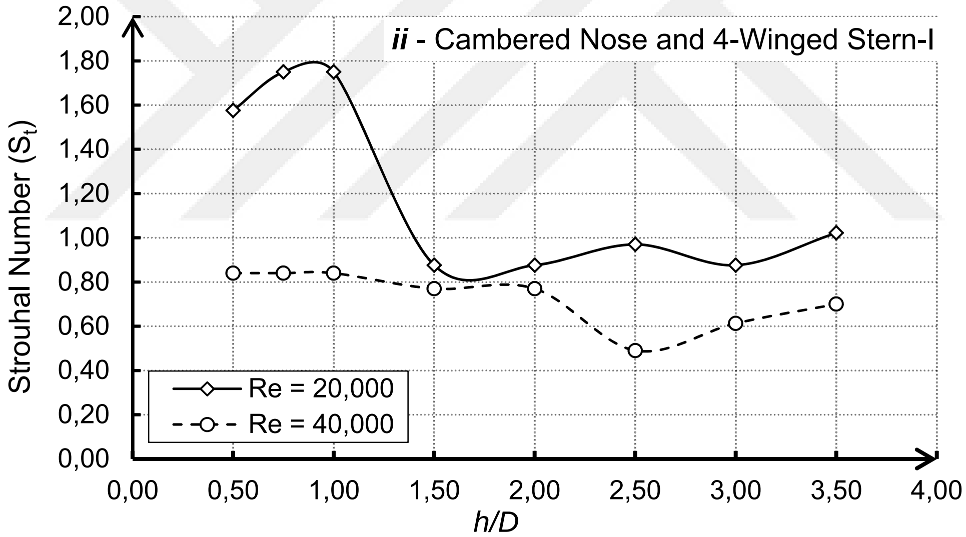

Figure 4.49. Variations of Strouhal numbers, S_t against submergence depth ratios *h/D* for the geometry consisting of the cambered nose and (i) 3-winged elliptical Stern-I and (ii) 4-winged elliptical Stern-I for the angle of attack α = 0° at Re = $20x10^3$ and $40x10^3$

At the submergence depth ratio of *h/D* = 1.5, the Strouhal number, S_t decreases dramatically to the value of St = 1 especially for Re = $20x10^3$. This is seen in all investigated torpedo-like geometries. Although the change in frequency, f_s is small, the Strouhal number, S_t is approximately halved for Re = 20x10^3 at *h/D* = 0.5 and 1.0 as the flow speed doubles, as it can be understood from the definition of the Strouhal number, S_t. After the submergence rate of *h/D* > 2, when the effect of the free surface becomes negligible, the vortex shedding frequency increases, f_s. Since the rates of increase in frequency, f_s and speed are approximately equal, Strouhal numbers, S_t take more or less the same values for Re = 20x10^3 and 40x10^3 for the cambered nose and wingless Stern-I. However, since the wingless Stern-I directs the flow towards the wake region, the vortex shedding frequency, f_s decreases gradually. Strouhal numbers, S_t for Re=20 x10^3 are 0.980, 0.876 and 0.876 for *h/D* = 2.5, 3 and 3.5 respectively and these values decrease to values of 0.446, 0.490, 0.490 for Re = 40 x10^3 with an approximately 50% reduction.

In the cases of the model geometry with 3-wings Stern-I and 4-wings Stern-I, the effects of free surface are significant for *h/D* = 0.5, 0.75 and 1. However, from the examination of dye visualization experiments and the quantitative observation of velocities for the wake regions, the vortex shedding is observed to be more regular. When the vortex shedding frequencies, f_s are evaluated as the change of force applied by the fluid on the body, high vortex shedding frequencies, f_s affect the hydrodynamic performance adversely. When numerical and experimental results of the model geometry with the winged stern section are evaluated together, it can be interpreted that the flow patterns damp the intensity of the large vortices in the flow region but do not cause a significant change in the vortex shedding frequency, f_s. The importance of controlling the vortex shedding, which negatively affects the maneuverability of underwater vehicles, can be seen clearly, especially at low submergence rates, *h/D* where the free-surface still effective. In the literature, many underwater vehicles have been investigating for this purpose.

5. CONCLUSION

The hydrodynamic characteristics of a model of underwater vehicle, called torpedo-like geometry were investigated numerically and experimentally under the effect of the water free-surface. The numerical study utilized the pressure-based solver of ANSYS-Fluent software while the experimental study employs the dye visualization and Particle Image Velocimetry (PIV) methods. The Large Eddy Simulation (LES) is performed to reveal the unsteadiness of the flow structure around the models of torpedo-like geometries, while the interface-capturing volume of the fluid fraction (VOF) method was used to model the free-surface.

The results show that the flow characteristics such as velocity field ($<u/U_\infty>$, $<v/U_\infty>$), streamline topology $<\Psi>$, vorticity $<\omega L/U_\infty>$, and Turbulent kinetic energy, $<TKE/U_\infty^2>$ become asymmetric as the torpedo-like geometry is located close to free-surface. Therefore, the resulted drag force, F_D corresponding to the drag coefficients, C_D were increased as the submergence depth is decreased. It was also found that the free-surface effect becomes negligible for submergence depth ratios higher than 2.0 ($h/D \geq 2.0$) owing to the near-symmetrical form of the flow structures. Also, when the Reynolds number is increased from Re = $20x10^3$ to $40x10^3$, time-averaged vorticity formation length and drag coefficient, C_D decrease for all examined torpedo-like geometries. For the h/D = 1.0, the highest acceleration realizes the region between the free surface and upper surface of the model. The wake of the torpedo-like geometry with 3-wings is smaller than the geometry with 4-wings. For the $h/D \geq 2.0$ the dimensionless vorticity concentrations, $<\omega\, L/U_\infty>$ around the free surface diminishes. The turbulent kinetic energy contours $<TKE/U_\infty^2>$ occur with a higher ratio around the air-water free-surface for h/D=0.5, 0.75 and 1.0. The time-averaged streamlines $<\Psi>$ calculated numerically for the cambered nose with wingless elliptical stern-I and stern-II geometries at Re = $40x10^3$ show that the free-surface affects the wake region and flow separation significantly. For *h/D* ≥ 2.0, the influence of the free surface on the streamline topology diminishes and the wake region becomes almost in a symmetrical shape. Some of the streamlines obtained experimentally using the PIV system is somehow different from the numerically predicted streamline topology. These differences might have resulted from the laser reflection from the model surfaces.

Variations of time-averaged drag coefficient values depending on the submergence depth ratio and Reynolds numbers for the considered torpedo-likes geometries demonstrates that as the submergence depth ratio, *h/D* increases from 0.5 to 3.5, time-averaged drag coefficient, C_D decreases gradually until *h/D* = 2.0 and beyond this submergence depth ratio, *h/D* the C_D becomes almost constant. The vortex shedding frequency results shows that the jet-like flow formed between the model geometry and the free surface results in momentum transfer between wake and core flow regions which can be considered as a source of higher frequency vortex shedding at submergence depth ratios, *h/D* = 0.75 and 1 under the effect of water free surface. At submergence rate of *h/D* = 1.5, the Strouhal number decreases dramatically to the value of S_t = 1 especially for Re = $20x10^3$. The presence of the free surface at Re = $20x10^3$ significantly affects the Strouhal number.

REFERENCES

Allston, T., Munroe, J., Lewis, R., Mouland, D., Xu, J., & Walker, D. (2014). Predicting the wake behind a large AUV hydrofoil. Methods in Oceanography, 10, 166-177.

Anonymous. (2019a). Auguste: pioneer of great heights and depths. Retrieved from https://www.daviddarling.info/encyclopedia/P/Piccard.html

Anonymous. (2019b). Deep water Remotely Operated Vehicle (ROV). Retrieved from http://www.rov-underwater.com/FOTO/rov2.png

Anonymous. (2019c). Historie Bathysphere von Barton und Beebe. Retrieved from http://www.profitaucher.de/Unterseiten/historie/Historie Bathysphere von Barton und Beebe.jpg

Anonymous. (2019d). Particle Image Velocimetry. Retrieved from Dantec Dynamics: https://www.dantecdynamics.com/solutions-applications/solutions/fluid-mechanics/particle-image-velocimetry-piv/measurement-principles-of-piv/

Anonymous. (2019e). REMUS 600. Retrieved from https://www2.whoi.edu/site/osl/wp-content/uploads/sites/8/2017/12/graphics-REMUS_dock_tests-_N802649.jpg

Anonymous. (2019f). Woods Hole Oceanographic. Retrieved from https://www.whoi.edu/

ANSYS. (2017). ANSYS Fluent Theory Guide. Ansys Inc.

Bellingham, J. (2009). Platforms: Autonomous Underwater Vehicles. In J. Bellingham, Encyclopedia of Ocean Sciences (pp. 473-484). Elsevier.

Doğan, S., Özgören, M., Okbaz, A., Şahin, B., & Akıllı, H. (2018). Serbest yüzey ve bir küre art izi arasındaki etkileşimlerin araştırılması. Gazi Üniversitesi Mühendislik-Mimarlık Fakültesi Dergisi, 33(3), 1123-1134.

Dubbioso, G., Broglia, R., & Zaghi, S. (2017). CFD analysis of turning abilities of a submarine model. Ocean Engineering, 129, 459-479.

Ferziger, J., & Perić, M. (2002). Computational Methods for Fluid Dynamics. Berlin, Heidelberg: Springer Berlin Heidelberg.

Goktepeli, I. (2016). Experimental Determination of Drag Coefficients for Torpedo-Like Geometries in an Open Wind Tunnel. International Conference on Advanced Technology and Sciences, (pp. 949-955).

Huang, T. S. (1978). Stern Boundary-Layer Flow on Axisymmetric Bodies. In Proceedings of the 12th ONR Symposium on Naval Hydrodynamics, (pp. 127-157). Washington, D.C.

Jagadeesh, P., & Murali, K. (2005). Application of low-Re turbulence models for flow simulations past underwater vehicle hull forms. Journal of Naval Architecture and Marine Engineering, 2(1), 41-54.

Jagadeesh, P., & Murali, K. (2010). Rans Predictions of Free Surface Effects on Axisymmetric Underwater Body. Engineering Applications of Computational Fluid Mechanics, 4(2), 301-313.

Jagadeesh, P., Murali, K., & Idichandy, V. (2009). Experimental investigation of hydrodynamic force coefficients over AUV hull form. Ocean Engineering, 36(1), 113-118.

Javanmard, E., & Mansoorzadeh, S. (2019). A Computational Fluid Dynamics Investigation on the Drag Coefficient Measurement of an AUV in a Towing Tank. Journal of Applied Fluid Mechanics, 12(3), 947-959.

KAYNARCALIOĞLU, M. (2016). Investigation of hydrodynamic and aerodynamic flow characteristics around a cylinder having an elliptic cross-section nose. SELÇUK UNIVERSITY.

Kim, S., Wilson, P., & Chen, Z.-M. (2015). Effect of turbulence modeling on 3-D LES of transitional flow behind a circular cylinder. Ocean Engineering, 100, 19-25.

Lin, J. (1996). NWENSAV2 software. Fluid Mechanics Lab, Lehigh University.

Lin, M.-y., & Huang, L.-h. (2010). Free-surface flow past a submerged cylinder. Journal of Hydrodynamics, 22(S1), 209-214.

Mansoorzadeh, S., & Javanmard, E. (2014). An investigation of free surface effects on drag and lift coefficients of an autonomous underwater vehicle (AUV) using computational and experimental fluid dynamics methods. Journal of Fluids and Structures, 51, 161-171.

Marx, R. (1990). The History of Underwater Exploration. Dover Publications.

McEwen, R., Hobson, B., McBride, L., & Bellingham, J. (2008). Docking Control System for a 54-cm-Diameter (21-in) AUV. IEEE Journal of Oceanic Engineering, 33(4), 550-562.

Pan, Y.-c., Zhang, H.-x., & Zhou, Q.-d. (2012). Numerical Prediction of Submarine Hydrodynamic Coefficients using CFD Simulation. Journal of Hydrodynamics, 24(6), 840-847.

Reichl, P., Hourigan, K., & Thompson, M. (2003). The Unsteady Wake of a Circular Cylinder near a Free Surface. Flow, Turbulence, and Combustion (formerly Applied Scientific Research), 71(1-4), 347-359.

Salari, M., & Rava, A. (2017). Numerical investigation of hydrodynamic flow over an AUV moving in the water-surface vicinity considering the laminar-turbulent transition. Journal of Marine Science and Application, 16(3), 298-304.

Shao, W., Zhang, Y., Zhu, D., & Zhang, T. (2013). Drag force on a free surface-piercing yawed circular cylinder in steady flow. Journal of Fluids and Structures, 43, 145-163.

Shepherd, K. (2001). Remotely Operated Vehicles (ROVs). In K. Shepherd, Encyclopedia of Ocean Sciences (pp. 742-747). Elsevier.

Tian, W., Song, B., & Ding, H. (2019). Numerical research on the influence of surface waves on the hydrodynamic performance of an AUV. Ocean Engineering, 183, 40-56.

Wikipedia. (2019). David Bushnell. Retrieved from https://en.wikipedia.org/wiki/David_Bushnell#/media/File:Turtle_submarine_1776.jpg

Wikipedia. (2019). Nautilus (1800 submarine). Retrieved from https://en.wikipedia.org/wiki/Nautilus_(1800_submarine)#/media/File:FultonNautilus.jpg

Wu, H., He, J., Liang, H., & Noblesse, F. (2019). Influence of Froude number and submergence depth on wave patterns. European Journal of Mechanics, B/Fluids.

YAĞMUR, S. (2016). Investigation of flow structure around torpedo-like geometries. SELÇUK UNIVERSITY.

CURRICULUM VITAE

Fuad SARIGIGUZEL was born in 1995 in Aleppo, Syria. He graduated from high school in Aleppo in 2012. He enrolled in the Mechanical Engineering Department of Çukurova University in Adana in 2012. He graduated from the Department of Mechanical Engineering and Automotive Engineering in 2017 and began his Master of Science in 2017. After completing his undergraduate studies, he worked as a project assistant at the Mechanical Engineering Department at Çukurova University in 2019. He is currently working as a project assistant in the same department.